# Numerical Investigation of Spray Formation in Air-Blast Atomizers

## Numerical study of air-blast atomization using a hybrid volume of fluid/discrete phase solver

B.I. Pal

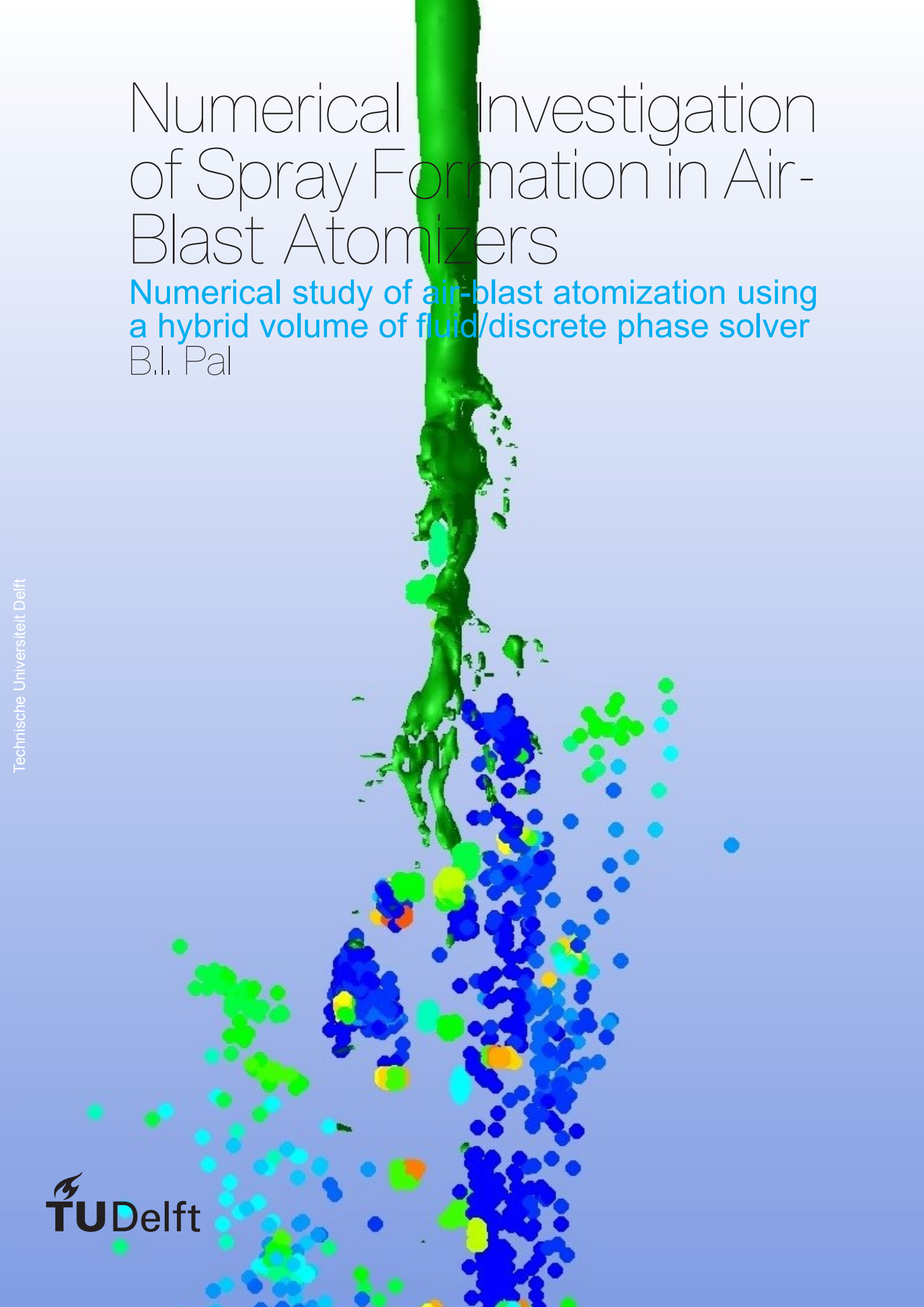

Technische Universiteit Delft

TU Delft

# Numerical Investigation of Spray Formation in Air-Blast Atomizers

## Numerical study of air-blast atomization using a hybrid volume of fluid/discrete phase solver

by

B.I. Pal

to obtain the degree of Master of Science
at the Delft University of Technology,
to be defended publicly on Wednesday July 3, 2019 at 9:00 AM.

| | | |
|---|---|---|
| Student number: | 4615794 | |
| Project duration: | November 1, 2018 – July 3, 2019 | |
| Thesis committee: | Ir. B. T. C. Zandbergen, | TU Delft, supervisor |
| | Prof. dr. D. J. E. M. Roekaerts, | TU Delft, co-supervisor |
| | Dr. A. Cervone, | TU Delft, committee chairman |

An electronic version of this thesis is available at http://repository.tudelft.nl/.

Cover picture portrays the surface of a round liquid jet as it breaks up in a gaseous coflow.

TU Delft

# Preface

What you are about to read is the result of a small, but steadfast attempt of nudging the train of rocket engine design forward. I don't know if it moved, but if it did, I think it was in the right direction. Early on, I did not fully realize the complexity of the phenomena I was about to research. I found the field of atomization to possess fascinating depth. The opportunity to use a new approach to investigate highly complex phenomena made the journey all the more interesting. I learned a lot about the difficulties and the rewards of venturing into the unknown. Sometimes you have to risk it all to feel like you might have made a difference. I can't wait to see what the future holds with respect to predictive modeling of complex fluid dynamics.

I would like to take this opportunity to thank Mr. Barry Zandbergen for the many meaningful discussions and his enthusiasm throughout the project. His eye for detail and his ever critical attitude have made me a sharper researcher. I would also like to thank Dr. Dirk Roekaerts for his priceless advice on numerical research and for granting me access to computational resources that were key to this project. The support of Dr. Roekaerts made it possible to present a poster and participate in a workshop that aims to facilitate advances in the field of spray modeling. Additionally, I would like to thank Dr. Assaad Masri from The University of Sydney for the provided measurement data.

My thanks go out to my parents, who have nurtured my interest in science and helped me summon the courage to push my boundaries. I will always be thankful to my wife, Katya, who has remained patient through delays, hardships and failures. Last, but not least, thanks go out to Paul and Veronica Townsend for their unwavering support.

*B.I. Pal*
*Delft, July 2019*

# Summary

The conducted study investigates the potential of a newly released multi-phase solver to simulate atomization in liquid rocket injectors. The ”VOF-to-DPM” solver was used to simulate primary and secondary atomization in an air-blast atomizer with a coaxial injector-like geometry. The solver uses a hybrid Eulerian/Eulerian-Lagrangian formulation with a geometric transition criteria between the two models. The conducted study assumed isothermal, non-reacting flow at room temperature. The primary focus was predicting Sauter Mean Diameter and droplet velocity data at a sampling plane downstream of the injection site. The results showed that the solver is able to produce the expected data and to predict trends similar to those found in experimental measurements. The accuracy of the produced droplet diameters was roughly a factor 2 off compared to experiment. This is attributed to mesh resolution. Measurements were obtained via a cooperative agreement between TU Delft and The University of Sydney. It was concluded that the solver has the potential to predict atomization at a reasonable computational cost, but further study is needed to confirm its full capabilities.

# List of Figures

# List of Tables

# Contents

# Nomenclature

**List of Abbreviations**

| | |
|---|---|
| CFD | Computational Fluid Dynamics |
| CSF | Continuum Surface Force |
| CSS | Continuum Surface Stress |
| DES | Detached Eddy Simulation |
| DNS | Direct Numerical Simulation |
| DPM | Discrete Phase Model |
| DRW | Discrete Random Walk |
| LDV | Laser Doppler Velocimetry |
| LES | Large Eddy Simulation |
| PDA | Phase Doppler Anemometry |
| RANS | Reynolds Averaged Navier Stokes |
| SBES | Stress Blended Eddy Simulation |
| SDES | Shielded Detached Eddy Simulation |
| SGS | Sub-Grid Scale |
| VOF | Volume of Fluid |
| WALE | Wall Adapting Local Eddy-Viscosity Model |
| WMLES | Wall Modeled Large Eddy Simulation |

**List of Subscripts**

| | |
|---|---|
| $l$ | Liquid |
| a | Arbitrary fluid phase a |
| b | Arbitrary fluid phase b |
| e | Eddy |
| p | Particle |
| r | Relative |

**List of Symbols**

| | | |
|---|---|---|
| $\Delta$ | LES filter cutoff width | $m$ |
| $\delta$ | Kronecker Delta | $N/A$ |
| $\dot{m}$ | Mass flow rate | $kg/s$ |
| $\epsilon$ | Rate of dissipation of turbulent kinetic energy per unit mass | $m^2/s^3$ |

| | | |
|---|---|---|
| $\Gamma$ | Vandenkerchkove constant | $N/A$ |
| $\gamma$ | Ratio of specific heats | $N/A$ |
| $k$ | Curvature | $m$ |
| $\mathcal{T}$ | Surface stress tensor | $Pa$ |
| $\mu$ | Dynamic viscosity | $Pa \cdot s$ |
| $\mu_t$ | Turbulent viscosity | $Pa \cdot s$ |
| $\phi$ | Arbitrary flow variable | $N/A$ |
| $\rho$ | Density | $kg/m^3$ |
| $\sigma$ | Surface tension coefficient | $N/m$ |
| $\tau$ | Characteristic time | $s$ |
| $\tau_B$ | Breakup time | $s$ |
| $\tau_d$ | Dwell time | $s$ |
| $\mathbf{a}$ | Acceleration | $m/s^2$ |
| $\mathbf{F}$ | Force | $N$ |
| $\mathbf{g}$ | Gravitational acceleration | $m/s^2$ |
| $\mathbf{u}$ | Fluid velocity | $m/s$ |
| $\mathbf{x}$ | Position vector | $m$ |
| $\xi_c$ | Combustion efficiency | $N/A$ |
| $a1$ | Drag coefficient parameter | $N/A$ |
| $a2$ | Drag coefficient parameter | $N/A$ |
| $a3$ | Drag coefficient parameter | $N/A$ |
| $A_t$ | Throat area | $m^2$ |
| $A_{cell}$ | Cell area | $m^2$ |
| $B_0$ | WAVE model constant | $N/A$ |
| $B_1$ | WAVE model constant | $N/A$ |
| $c^*$ | Characteristic exhaust velocity | $m/s$ |
| $C_d$ | Coefficient of drag | $N/A$ |
| $d$ | Diameter | $m$ |
| $D_c$ | Coflow diameter | $m$ |
| $D_n$ | Needle diameter | $m$ |
| $D_p$ | Pilot diameter | $m$ |
| $e$ | Mesh adaption error | $N/A$ |
| $I$ | Identity matrix | $N/A$ |
| $J$ | Jet Momentum Ratio | $N/A$ |

| | | |
|---|---|---|
| $k$ | Turbulent kinetic energy per unit mass | $m^2/s^2$ |
| $l$ | Length scale | $m$ |
| $L^*$ | Chamber characteristic length | $m$ |
| $L_c$ | Chamber length | $m$ |
| $l_e$ | Eddy length scale | $m$ |
| $M$ | Momentum ratio | $N/A$ |
| $m$ | Mass | $kg$ |
| $N$ | Number of droplets | $N/A$ |
| $Oh$ | Ohnesorge number | $N/A$ |
| $p$ | Pressure | $Pa$ |
| $P_c$ | Chamber pressure | $Pa$ |
| $R$ | Specific gas constant | $J/(kgK)$ |
| $r$ | Radius | $m$ |
| $r_{vol}$ | Mesh adaption volume weight parameter | $N/A$ |
| $Re$ | Reynolds number | $N/A$ |
| $S_m$ | Mass source term | $kg/(m^3s)$ |
| $T$ | Integral time scale | $s$ |
| $t$ | Time | $s$ |
| $T_c$ | Chamber temperature | $K$ |
| $V_c$ | Chamber volume | $m^3$ |
| $We$ | Weber number | $N/A$ |

# 1

# Introduction

Recent successes in space launch vehicle engineering have dramatically reduced the cost of access to space. Space Exploration Technologies Corporation's (SpaceX) successfully tested reusable launch vehicles have enabled a cost reduction to around 90 million USD for missions that the Space Shuttle performed for 450 million USD [2][23]. The debate on the feasibility of a competitively priced expendable launcher (Ariane 6) is ongoing [4][5]. At the time of writing of this document, sources indicate that a reusable Falcon 9 is about 10 million USD cheaper per launch than the currently advertised cost for the new Ariane 6 [2][5].

As launch costs decrease, the financial feasibility of putting large payloads into orbit increases. This opens up the possibility of renewed efforts of planetary exploration. An example is the planned SpaceX mission to Mars [55]. The company intends to land cargo on the surface of Mars by 2022 and crewed vehicles by 2024 [3]. Other missions involving planetary landings are also in the works by the ESA and Roscosmos [6]. It is worth noting that the technology that has enabled the reuse of launch vehicles also has potential in the case of planetary landings. Specifically, powered landings have enabled SpaceX to reuse the first stage of a Falcon 9 [63]. The same engine technology can and likely will be used for future planetary landings.

A primary propulsion system requirement for any mission involving a planetary lander is throttleability. This is evident by the thrust profile requirement for the Lunar Module Descent Engine as well as the Viking Landers' engines. Fig. 1.1 shows the thrust profiles for the Apollo lander and the Viking landers respectively.

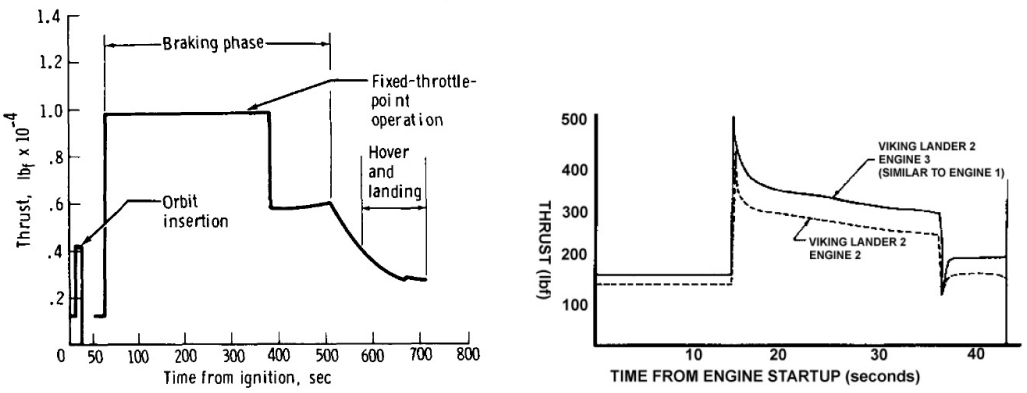


Figure 1.1: Thrust profiles for Apollo lander(left) [26] and Viking lander(right) [53]

Both figures show required thrust changes in the range of a 4:1 ratio - which qualifies as a "deep throttling" requirement [9]. This capability is provided by liquid rocket engines, since the flow rate of both propellants can be controlled directly. Experience has shown that

engines using fixed-area injectors are prone to instabilities that can cause failures [13]. Since instabilities are associated with variable pressure drop in fixed area injectors, research was conducted in variable area injectors by the TRW corporation in the 1960's. The resulting injector design, called a pintle injector, was used successfully in the Lunar Module Descent Engine and several subsequent TRW engines. It is worth noting that not all instabilities stem from pressure drop variation in the feed lines. As discussed by Zandbergen et al., there are three classes of instabilities: low-frequency (the one mentioned), medium frequency and high frequency [68]. It should therefore be noted that the pintle injector is not necessarily a solution to every type of instability. It has been shown to alleviate low-frequency instabilities that stem from chamber-feed system interactions. The most common injector used for large rocket engines has been the coaxial hollow post injector [27]. This type of injector can can also be throttled, but within a narrower range compared to the pintle injector [68]. This is due to the aforementioned low-frequency instabilities that can be triggered when the pressure drop across injector elements dips below a certain level. Given the large amount of literature available on these types of injectors, a study of their throttling limitations may also be worthwhile. In addition, Betts et al. points out that pintle injectors typically have lower combustion efficiency than other common injector types (e.g. coaxial injector) [9].

## 1.1. Liquid Rocket Injectors - State of the Art

A literature study was conducted to investigate the status of current liquid rocket injector research [45]. Firstly, it was identified that the performance metrics of a liquid rocket injector are the produced droplet diameters and droplet size distribution parameters. Most research on injectors is related to the prediction of these metrics either via experimental or numerical methods.

Experimental studies produce the most reliable results and are the benchmark for validation of numerical tools. The drawbacks are high cost and lack of flexibility in changing studied variables. Recent experimental studies of liquid rocket injector sprays use shadowgraph-type or laser-based techniques to measure droplet sizes [48][42][7]. These studies require specialized measurement equipment and software to produce quality results. Other studies examine the differences between various injector geometries with the aim of identifying design trends [61][40]. Prototypes are built and tested using cold-flow and hot-fire tests. The results from different geometries are compared with regards to performance and failure modes. Collectively, the results from recent experimental studies indicate that design trends regarding spray angles and atomization quality are well understood. The challenge lies in the quantitative measurement of droplet sizes. These experiments require the most sophisticated equipment and software.

It was found that numerical studies have the potential to produce results quicker than experiment with the added advantage of allowing the studied parameters to be changed at virtually no cost. The identified difficulties with numerically simulating the injection process were the high cost of simulating both primary and secondary atomization accurately. Most studies employed methods that model primary atomization and attempt to predict the secondary atomization region using empirical parameters. These methods are less computationally demanding, but often require experimental data as an input. The most commonly employed method is the injection of a known distribution of droplets into the computational domain. This method was used by all the works found on the topic of pintle injector research [57][67][56][19]. While these studies were computationally affordable, most are not validated with experimental measurements. The outcomes are mainly qualitative and show what trends can be expected from varying injector geometries. No publicly available raw data on pintle injector sprays were found. Other numerical studies highlight the prohibitively high computational cost of simulating primary and secondary atomization knowing upstream conditions only [38][20]. Based on the available studies, one can conclude that there is a need for computationally cheap numerical methods that predict both primary and secondary atomization without a priori knowledge of experimental results.

## 1.2. Previous work at TU Delft

This section briefly introduces research activities related to pintle injectors at TU Delft and the driving factors behind them.

At the faculty of Aerospace Engineering, experimental studies have been carried out concerning rocket engine pintle injectors [36][47]. In addition, the student team DARE (Delft Aerospace Rocket Engineering) is currently developing a pintle injector. A prototype has been built, but no simulations of the injector have been carried out to date. The DARE design team has confirmed a need for the capability to numerically model the injection process.

At the TU Delft faculty of Mechanical Engineering, numerical modeling of spray combustion is a current research topic in the broader context of energy engineering [8][10][46]. TU Delft is one of several universities collaborating in the organization of the Workshop on Measurement and Computation of Turbulent Spray Combustion. The goal of the proceedings is the advancement of the capability to model reacting and non-reacting turbulent spray flows. [28] While this research is not specifically related to liquid rocket injectors, spray combustion is at the center of injector applications and thus the link between research at the two departments.

## 1.3. Thesis Objectives

The original idea for the objective of this work was the simulation of a pintle injector due to its mentioned characteristics and relevance to research interests at TU Delft. The use of a novel multi-phase solver was key to the proposal.

Due to the lack of available data and the need for a simpler geometry, it was decided not to simulate a pintle injector. An existing collaboration between TU Delft and The University of Sydney provided an opportunity to use high quality measurement data from an air-blast atomizer. Measurements were carried out at The University of Sydney School of Aerospace, Mechanical and Mechatronic Engineering. The geometry is very similar to that of a coaxial injector common in large liquid rocket engines. A successful validation of the new solver using the geometry of a coaxial injector element could pave the way for subsequent simulations of other injector types (e.g. pintle injector). A thesis proposal was therefore submitted with the following goal:

**The aim of the proposed study is the accurate prediction of spray properties at reasonable computational cost, using the VOF-to-DPM solver.**

Specifically, the following research questions are proposed:

1. Can the Ansys VOF-to-DPM solver predict experimental trends correctly?
   - 1.1. Are droplet size and velocity trends predicted correctly?
   - 1.2. What solver parameters and breakup models predict trends correctly?
2. Can the Ansys VOF-to-DPM solver predict spray properties accurately?
   - 2.1. Are droplet size and velocity values predicted accurately?
   - 2.2. What solver parameters and breakup models predict spray properties most accurately?

In the context of this study, an accurate prediction of spray properties is defined as a maximum Sauter Mean Diameter and velocity magnitude error of 10%. Similarly, reasonable computational cost is defined as a simulation time of no more than two weeks on a single, 16 core machine.

While the objective of this work is similar to other research efforts documented in open literature, the numerical solver used (Ansys 19.2 VOF-to-DPM [51]) constitutes a new approach to solving the problem of spray characterization. It is therefore also the objective of the study to show that the solver is indeed capable of producing a distribution of droplets and that the obtained results show a trend that is physically relevant.

## 1.4. Methodology

An air-blast atomizer type spray will be modeled numerically using the commercially available Computational Fluid Dynamics (CFD) software, Fluent ver 19.2. The finite volume method will be applied to solve the governing equations using Reynolds Averaged Navier Stokes (RANS) and Large Eddy Simulation (LES) turbulence models. The simulations will model non-reacting flow of coaxially flowing streams of acetone and air at constant temperature and pressure. Ansys VOF-to-DPM solver will be used to model multi-phase flow [51].

The methods used to answer the research questions mentioned in the previous section are as follows:

- Question 1.1 - Droplet diameters and velocities are directly calculated by the solver and sampled at user defined planes.
- Question 1.2 - Several test runs are carried out, using different solver settings. Results are compared.
- Question 2.1 - Average Sauter Mean Diameter and velocity errors are quantified for each test run.
- Question 2.2 - Several test runs are carried out using different solver settings. Error values are compared.

Numerical studies are invaluable during the course of a research project since they provide quantitatively and qualitatively better results than an analytical approach, but are more flexible and at times less costly than experimental analysis. Analytical analysis is often the first step of a research effort. Results can be obtained quickly, but usually lack accuracy due to simplifying assumptions. Experimental studies provide the most reliable results as they aim to replicate the studied phenomena. The disadvantage lies with the lack of flexibility with regards to changing design variables as this often requires rebuilding the test-setup and/or purchasing additional equipment. Numerical studies do not suffer from this disadvantage - the simulation setup can be changed quickly and without additional cost. The results are also often more accurate than the analytical. For these reasons, a numerical study of an injector is warranted.

Given that an important purpose of injectors in liquid rockets is atomizing the propellants, it was deemed necessary to be able to simulate the atomization process as a first step towards a full combustion simulation. During throttling, the atomization quality is one of the parameters that can change significantly. A literature study of pintle injector simulations has shown that the most commonly used numerical methods for atomization simulations require experimental data as an input [45]. Combustion simulations inject droplets whose properties match those of measured distributions. This negates some of the advantages of numerical work. The ability to simulate atomization without any experimental input would be beneficial for the development of not only pintle injectors but other types of injectors as well. A novel multi-phase solver released by Ansys attempts to tackle this problem. Detailed discussions on identified needs in atomization simulations and the merits of the selected solver can be found in chapters 2 and 3 respectively.

The author's internship experience (numerical study of underexpanded jets) and interest in numerical studies of fluid flow (computational fluid dynamics) as well as rocket propulsion were also a reason for choosing numerical investigation of injectors as a research topic. It is the author's view that predictive injection models have great potential in reducing development costs and time for new technologies in the propulsion industry.

## 1.5. Verification & Validation

Verification and validation are key parts of any numerical study. The methods used in this work are outlined below:

**Verification** of simulation results is done via two checks to ensure correct model implementation:

- Mass flow rate verification - the net mass flow rate for the simulation domain must approach zero
- Residuals - the residuals of the calculated equations must remain in a narrow range below a minimum threshold

These methods were chosen from several outlined by NASA in the framework of the "National Program for Application Oriented Research in CFD" [41]. Based on the standards outlined by NASA, this work will only partially be verified due to the time constraints of the project.

**Validation** of the results will be done via comparison of droplet sizes and velocities to experimental values obtained using Phase Doppler Anemometry (PDA) and Laser Doppler Velocimetry (LDV) at set distances from the injection site. The importance of validation by comparison with experiment is explained by Versteeg et al. [62].

## 1.6. Organization

Thus far, the importance of throttleable liquid rocket engines has been introduced together with the research interests at TU Delft and in the wider engineering community. The objective of the work to be carried out and the methodology to be used have also been established. In closing, the structure of the information presented in this document is summarized below:

- **Chapter 2** - This chapter presents the function and operating principle of liquid rocket injectors including the pintle and coaxial injectors. Basic theory related to injector function is also included. The last section discusses recent works on the topic of injection simulation in rocket engines.
- **Chapter 3** - This chapter presents the theory behind the implemented numerical models used for spray analysis.
- **Chapter 4** - This chapter presents unfinished, preliminary work that was done early on during the course of the present study. This work concerns an experimental case other than the primary case that forms the topic of this study.
- **Chapter 5** - The experimental setup is presented. The domain, mesh, boundary conditions as well as simulation settings of interest are presented and discussed.
- **Chapter 6** - The results of all the simulations are presented and discussed.
- **Chapter 7** - Chapter 7 discusses the methods used to verify the numerical solver and the results of the verification.
- **Chapter 8** - The topic of the chapter is validation. Results are compared with experimentally measured values. The chapter begins with a discussion on the methods used to establish convergence.
- **Chapter 9** - Research questions are answered and recommendations for future work are presented.

# 2

# Liquid Rocket Injectors

This chapter provides an overview of the operating principles of liquid rocket injectors. After the introduction of injector basics, the pintle injector is introduced and described in detail. The coaxial injector is then introduced as a limiting case of a pintle injector. The focus of the chapter is to highlight the operating principles of an injector and the basic theory necessary to understand its function. The chapter ends with an overview of recent works on simulating propellant injection in rocket engines.

## 2.1. Liquid Rocket Injectors - Introduction

An injector is defined as a disk or cylinder that contains openings or holes [68]. Huzel et al. states that the function of any liquid rocket injector is the introduction and metering of propellants into the combustion chamber. The injector is also responsible for atomizing and mixing the propellants for best combustion efficiency. Huzel et al. also points out that combustion efficiency is closely linked to the design of the injector [27]. As an example, a depiction of the Space Shuttle Main Engine injector can be seen in Fig. 2.1 below [59]:

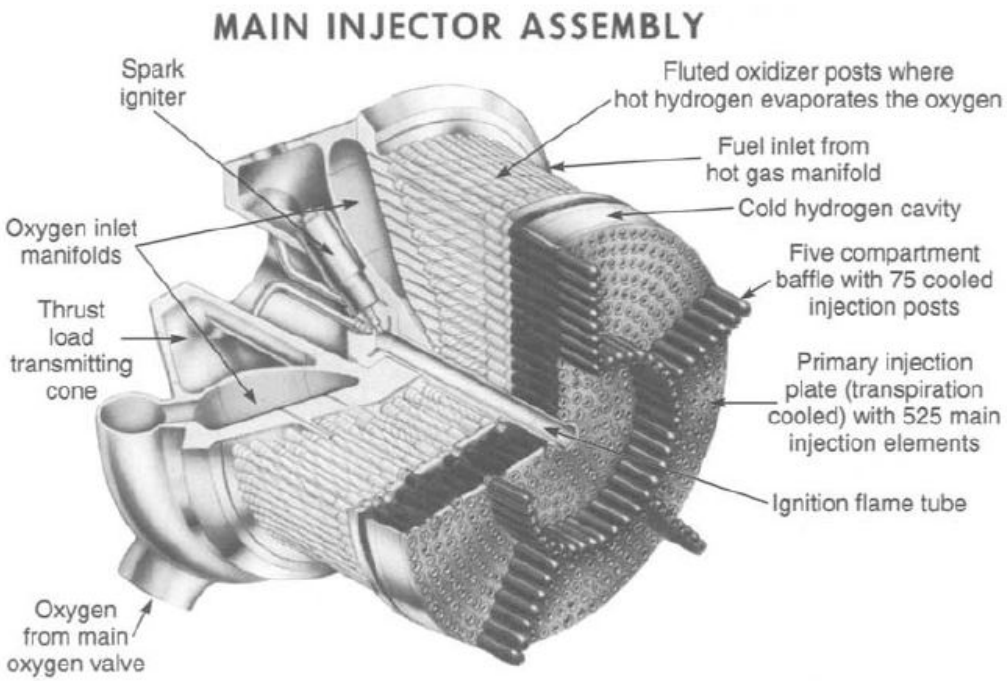


Figure 2.1: Space Shuttle Main Engine injector schematic [59]

Let us discuss the three injector functions (propellant metering, atomization and mixing) in the context of combustion efficiency. As mentioned by Zandbergen et al., the most desirable propellant spray is one that provides the highest combustion efficiency (in general) [68]. Combustion efficiency in the context of rocket propulsion is defined by eq. 2.1 below:

$$\xi_c = \frac{{c^*}_{real}}{{c^*}_{ideal}} \tag{2.1}$$

Specifically, combustion efficiency is the ratio of the real and ideal characteristic velocities of the engine. Characteristic velocity is defined in eq. 2.2 below [68]:

$$c^* = \frac{\sqrt{RT_c}}{\Gamma} \tag{2.2}$$

In the above equation, R is the mean molecular weight of the exhaust gases, $T_c$ is the chamber temperature and Γ is a function of the ratio of specific heat capacities. Eq. 2.3 defines Γ below [68]:

$$\Gamma = \sqrt{\gamma}\left(\frac{2}{\gamma+1}\right)^{\frac{\gamma+1}{2(\gamma-1)}} \tag{2.3}$$

Zandbergen et al. [68] explains that $c^*$ indicates the available energy level of the propellants for propulsion. An additional expression for $c^*$ is denoted by eq.2.4 [68]:

$$c^* = \frac{P_c A_t}{\dot{m}} \tag{2.4}$$

,where $P_c$, $A_t$ and $\dot{m}$ are chamber pressure, throat area and mass flow rate respectively. Zandbergen et al. continues by stating that the terms on the right hand side of Eq. 2.4 can be experimentally obtained (it should be noted that this applies only for high Reynolds number cases where the discharge coefficient can be neglected) [68]. This allows for a comparison between the theoretical value calculated via eq. 2.2 and the real $c^*$ calculated from measured values.

Based on the above definitions, it follows that in order to increase combustion efficiency, the goal is to maximize the obtainable chamber pressure for a given propellant mass flow rate. In other words, the amount of energy extracted from the propellants for propulsion should be maximized. Chamber pressure is not the only variable of importance (as related to combustion efficiency), but for the purpose of this discussion, further details on combustion are omitted.

For maximum energy release, it is required that propellants react fully in the combustion chamber. To be specific, there should not be unburnt propellant exiting the engine. This sometimes occurs in rocket engines by design, for reasons such as cooling, throttling etc. From the sole perspective of energy release however, this is undesirable. This is where propellant metering, atomization and mixing come into play.

As previously discussed, in order to maintain the desired chamber pressure, a certain propellant mass flow rate must be provided. However, for propellants to fully react, proper mixing is required. Huzel et al. [27] states that the better the uniformity of oxidizer/fuel distribution produced by the injector, the more rapidly the equilibrium composition necessary for optimum combustion is achieved. The role of atomization (droplet formation) is to facilitate droplet vaporization and consequently, propellant mixing. Smaller droplets present a larger liquid surface area (relative to droplet mass) exposed to the surrounding gas, thus increasing heat transfer and reducing vaporization time [68].

An additional requirement for propellants to fully react is known as the dwell time. This is the estimated amount of time that propellants spend in the combustion chamber. This is important because it is a measure of the available time for evaporation and combustion to take place. Dwell time is defined by eqn. 2.5 [68]:

$$\tau_d = \frac{L_c}{U_c} \tag{2.5}$$

,where $L_c$ and $U_c$ are the chamber length and the average velocity inside the chamber respectively. When it comes to chamber design, the length of the chamber is determined by the propellant dwell time. The characteristic length of the chamber is defined by eqn. 2.6 and depends on the propellants [68]:

$$L^* = \frac{V_c}{A_t} \tag{2.6}$$

,where $V_c$ and $A_t$ are the chamber volume and throat area respectively. The dwell time is related to the characteristic length and velocity by eqn. 2.7, which illustrates why the characteristic length is determined by the propellants [68].

$$\tau = \frac{L^*}{\Gamma^2 c^*} \tag{2.7}$$

To show the importance of droplet diameters during engine design, consider the following scenario: a hydrazine droplet having an initial diameter of 200 microns and a temperature of 300K is formed by the injector of a rocket engine. The chamber temperature is assumed to be 3000K. Using the relations for drop diameter vs time, from the work of Penner, yields an evaporation time of roughly 15 ms [50]. An example of radius vs time and temperature vs time values obtained by Penner for a hydrazine droplet can be seen in Fig. 2.2 below:

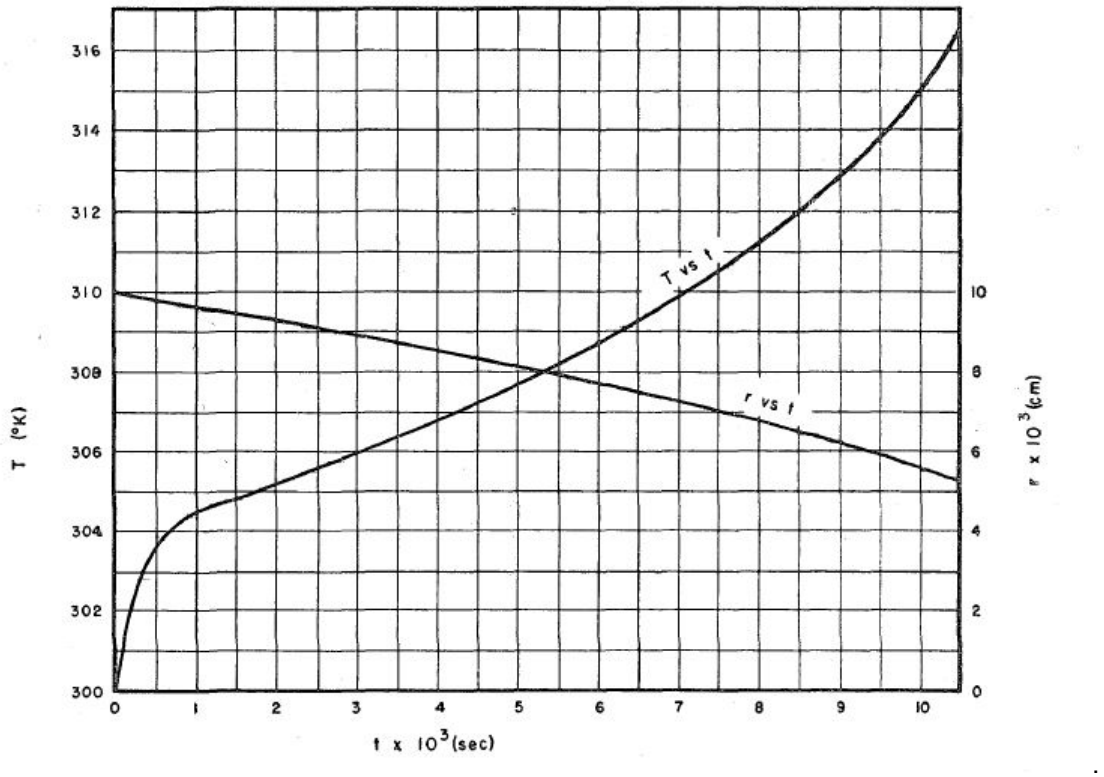


Figure 2.2: Droplet radius vs time and temperature vs time [50]

Assuming the droplet travels with an average velocity of 100 m/s yields a required chamber length of 1.5 m for full evaporation. A 100 micron droplet under the same conditions would evaporate in about 4 ms, requiring a chamber length of .4 m. These and other sample calculation results can be seen in Table 2.1:

Table 2.1: Chamber length example calculation

| Initial diameter (microns) | Evaporation time (ms) | Chamber Length (m) |
|---|---|---|
| 300 | 35 | 3.5 |
| 200 | 15 | 1.5 |
| 100 | 4 | .4 |

## 2.2. Injector Performance

The close link between combustion efficiency of an engine and the design of the injector has thus far been established. Combustion efficiency can be considered a propulsion system level performance metric. There are performance parameters that can be said to be a property of the injector itself. These are briefly discussed in the following paragraphs.

As mentioned previously, the level of propellant atomization is a direct result of the injector design. Atomization is formally defined as the conversion of bulk liquid into droplets [31]. Two regimes of atomization are distinguished: primary and secondary. Primary atomization is the breakup of a liquid column into ligaments. Secondary atomization is the further breakup of ligaments\droplets into smaller droplets. From a performance point of view, a definition of the quality of atomization is warranted. As discussed by Lefebvre et al., atomization quality is commonly defined as a mean drop size [31]. Due to the complexity of the physical process of atomization, mainly empirical relationships are used to predict mean drop size for different types of atomizers and propellants. Since most sprays are nonuniform, an additional property that must be taken into account together with the mean drop size is the drop size distribution. It can therefore be said that atomization quality consists of a mean drop size and drop size distribution parameters.

Lefebvre et al. categorizes the available relations for drop size distributions into two categories: mathematical (Normal distribution, Log-normal distribution and Log-hyperbolic distribution) and empirical (Nukiyama & Tanasawa, Rosin-Rammler, Modified Rosin-Rammler, Upper limit function) [31]. It is mentioned that due to the lack of understanding regarding the physical phenomena affecting droplet formation, no mathematical model is clearly better than the others. The available models are mostly developed based on empirical considerations or probability. The primary purpose of these models is to offer alternatives to test during data-fitting trials.

The empirical models used to characterize droplet size distributions are most often tied to a specific type of disintegration mechanism. Just as in the case of mathematical models, empirical models need to be tested using trial and error versus each data-set. There is no evidence to suggest one is better than the other for any given case. After discussing a number of empirical models (Nukiyama & Tanasawa, Rosin-Rammler, Modified Rosin-Rammler, Upper-Limit Function), Lefebvre et al. concludes that the best reasons for selecting one model over the other are [31]:

1. mathematical simplicity
2. ease of manipulation in computations
3. consistency with the physical phenomena involved

In other words, the best model is the one that is easiest to use and correlates best with experimental results. For a more detailed overview of mathematical and empirical drop size distributions, the reader is referred to the literature study by Pal [45].

The most commonly used model for drop size distribution is Rosin-Rammler. It is a two-parameter distribution that takes the form seen in Eq. 2.8 [31]:

$$1 - Q = e^{-(\frac{D}{X})^q} \tag{2.8}$$

where Q represents the fraction of the total volume in droplets of diameter less than D and X and q are constants. The parameter q is a measure of the spread of drop sizes. Higher

values of q will yield a more uniform spray. Typical values for q are between 1.5 and 7 [31]. X is a representative drop size equal to .632 of the maximum drop size of the distribution. Using this model, a droplet distribution can be represented by only two parameters. A known drawback of this relation is the inability to portray multipeaked distributions [31]. Fig. 2.3 is an example of a Rosin-Rammler distribution:

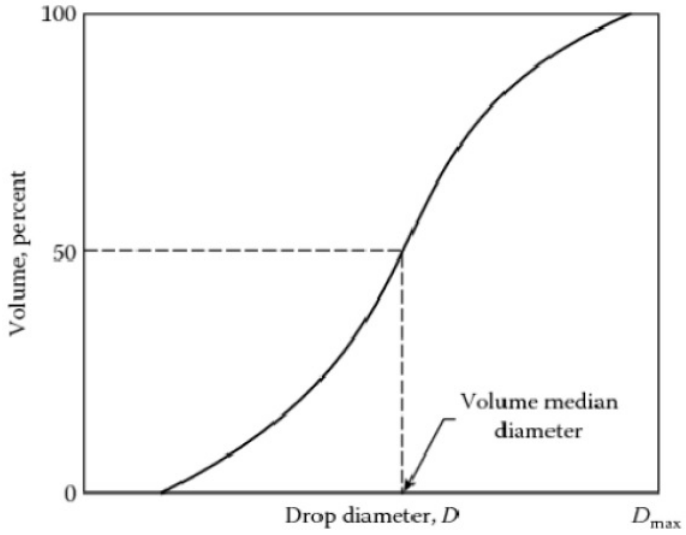


Figure 2.3: Rosin-Rammler distribution [32]

Fig. 2.4 is a representation of the effect of the parameter q on a Rosin-Rammler distribution. It indicates that higher values of q will results in a more uniformly distributed spray over a larger range of diameters.

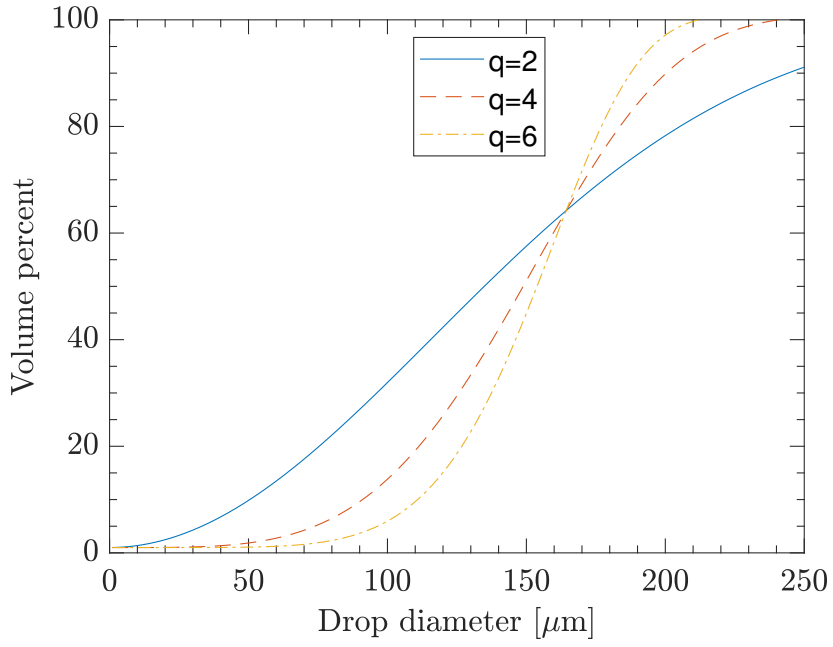


Figure 2.4: Rosin-Rammler distribution examples

There are several formulations for mean drop sizes in a spray, depending on the formula used to obtain the mean diameter. Some formulations are more relevant than others for a

particular application. In the case of the pintle injector, a commonly used formulation is the Sauter Mean Diameter (SMD) [47][42][48]. This is because the SMD is a surface-area weighted diameter distribution. Eq. 2.9 defines the Sauter Mean Diameter of a group of droplets:

$$SMD = \frac{\sum N_i d_i^3}{\sum N_i d_i^2} \tag{2.9}$$

,where i indicates a class of droplets of the same diameter, N is the number of droplets in class i and d is the diameter of each droplet in class i. Lefebvre et al. makes a number of noteworthy points regarding the mean diameter and drop size distribution of a spray[31]:

1. More than one parameter is necessary to define a drop size distribution
2. There is no correlation between a spray's mean diameter and its drop size distribution

Based on the presented reasoning, performance criteria for injectors could be established referencing a target mean droplet diameter (for the produced spray) that would ensure a specific degree of vaporization. Criteria for mean droplet sizes at set distances from the injector face can be established as performance metrics for a particular injector. Considering the engine as a whole, depending on the design, performance criteria for vaporization distances and/or dwell times can be considered. Vaporization distance is relevant because it can dictate the size of the combustion chamber if full propellant vaporization is key. It is also relevant if the spray from the injector is used to cool the walls of the chamber. In this case it is important that the liquid propellant does not vaporize before reaching the wall. These are the main links between engine performance and spray properties.

Up to this point, liquid rocket injectors and their roles in a rocket engine have been defined and discussed from a general point of view. It's been established that the performance of an injector is characterized by the properties of the spray it is able to produce. The following section will introduce dimensionless quantities relevant to atomization studies.

## 2.3. Quantities of interest in the context of atomization

In studies of fluid flows, it is common practice to calculate dimensionless quantities that can indicate what the flow field may look like or how it may behave. There is physical reasoning behind the choices of forces or material properties that are used in these ratios and some are problem dependent. Experimental measurements often quantify how the flow field of a certain problem may change within a range of some dimensionless parameter. In the context of atomization, there are three dimensionless parameters of interest:

- $We$ - Weber number
- $Re$ - Reynolds number
- $Oh$ - Ohnesorge number

The **Weber number** (We) is a ratio of inertial forces to surface tension forces in a liquid ligament or droplet. This quantity is used to categorize secondary breakup regimes (the breakup of ligaments and droplets into smaller fragments) [29]. The Weber number is defined by eqn. 2.10 below:

$$We = \frac{\rho u^2 l}{\sigma} \tag{2.10}$$

where $\sigma$ is the surface tension coefficient of the liquid and the other properties are that of the surrounding gas. The velocity is that of the gas relative to the liquid. A visual description of the breakup regimes that can be categorized by We ranges can be found in the work of Roekaerts et al. seen in fig. 2.5 [29].

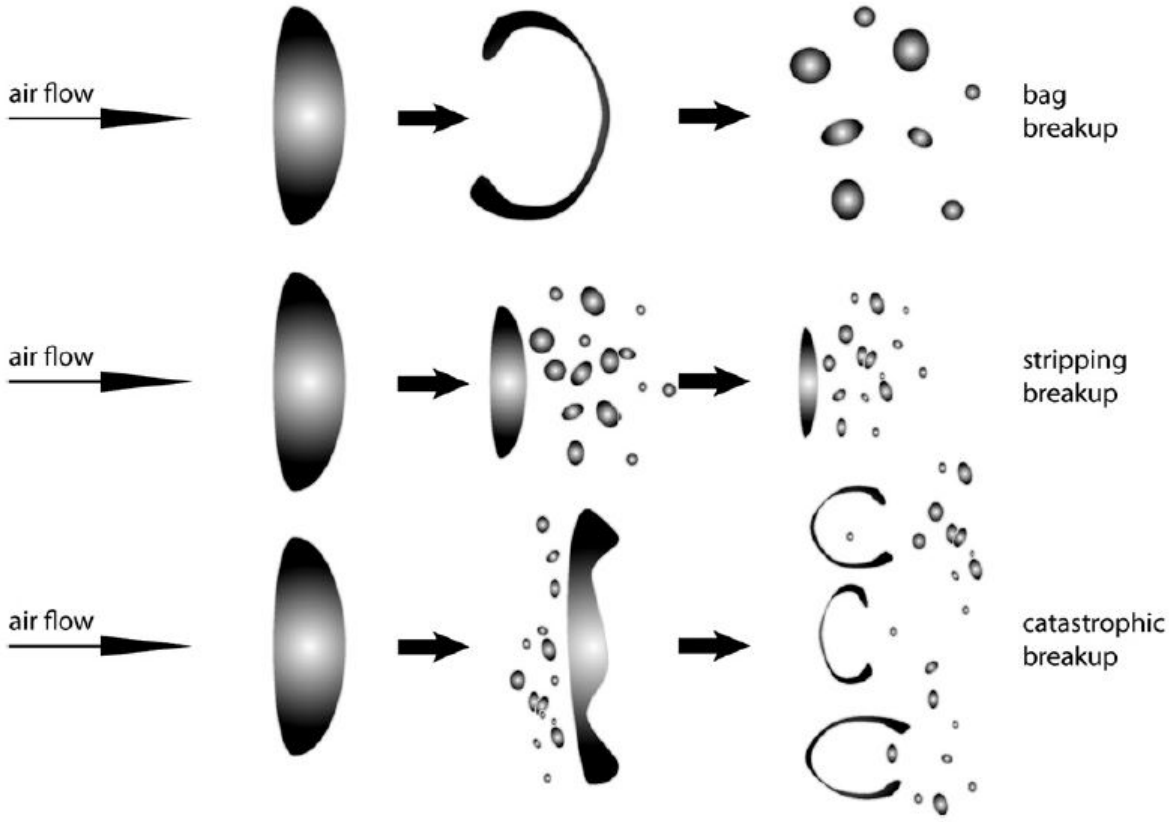


Figure 2.5: Secondary breakup regimes [29]

The **Reynolds number** (Re) is a dimensionless quantity that represents the ratio of inertial forces and viscous forces in a fluid. It is defined by eq. 2.11 below:

$$Re = \frac{\rho u l}{\mu} \tag{2.11}$$

where $\rho$ is the fluid density, l is a characteristic length scale, u is the fluid velocity, and $\mu$ is the viscosity of the fluid. The Reynolds number is most commonly used to categorize laminar, transitional or turbulent flow regimes. It's importance regarding atomization lies with the fact that it is a measure of how turbulent the phases are. At low Re values, the viscous forces damp disturbances and the flow remains laminar. At higher Re values, this is no longer the case and past a certain threshold the flow becomes fully turbulent. Since disturbances play a central role in the process of atomization, the Re of the interacting fluids must be taken into account.

The **Ohnesorge number** (Oh) represents the ratio of internal viscosity to surface tension forces for a liquid. It is used as an indicator of jet or sheet stability [31]. The definition can be found in eq. 2.12:

$$Oh = \frac{\sqrt{We}}{Re} = \frac{\mu}{\sqrt{\rho \sigma l}} \tag{2.12}$$

Lefebvre et al. explains that due to inconclusive experimental results in the past, the role of Oh could not be consistently defined as related to droplet breakup [31]. The work of Faeth et al is mentioned as having provided some clarification of the role of Oh in droplet breakup. As seen in fig. 2.6, as Oh increases larger values of We are required in order to stay within the same breakup regime. It is also worth noting that Oh is a function of material properties

and length scale only. The data in Fig. 2.6 was attained via shock tube experiments, since shock wave disturbances provide a step type change in the gas properties around a drop. This is similar to what a droplet may experience at the end of primary breakup [18].

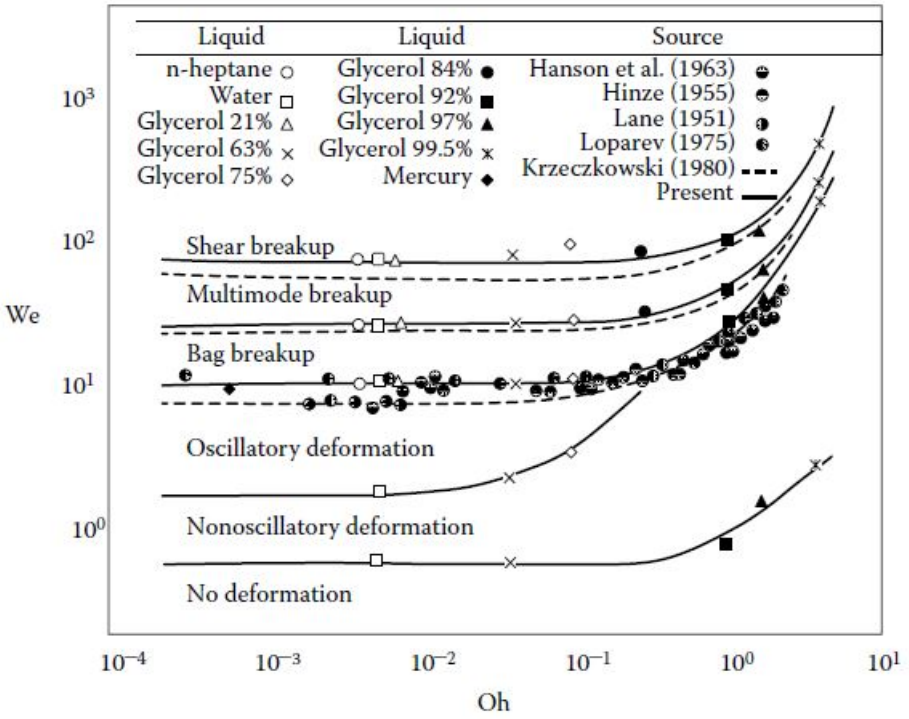


Figure 2.6: Drop breakup regime map from shock-tube experiments [18]

## 2.4. The Pintle Injector

As described by Dressler et al., the pintle injector concept relies on the injection of one propellant through an annular opening, centered around the pintle rod [16]. The second propellant flows axially between the pintle rod and its sleeve. At the end of the pintle rod, the second propellant is directed radially upwards via the geometry of the pintle tip. Consequently, the second propellant path intersects with the first and momentum is exchanged creating a circular, angled spray. The point at which the two propellants meet is known as the point of impingement. An example of a pintle injector axial cross-section schematic can be seen in Fig. 2.7:

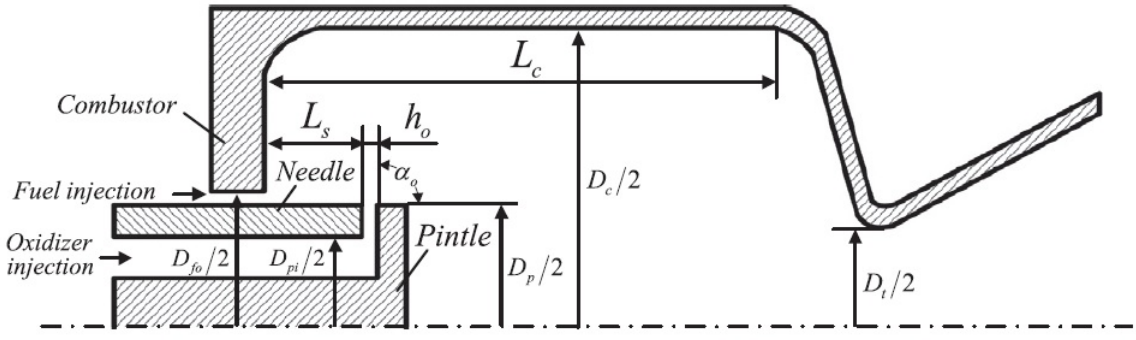


Figure 2.7: Combustion chamber axial cross-section [19]

The left side of the figure shows the openings for the oxidizer and fuel at the head-end of the combustion chamber. The pintle rod can be seen turning the central propellant (oxidizer in this case) towards the fuel stream at a 90 degree angle. The choice of oxidizer-centered or fuel-centered configuration is one of the important design decisions that can impact the performance of the injectors. Dressler et al. points out that there are three geometrical design choices for central propellant injection [16]:

1. a continuous gap is present between the pintle rod and its sleeve
2. slots or holes are present on the sleeve or the tip of the pintle rod
3. a combination of the previous two designs

The schematic seen in Fig. 2.7 is an example of the first option as the space between the pintle rod and its sleeve, labeled "$h_0$", is continuous. The movable pintle rod is a distinguishing feature of the injector, since it allows the variation of the injection area of the central propellant. Injectors using the second design choice for central propellant injection (radial holes or slots) are used for fixed thrust rockets only. This is because the injection area of the central propellant is not variable [16]. This is the type of injector being developed by the student rocketry group, DARE, at TU Delft. A noteworthy variation of the pintle injector is the "Face Shut-Off" variant, which allows changing the injection area of both propellants simultaneously, as seen in Fig. 2.8. The injector sleeve which does not appear in previous figures is clearly denoted here.

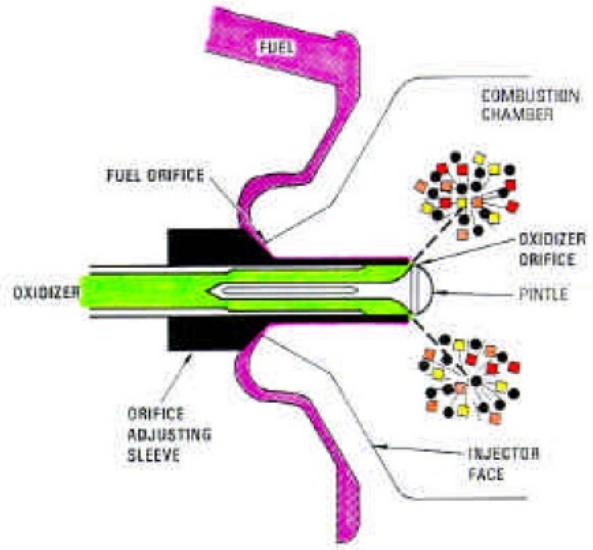


Figure 2.8: Injector geometrical parameters [16]

The simultaneous variation of the injection area of both propellants is achieved via a notch on the injector sleeve, near the annular propellant injection point. Moving the sleeve instead of the pintle will subsequently change both injection areas. In the context of geometry, it is worth discussing current design trends of pintle injectors. A variable that often changes between designs is the pintle impingement angle. This can be observed by comparing Fig. 2.7 (90 deg) and Fig. 2.8 (less than 90 deg). The reason for this variation has to do with the pintle impingement angle's influence on spray parameters. An additional common variation is that of the movable sleeve vs the movable pintle. The FSO (Face Shut Off) variants often involve movable sleeves due to the reasons explained above.

Considering the geometry and working principle of the pintle injector, one could argue that a coaxial injector is a limiting case of the pintle injector. A zero pintle impingement angle will result in a geometry that differs from that of a coaxial injector only by the presence

of the pintle rod. Considering the working principle of the pintle injector, one can see that atomization results from impingement and shearing effects between two fluid streams. The coaxial injector makes use of shearing only. For these reasons, it can be thought of as a simpler, limiting case of a pintle injector. The geometry essentially consists of two concentric pipes. Liquid propellant flows through the central one and gaseous propellant flows around it. A sketch of this can be seen in Fig. 2.9.

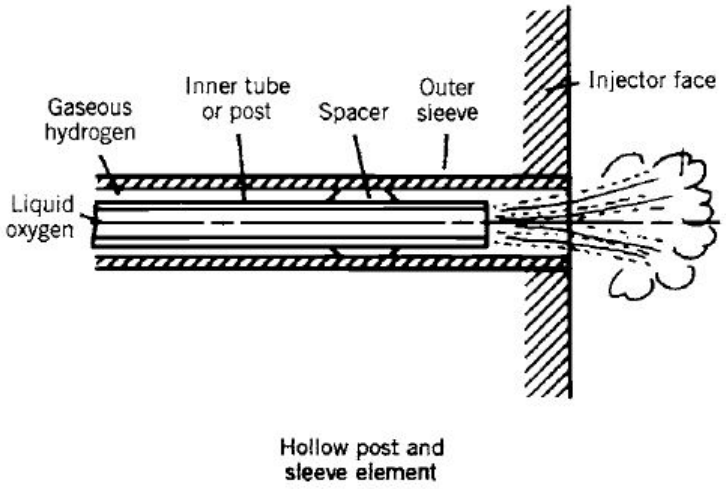


Figure 2.9: Coaxial injector sketch [59]

This type of injector has been used in many large rocket engines successfully [59]. One of it's drawbacks is its susceptibility to combustion instabilities. Much research has therefore been devoted to methods to alleviate this problem. Current research efforts include the exploration of Gas Centered Swirl Coaxial (GCSC) injectors and their potential to dampen pressure oscillations in the thrust chamber [7]. GCSC injectors are a variation of the coaxial injector where propellants are injected normal to the axis of the post to generate swirling flow.

A study of typical ranges of dimensionless quantities found in experimental studies of injectors indicated that coaxial injectors typically operate at higher Weber numbers than pintle injectors. The results can be seen in Table 2.2. It should be noted that the definitions of indicated parameters may vary from author to author. Cells marked with N/A indicate that parameters were not indicated clearly or not enough data was provided for their calculation. None of the works consulted have discussed the Ohnesorge number or its importance in liquid rocket injector applications. This data provides an order of magnitude estimate for typical dimensionless quantities found in experimental studies of the two presented injector types.

Table 2.2: Typical injection nondimensional parameters

| Reference | Injector type | Re (liquid) | We | Oh |
|---|---|---|---|---|
| Son et al. [58] | Pintle | N/A | 10-4500 | N/A |
| Son et al. [56] | Pintle | N/A | 1-180 | N/A |
| Son et al. [57] | Pintle | N/A | 10-120 | N/A |
| Murrone et al. [38] | Coaxial | 6.3e04 | 2.5e04 | 2.5e-03 |
| Gautam et al. [21] | Coaxial | 2.21e05 | 1.93e04 | 6.3e-04 |
| Tani et al. [60] | Coaxial | 1e05 | 1.1e05 | 3.4e-03 |

## 2.5. Current research - Liquid Rocket Injection Modeling

The submitted literature study by Pal contains a summary of recent numerical studies on pintle injectors [45]. Son et al. performed an axysimmetric simulation using an Eulerian multi-phase model (software or specific model not specified). Qualitative results of the flow-field were obtained as well as spray angles with errors of up to 25% relative to experiment [57]. Fang et al. injected an experimentally obtained droplet distribution into the domain of a combustion simulation [19]. Comments are made regarding possible methods to improve the geometry of the injector for higher efficiency based on observed flow patterns. The work of Radhakrishnan et al. also uses a model that injects droplets at the injector face [48]. Qualitative observations are made on the behaviour of mixing quality and spray cone angle with varying injection conditions. What these works have in common is that primary atomization is not accounted for and in certain cases experimental data is necessary to produce simulation results. Specifying droplet sizes and velocities (from experiment) as a boundary condition is the most commonly used technique in injection simulation to date. The described method of injecting a discrete second phase into a continuum is known as the Eulerian-Lagrangian method. All the works mentioned, so far, have used RANS turbulence models.

The works of Murrone et al. on simulating atomization in a coaxial injector discuss and showcase the difficulties of resolving primary and secondary breakup regimes in a single simulation [38][20]. In the introduction of the study, Murrone et al. articulates the need for numerical methods that are able to output spray properties using only the upstream variables as inputs (as opposed to fixing the characteristics of the spray as an input) [38]. Moreover, it is mentioned that the difficulty with atomization simulations lies with the range of scales that must be resolved (e.g. dense regime vs dilute regime). The study tackles this problem by using two custom Eulerian multi-phase solvers with an LES turbulence model. In the second work on the same topic, Murrone et al. shows preliminary results of a simulation that has not yet converged. The resources required for a 17ms simulation on a 10 million cell domain were roughly 1 million core-hours using 480 cores in parallel [20]. The work of Warncke et al. is not on rocket injectors, but serves as an additional example of the high computational expenses required to model primary atomization [66]. Warncke et al. used a hybrid DNS/LES turbulence formulation to model the primary atomization of an air-blasted liquid sheet. Results showed good agreement with experiment at the cost of high grid sensitivity. A different approach to the simulation of air-blasted liquid sheets can be found in the study by Zuzio et al. [69]. Direct Numerical Simulation is carried out using a hybrid multi-phase method that switches from a continuum to a discrete formulation for the liquid phase. This is done based on ligament size criteria. The technique allows for a computationally cheaper study, since the smallest droplets need not be fully resolved. Results have shown good qualitative agreement with experiment.

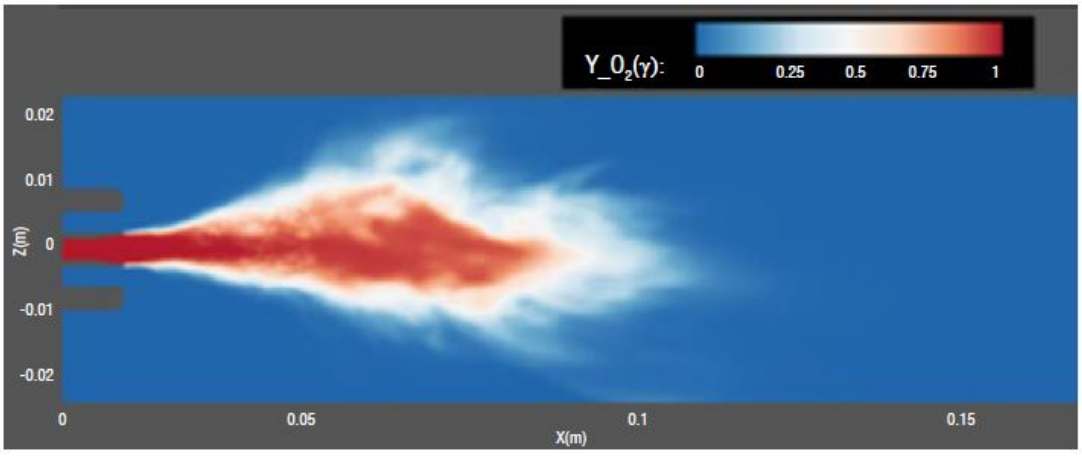


Figure 2.10: Coaxial injector simulation - liq. volume fraction [20]

The approach of solving equations of motion for discrete particles in a continuum is known

as the Eulerian-Lagrangian method. This is because the continuum phase uses an Eulerian reference frame which is fixed in space. The particles use a Lagrangian reference frame which means they are followed in time. A fully Eulerian simulation means that both phases are modeled as continuous. This means that the interface must be captured or tracked between the two fluids - this can become expensive as particle ligaments multiply and become smaller. This is the general approach used in the work of Murrone et al. [38][20]. Fig. 2.10 shows the mid plane volume fraction of liquid oxygen in a gaseous hydrogen\liquid oxygen coaxial injector. It quickly becomes apparent that as the volume fraction drops, capturing the shape of liquid ligaments can become prohibitively expensive. The model of Murrone et al. uses a diffuse interface capturing method to alleviate this problem [20].

To summarize the main points of the current state of the art of injection modeling, one can state the following:

- The most common modeling approach neglects primary atomization and injects discrete droplets at domain boundaries.
- Studies that model both primary and secondary atomization can be prohibitively expensive.
- There is a need for numerical methods that can affordably and accurately model the range of scales encountered in liquid rocket injector sprays.
- There is a need for numerical methods that can predict spray properties without using measurement data as input

The following chapter will discuss how the ”VOF-to-DPM” solver could be a potential solution for the mentioned challenges.

# 3

# Numerical model

The theory behind the numerical models used throughout the study are described in this chapter. The governing equations and the Finite Volume method are presented. An overview of turbulence modeling is given as a general guideline. The two multi-phase models that form the basis for the VOF-to-DPM solver are then described. The last section discusses the working principle and potential of the new solver.

## 3.1. Solution Approach and Governing Equations

Ansys Fluent uses the finite volume method to discretize the flow domain. As a result, a set of control volumes are produced for which conservation (transport) equations are solved. These equations are momentum and continuity at a minimum, but can include energy, species and other equations, depending on the problem [51]. Flow variables are calculated at the center of each cell and face values are interpolated. This section will briefly present the continuity and momentum equations.

The momentum equation for a Newtonian fluid using vector notation takes up the following form [51]:

$$\frac{\partial}{\partial t}(\rho \mathbf{u}) + \nabla \cdot (\rho \mathbf{u} \otimes \mathbf{u}) = -\nabla p + \nabla \cdot [\mu(\nabla \mathbf{u} + \nabla \mathbf{u}^T) - \frac{2}{3}\nabla \cdot \mathbf{u} I] + \rho \mathbf{g} \tag{3.1}$$

where user defined sources are excluded and the following notation applies:

- $p$ - pressure
- $\rho$ - density
- $\mathbf{u}$ - velocity
- $\mu$ - dynamic viscosity
- $I$ - identity matrix
- $\mathbf{g}$ - gravity

The T subscript seen in $\mathbf{u}^T$ represents the transpose of the velocity vector. (Note: there is a typo in the divergence term of the Ansys Theory guide) The bold notation is used to indicate vectors. The two terms on the left hand side of eqn. 3.1 represent inertial forces. On the right hand side, the first term represents pressure forces and the second and third stand for viscous and gravitational forces respectively. In two-phase flow simulations, there is sometimes a source term on the right hand side of the momentum equation for one or more phases. This would be the case, for example, if two-way coupling were used in the current study. Two-way coupling takes into account the effect of the discrete phase on the continuum phase. For the current study, one way coupling was used. For this reason, there is no source term shown in eqn. 3.1.

The continuity (mass conservation) equation can be found below [51]:

$$\frac{\partial \rho}{\partial t} = \nabla \cdot (\rho \mathbf{u}) + S_m \tag{3.2}$$

where the $S_m$ term is a source term for mass from other phases (eg. droplet vaporization) or user defined sources. Later sections will clarify the role of the mass source term in the solver used herein. The governing equations are integrated per control volume to obtain a set of algebraic equations for the dependent variables (flow variables). These equations are then linearized and solved as a system of linear equations to yield the dependent variables.

The momentum and continuity equations simplify significantly for incompressible flow. This is due to the condition of constant density for such a flow regime. The incompressible momentum and continuity equations can be found in eqns. 3.3 & 3.4 respectively:

$$\frac{\partial \mathbf{u}}{\partial t} + \nabla \cdot (\mathbf{u} \otimes \mathbf{u}) = -\frac{1}{\rho}\nabla p + \nu(\nabla^2 \mathbf{u}) + \mathbf{g} \tag{3.3}$$

$$\nabla \mathbf{u} = S_m \tag{3.4}$$

where $\nu$ is the kinematic viscosity, defined as the ratio of dynamic viscosity and density.

## 3.2. Turbulence Modeling

The concept of turbulence, its relevance and the models used to account for it are discussed in this section. Due to the complexity and depth of this topic, the discussion is mostly limited to a conceptual level. With practicality in mind, only those aspects of the presented theory which are believed to influence the results significantly are discussed in more detail.

Lesieur defines turbulent flow as a flow that is disorderly in time and space, but notes that this definition is not a precise mathematical one [33]. Lesieur explains that turbulent flow must have three properties:

- Unpredictability - a small uncertainty regarding the flow at an initial time will amplify to the point where a deterministic prediction of its evolution is impossible
- Mixing behaviour - the flow should mix transported quantities more rapidly than molecular diffusion alone
- Scale - the flow must contain a wide range of spatial wavelengths

These three flow properties motivate the importance of turbulence modeling when attempting to simulate atomization. If the goal is to predict droplet sizes, positions and velocities, then it is easy to see how the turbulent properties of the flow have significant influence. The unpredictability of the flow gives way to unpredictability in droplet sizes. The mixing behaviour and range of spatial scales drive the spreading of the droplets, as well as their breakup. The Reynolds number is the non-dimensional parameter used to determine if the flow can be considered turbulent or laminar.

There are three main categories of turbulence models [62]:

- **Reynolds Averaged Navier Stokes (RANS)** - as the name suggests, these models work with the Reynolds Averaged Navier Stokes equations. Only mean flow components are solved for and the fluctuating components are modeled. Due to the averaging of the governing equations, additional unknowns show up in the system of equations. This results in too many unknowns and for this reason RANS turbulence equations are used to close the set of governing equations. The most well known RANS turbulence model is the k-$\epsilon$ model. This approach is the least computationally expensive out of the three.
- **Large Eddy Simulation (LES)** - As opposed to RANS models, LES simulations solve for the large scale turbulent structures in the flow. A spatial filter is applied to the governing equations, resulting in a decomposition into resolved scales and sub-grid scales. Conceptually, the difference between RANS and LES lies in that LES solves for turbulent

scales above a certain filter size, whereas RANS models all turbulent scales. LES solves for unsteadiness in the flow, which is one of several reasons why it is significantly more expensive computationally than RANS methods.

- **DNS (Direct Numerical Simulation)** - DNS methods solve for the mean flow and all the turbulent velocity fluctuations. This is done by using grids that are sufficiently fine to resolve turbulent scales down to the Kolmogorov length and time-steps small enough to resolve the finest turbulent velocity fluctuations. This technique requires extensive computing power. For this reason it is not often used in industry.

This work makes use of the first two methods, which are briefly discussed in the following sections.

### 3.2.1. RANS models

The **RANS** equations are derived by starting from a decomposition of the instantaneous velocity into a mean and a fluctuating component, this is known as Reynolds decomposition:

$$\mathbf{u} = \overline{\mathbf{u}} + \mathbf{u}' \tag{3.5}$$

Eq. 3.5 is substituted into the momentum equation, which will then result in 6 unknown terms that must be modeled. These are known Reynolds stresses and they are: $-\rho\overline{u'^2}$, $-\rho\overline{v'^2}$, $-\rho\overline{w'^2}$, $-\rho\overline{u'v'}$, $-\rho\overline{u'w'}$, $-\rho\overline{v'w'}$. It is the goal of the RANS turbulence equations to predict these Reynolds stresses in order to solve the closure problem [62].

RANS models are classified based on the number of additional scalar transport equations that must be solved in addition to the RANS equations. Fig. 3.1 by Versteeg et al. shows the most common RANS models and the number of additional equations that need solving:

| *No. of extra transport equations* | *Name* |
|---|---|
| Zero | Mixing length model |
| One | Spalart–Allmaras model |
| Two | $k$–$\varepsilon$ model |
| | $k$–$\omega$ model |
| | Algebraic stress model |
| Seven | Reynolds stress model |

Figure 3.1: Common RANS models [62]

All of the above models except the Reynolds Stress Model, are classified as linear eddy-viscosity models. These are based on a constitutive relationship between stress and strain rate known as the Bousinessq hypothesis. This is seen in Eq. 3.6 using index notation [62]:

$$\tau_{ij} = -\rho\overline{u'v'} = \mu_t\left(\frac{\partial u_i}{\partial x_j} + \frac{\partial u_j}{\partial x_i}\right) - \frac{2}{3}\rho k\delta_{ij} \tag{3.6}$$

,where $\mu_t$ is eddy viscosity, k is turbulent kinetic energy per unit mass and $\delta_{ij}$ is Kronecker's delta (a.k.a. Identity matrix). The turbulent kinetic energy (TKE) per unit mass is defined as:

$$k = \frac{1}{2}\left(\overline{u'^2} + \overline{v'^2} + \overline{w'^2}\right) \tag{3.7}$$

The hypothesis is based on an analogy between Reynolds stresses and the Newtonian strain rate tensor which has the same form as eq. 3.6. Using this analogy, an eddy viscosity is proposed that acts similarly to the fluid viscosity. It is important to note that in order for eq. 3.6 to be valid, turbulence must be assumed to be isotropic. In other words, the

velocity fluctuations have the same magnitude in all directions. It is also visible that the eddy viscosity is assumed to be the same in all directions. This has been shown not to be true in many flow types [62].

At this point the basic concepts and assumptions behind linear eddy viscosity models have been presented. The derivations and equations for the turbulence models presented in Fig. 3.1 are well documented in literature and will not be discussed here for the sake of brevity.

### 3.2.2. Large Eddy Simulation

As explained by Versteeg et al., large and small eddies have significantly different behaviour [62]. Large eddies are anisotropic and their behaviour is dictated by the geometry of the flow. Smaller eddies are close to isotropic and their behaviour tends to be uniform (for sufficiently large Reynolds numbers). The nature of RANS models dictates that all eddies be described by a single turbulence model. This is not advantageous since the largest eddies depend on the problem at hand. Versteeg et al. further states that LES models approach this issue by solving for the larger eddies and modeling the smaller ones in a time-dependent simulation.

As opposed to the time-averaging implemented in RANS models, LES uses spatial filtering for separation of scales. A cut-off width is selected and all eddies larger than this width are resolved. The unresolved smaller eddies will produce what are referred to as sub-grid-scale (SGS) stresses analogus to the appearance of Reynolds stresses in RANS equations. The effects of the unresolved eddies on the resolved flow are accounted for by using SGS models.

Spatial filtering is performed via a filtering function. When using the Finite Volume Method, it is common practice to define a cutoff width $\Delta$ that is the cubed root of the cell volume:

$$\Delta = \sqrt[3]{\Delta x \Delta y \Delta z} \tag{3.8}$$

It is worth noting that due to the Finite Volume formulation, it does not make sense to define a cutoff width that is smaller than the side of one cell. The derivation of the governing equations is analogus to that of the RANS model, except the decomposition of flow variables is done into filtered and subgrid components per eq. 3.9:

$$\phi = \overline{\phi} + \phi' \tag{3.9}$$

,where $\phi$ is a flow variable and the overline represents the spatially filtered component. Substituting eq. 3.9 will yield a set of momentum equations that contain three sets SGS stresses. One of these has the form of the Reynolds stresses seen previously. The other two are referred to as Cross stresses and Leonard stresses. It is these three sets of stresses that SGS models attempt to predict. Similarly to RANS, the Bousinessq hypothesis is used to define an eddy viscosity. This eddy viscosity is analogus to the turbulent viscosity used in RANS.

Ansys Fluent offers a number of turbulent SGS models for eddy viscosity in release 19. These can be found below, in order of increasing complexity:

- Smagorinsky-Lilly
- Dynamic Smagorinsky-Lilly
- Wall-Adapting Local Eddy-Viscosity (WALE)
- Algebraic Wall-Modeled LES Model (WMLES)
- Dynamic Kinetic Energy Subgrid-Scale

A detailed discussion on the differences between the different models is beyond the scope of this work. Conceptually however, the differences between the models have to do with their behaviour near the wall and the complexity of the eddy viscosity equation. Several models have empirical coefficients that may need adjusting depending on the problem to be solved. One of the challenges that all models face is a high resolution requirement near the wall,

which is why commonly LES simulations require a larger number of cells compared to RANS simulations. Some models attempt to address this problem using different approaches [1].

Ansys Fluent also offers a range of hybrid RANS-LES models specifically designed to reduce the high resolution requirement of LES near the walls. The RANS formulation is used near wall boundaries and the LES formulation is used in the core flow. These models are the Detached Eddy Simulation (DES), Shielded Detached Eddy Simulation (SDES) and the Stress Blended Eddy Simulation (SBES). It is pointed out in the Ansys Theory Guide that the reason it is possible to switch from a RANS to an LES formulation with ease, is that the momentum equations are identical for both models. The difference lies in the formulations used for predicting the eddy viscosity.

### 3.2.3. Model selection

The criteria that were considered during turbulence model selection are as follows:

- Stability - Is it stable when used with the selected solver? (VOF-to-DPM)
- Ansys recommendation - What models did Ansys use in their benchmarking studies?
- Computational demand - How many equations are solved? How many iterations are required for convergence?
- Physical basis - What is the physical reasoning behind the model derivation?

Table 3.1 shows the trends among turbulence models based on the aforementioned criteria in a graphical trade-off format. The models recommended by Ansys were considered separately, since the solver is new and not much data is available on its performance and behaviour. For this reason, the recommendation of the authors of the VOF-to-DPM model carried significant weight in the decision-making process.

Table 3.1: Graphical Turbulence Model Trade-off

| | Stability | Comp. Demand | Physical basis |
|---|---|---|---|
| RANS | Case dependent | Low | Only solves mean flow |
| LES | Case dependent | Significant vs RANS | Resolves large scales |
| Hybrid RANS-LES | Case dependent | Lower than LES | Resolves large scales |
| DNS | Stable if set up correctly | Very high | Resolves all scales |
| Excellent | | | |
| Good | | | |
| Correctable deficiencies | | | |
| Unacceptable | | | |

Table 3.1 only shows a high level trade-off and does not address the particular turbulence models within each category (RANS, LES etc.) The decision making process in the case of the particular models was based on observations made in the Ansys Theory Guide and throughout literature on the performance of each model.

The following models are recommended for use with the VOF-to-DPM solver in a 2018 webinar presenting the new solver [52]:

- Scale Adaptive Simulation (k-$\omega$ variant)
- k-$\omega$ SST with SBES - RANS-LES hybrid model
- LES with WMLES SGS model

To summarize, there is one model recommended for each category (DNS not relevant in this case). Considering the presented trade-off results and the available time and resources for the project, the hybrid RANS-LES model was chosen for the simulations.

## 3.3. Volume of Fluid Model

The Volume of Fluid (VOF) model can model the flow of two or more immiscible fluids. A single set of momentum equations is solved together with volume fraction equation(s) to track the volume(s) of different fluids throughout the domain.

### 3.3.1. Volume fraction equation

The volume fraction equation assumes the form shown in eq. 3.10, according to the Fluent 19.2 Theory Guide[1]:

$$\frac{1}{\rho_b}[\frac{\partial}{\partial t}(\alpha_b \rho_b) + \nabla \cdot (\alpha_b \rho_b \mathbf{u}_b) = \sum_{a=1}^{n}(\dot{m}_{ab} - \dot{m}_{ba})] \tag{3.10}$$

where the following notation applies:

- $\rho_b$ - phase b density
- $\alpha_b$ - phase b volume fraction
- $\mathbf{u}_b$ - phase b velocity
- $\dot{m}_{ba}$ - mass transfer rate from phase b to phase a
- $\dot{m}_{ab}$ - mass transfer rate from phase a to phase b

The volume fraction of the primary phase is obtained from the constraint seen in eq. 3.11 below[1]:

$$\sum_{b=1}^{n} \alpha_b = 1 \tag{3.11}$$

In essence, the VOF model solves a continuity equation (eq. 3.10) for the volume fraction of one fluid (in a two fluid simulation). The value of the volume fraction $\alpha$ is 1 in cells that contain only liquid and 0 in cells that contain only gas, for a case of gas-liquid flow where gas is selected as the primary phase. The volume fraction of the second fluid is found via the necessity of the volume fractions to add up to unity in each cell (eq.3.11). It is worth noting that a single set of momentum and turbulence equations is solved when using the VOF model (in addition to eq. 3.10). All material properties and scalars (i.e. turbulence quantities) are averaged using the volume fraction.

Fluent provides two options for solving the volume fraction equation: implicit and explicit. The explicit method is more accurate, but it is subject to stability criteria [1]. The primary advantage of the implicit formulation is that a higher time step can be used (unlike the explicit case where large timesteps will cause instability). The drawbacks are higher levels of numerical diffusion and truncation error limitations. For a transient simulation, where the accuracy of the interface is essential, the explicit method is the more relevant one based on its mentioned properties.

### 3.3.2. Fluid Interface Reconstruction

The Geometric Reconstruction scheme was used in all simulations. This method makes use of a piece-wise linear reconstruction of the gas-liquid interface. A visual representation of this can be seen in fig. 3.2 below:

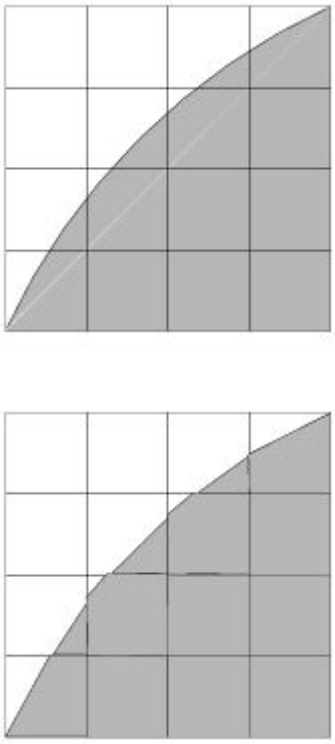


Figure 3.2: Geometric Reconstruction scheme concept [51]

The Ansys Theory Guide [51] states that when a cell is completely filled with one phase or another, standard interpolation schemes are used. The Geometric Reconstruction scheme is used when a cell is near the interface. The model assumes that each cell contains a linear interface between two fluids. The linearly shaped interface is then used to calculate advection of fluid through cell faces. There are three steps to the process of interface reconstruction:

1. The position of the linear interface relative to the cell center is calculated based on the value of the volume fraction and its derivatives for the given cell.

2. The amount of advecting fluid is calculated based on the computed linear interface and velocity values normal and tangential to it.

3. Using the fluxes calculated in the second step, volume fractions in neighbouring cells are calculated.

### 3.3.3. Material Properties

In multi-phase simulations using the VOF model, material properties in each cell are weighted by volume fraction.For a two fluid system, the equation for density is represented by eq. 3.12 below [1]:

$$\rho = \alpha_a \rho_a + (1 - \alpha_b)\rho_b \tag{3.12}$$

For a system of n liquids, the generalized equation would be eq. 3.13 below [1]:

$$\rho = \sum_{a=1}^{n} \alpha_a \rho_a \tag{3.13}$$

All other material properties (viscosity etc.) are computed as shown above.

### 3.3.4. Surface Tension

There are two available models for surface tension modeling in Ansys Fluent 19.2 : *Continuum Surface Force (CSF)* and *Continuum Surface Stress (CSS)*.

The CSF model is based on the work of Brackbill et al. [11]. The implementation of this model is based on a source term being added to the momentum equation. The extra term is expressed as a volume force and is a function of the curvature of the interface, the volume fraction gradient, the surface tension coefficient and the densities of the two fluids.

The CSS model is a conservative model of surface tension, as opposed to the CSF model [1]. The main difference between the two models has to do with the calculation of surface tension. The CSS model does not explicitly calculate surface tension, which means that it can perform better in underresolved regions. For the same reason, it does not require additional terms when modeling variable surface tension [51]. Based on the information found in the Fluent Theory Guide, it would appear that the CSS model only has advantages over the CSF model.

Nadooshan et al. states that the shortcomings of both the CSF and CSS models are the spurious velocity oscillations produced at the interface due to an inconsistent calculation of the surface tension force [39]. In a study of 6 different surface tension models, it was shown that for surface tension dominated flows, the CSS model marginally outperforms CSF model. Specifically, it produces smaller magnitude oscillations at the interface.

The work of Wang identifies an equation in the derivation of the CSF model that is not fully mathematically correct [64]. It is mentioned that when using the CSF model, the pressure difference at the interface depends on the density difference which is not physical. Finally, it is concluded that there are significantly more accurate ways of calculating the curvature of the interface than the method used in the CSF model.

Based on the presented information on the CSF model, it would appear that the CSS model is the superior of the two. In addition, literature indicates that both models have shortcomings that other models do not exhibit [39]. The CSS model was used for the purpose of this work, as the better of the two available models.

## 3.4. Discrete Phase Model

The purpose of this section is to describe the theory behind the discrete phase model. This includes the particle equations of motion and associated solution methods, turbulent dispersion theory and droplet break-up modeling.

### 3.4.1. Particle equations of motion

The force balance on a particle in a Lagrangian reference frame can be seen in eq. 3.14 below[1]:

$$m_p \frac{d\mathbf{u}_p}{dt} = m_p \frac{\mathbf{u} - \mathbf{u}_p}{\tau_p} + m_p \frac{\mathbf{g}(\rho_p - \rho)}{\rho_p} \tag{3.14}$$

where the following notation applies:

- $m_p$ - particle mass
- $\mathbf{u}$ - fluid velocity
- $\mathbf{u}_p$ - particle velocity
- $\rho$ - fluid density
- $\rho_p$ - particle density
- $\tau_p$ - particle relaxation time

The particle relaxation time, $\tau_p$ is defined as:

$$\tau_p = \frac{\rho_p d_p^2}{18\mu} \frac{24}{C_d Re_r} \tag{3.15}$$

where $\mu$ is the kinematic viscosity, $d_p$ is the particle diameter and $Re_r$ is the relative Reynolds number defined as:

$$Re_r \equiv \frac{\rho d_p |\mathbf{u}_p - \mathbf{u}|}{\mu} \tag{3.16}$$

The first term on the right hand side (RHS) of eq. 3.14 represents the drag force acting on the particle. The second term is the gravitational term including buoyancy and the third represents additional forces to be included in the model. The particle relaxation time seen in the first term on the RHS is obtained from a force balance on a spherical particle in gaseous flow. It is equal to the time it takes for the particle to reach 63% of the free-stream velocity. This parameter is a strong function of the particle size [14].

The drag coefficient is determined by an empirical relationship from the work of Morsi et al. [37]. Referred to as the "spherical drag law" in the Ansys Theory Guide, it uses $Re_r$ and three empirical parameters (a1-a3) to calculate the drag coefficient [51]. The empirical parameters are adjusted based on the relative Reynolds number range. For further details, the reader is referred to the work of Morsi et al. [37]. The drag coefficient relation can be found in Eq. 3.17:

$$C_d = a_1 + \frac{a_2}{Re_r} + \frac{a_3}{Re_r^2} \tag{3.17}$$

### 3.4.2. Integration of particle equations of motion

Particle trajectories and velocities are obtained from the velocity and force balance equations labeled 3.18 & 3.19 respectively:

$$\frac{d\mathbf{x}}{dt} = \mathbf{u}_p \tag{3.18}$$

$$\frac{d\mathbf{u}_p}{dt} = \frac{1}{\tau_p}(\mathbf{u} - \mathbf{u}_p) + \mathbf{a} \tag{3.19}$$

where x is the position vector and a is the sum of additional accelerations acting on the particle.

There are four discretization methods available:

- Analytic
- Euler implicit
- Trapezoidal
- Runge-Kutta

The main differences between the methods have to do with stability versus accuracy. The Fluent Theory guide provides some guidelines on the pros and cons of the different schemes. These are summarized below [1]:

- The analytic scheme is efficient, but becomes inaccurate for large steps and in cases where the particles are not in hydrodynamic equilibrium with the continuum phase.
- The Runge-Kutta scheme is recommended if the magnitudes of forces other than the drag force change along particle integration steps
- The trapezoidal and Runge-Kutta schemes must be limited to a stable range of step sizes

Fluent has a built-in feature that switches between two user selected methods (higher-order and lower order) depending on the step size in order to balance accuracy with stability. This is useful because higher order schemes are conditionally stable, but more accurate.

### 3.4.3. Turbulent Dispersion of Particles

The Discrete Random Walk (DRW) model is used to calculate the effects of turbulent dispersion on the discrete phase. This is the only model compatible with the VOF to DPM solver in Ansys Fluent 19. The following paragraphs will briefly present the concepts behind the model, which is based on the work of Gosman et al [25].

The first important assumption made in the DRW model is that turbulence is isotropic. In other words, the fluctuating velocity components of the flow are statistically uniform in all three directions. It is assumed that the fluctuating velocity magnitude can be described by a Gaussian probability distribution with a standard deviation equal to $\sqrt{|\mathbf{u}'|^2}$, where the instantaneous velocity can be written as seen in eqn. 3.20:

$$\mathbf{u} = \overline{\mathbf{u}} + \mathbf{u}' \tag{3.20}$$

It is assumed that droplets interact with turbulent eddies found in the flow field. The interaction time is determined based on the premise that one of two scenarios can occur:

1. The droplet moves slow enough inside the eddy that it remains in it for the whole eddy lifetime

2. The droplet has a high slip velocity and traverses the eddy in less time (defined as transit time $t_r$) than the eddy lifetime

The interaction time is then defined as the minimum of the eddy lifetime and the transit time. The eddy lifetime is a function of the integral time scale (T) of the flow-field. The integral time scale is a representation of a length of time for which the velocity is closely correlated with itself in a given region of the flow.

The transit time is a function of the particle relaxation time, the relative velocity between the flow and the particle as well as the eddy length scale (size of the largest eddies present in the flow). The particle relaxation time is a measure of how quickly a particle of a given size reacts to being disturbed by the surrounding flow.

To summarize, the DRW model accounts for the effects of the turbulent velocity fluctuations on the discrete phase. A fluctuating velocity magnitude is selected from a Gaussian probability distribution. Two interaction times are calculated (between the particle and the fluctuating velocity component), the smaller of which is implemented. The effect of the fluctuating velocity component is then accounted for in the particle trajectory calculation for the duration of the selected interaction time.

### 3.4.4. Droplet breakup modeling - WAVE model

The WAVE model is based on the work of Reitz [49]. The Ansys Fluent Theory Guide specifies that the model is appropriate for injections at Weber numbers above 100 [1]. The purpose of the original model was prediction of atomization in high pressure sprays for diesel engines. It's been shown to predict SMD values accurately in the high velocity region close to the injection site [49].

The model assumes that droplet break-up is initiated by Kelvin-Helmholtz instabilities. Droplet properties are predicted using the wavelength and growth rate of these instabilities. The breakup time of a droplet is related to the growth rate of surface waves. The mass transfer rate from the parent droplet can be calculated using the breakup time. A new parcel is formed when the shed mass is equal to 5% of the original mass of the parent droplet. The new parcel shares all properties with the parent parcel (material properties, temperature, position) except radius and velocity. The new parcel is assigned a random velocity component in a plane orthogonal to the parent parcel plane of motion. The magnitude of the new parcel's velocity is the same as the parent parcel's. The momentum of the parent parcel is adjusted so that conservation of momentum is maintained [1].

The two parameters that the user specifies are the constants $B_0$ and $B_1$. $B_0$ has to do with the child drop size and is usually kept at .61. The breakup time $\tau_B$ is directly proportional to $B_1$, which means that $B_1$ determines how quickly the parent parcel loses mass. Typical range for $B_1$ is between 1 and 60, with a default value of 1.73 in Ansys Fluent.

The $B_1$ parameter is assumed by the author of the model to be a characteristic of the initial disturbance level generated by the injector nozzle. In other words, this constant must be empirically determined for each injector [49].

### 3.4.5. Droplet breakup modeling - TAB model

The Taylor Analogy Breakup (TAB) model was developed by O'Rourke et al. [43]. The documentation for Fluent specifies that it is well suited for low Weber number applications [51]. The working principle of the model relies on an analogy between an oscillating/distorting droplet and a spring-mass-damper system.

| Spring-Mass System | Distorting and Oscillating Droplet |
|---|---|
| restoring force of spring | surface tension forces |
| external force | droplet drag force |
| damping force | droplet viscosity forces |

Figure 3.3: Taylor analogy [51]

Fig. 3.3 shows the analogy between the forces in a spring-mass-damper system and the droplet [51]. The dependent variable becomes the displacement of the droplet equator. Breakup is assumed to occur when the displacement of the droplet equator reaches a factor of 0.5 of its original radius. It is also assumed that the droplet has only one (fundamental) oscillatory mode. Fig. 3.4. shows the breakup mechanism assumed in the TAB model, where x stands for the displacement of the droplet equator and $r_0$ for the undisturbed droplet radius.

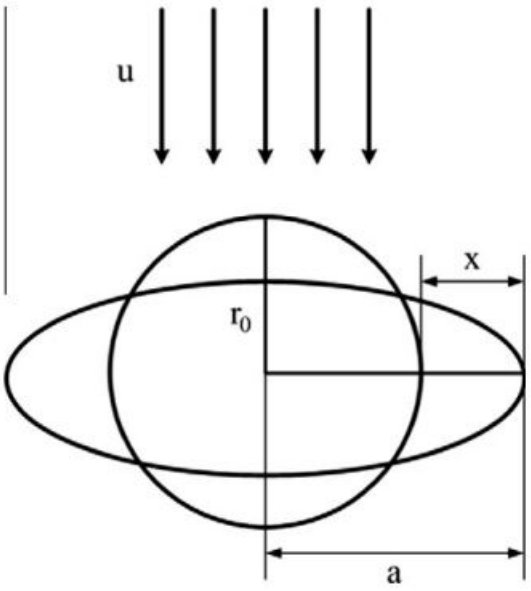


Figure 3.4: TAB model concept [30]

The sizes of the child droplets are determined via energy conservation. The energy of the parent droplet is assumed to be the sum of its minimum surface energy and the energy in oscillation and distortion. Since only oscillation in the fundamental mode is modelled, a factor K (of the order 10/3) is used to account for the energy contribution of other oscillatory modes. This factor must be determined experimentally and varies based on Weber number

regime. The child droplet radius obtained from the energy balance is used as the SMD value for a Rosin-Rammler distribution with a spread parameter of 3.5. In other words, the radii of the child droplets is sampled from a Rosin-Rammler distribution. A velocity normal to the travel direction of the parent droplet is imposed on the formed child droplets. This velocity is proportional to the displacement velocity of the equator of the parent droplet. It is worth noting that the child droplets are assumed to be undistorted and non-oscillatory [51].

### 3.4.6. Gradient adaption

Dynamic mesh adaption is a useful way of resolving areas of interest in a flow-field that contain discontinuities, without excessively increasing the number of cells in the mesh. Ansys Fluent offers several methods for dynamic mesh adaption. The curvature-based method was used for the purpose of this study, based on a recommendation by the solver authors [52]. The curvature-based gradient adaption method is based on the work of Dannenhoffer et al., originally developed to resolve shockwaves [15]. The method is implemented in Ansys as seen in eqn. 3.21 below (in 2 dimensions) [51]:

$$|e| = (A_{cell})^{\frac{r_{vol}}{2}} |\nabla^2 \alpha| \tag{3.21}$$

,where e is the error function (adaption function value), $A_{cell}$ is the cell area and $r_{vol}$ is the volume weighting parameter. For the purpose of this study, the volume fraction ($\alpha$) is the scalar of interest, hence its presence in eqn. 3.21. For other cases, the volume fraction can be replaced by other scalar variables of interest in order to govern the adaption algorithm. In other words, for this study, the goal is to refine the mesh at the gas-liquid interface (where the volume fraction varies sharply). Refinement is carried out until the error function value dips below a user defined threshold.

The volume weight parameter can be set by the user. It varies between 0 and 1, but the recommended value is 1. If $r_{vol}$ is 1, then the magnitude of the laplacian of the volume fraction is weighted by a cell length scale equal to the length of one side of a rectangular cell. Weighting is necessary to avoid high error function values in adapted regions, preventing future refinements of coarse areas that have not yet been refined.

## 3.5. VOF-to-DPM solver

The VOF-to-DPM solver was released in early 2018 with the release of Ansys Fluent 19.0. The new solver is an attempt to satisfy a need to simulate atomization without the high computational cost of a pure VOF simulation. There are two traditional methods for simulations of liquid in a gaseous environment: the VOF method and the Eulerian-Lagrangian method, as described in sections 3.3 & 3.4. The VOF method tracks the interface between two fluids, whereas the Eulerian-Lagrangian model tracks particles dispersed in a continuous phase. The VOF-to-DPM solver switches between the two models to simulate both dense and dispersed flow regimes of atomization, while keeping computational costs down.

What makes the solver unique is the transition criteria it uses to switch models. The solver identifies and tracks liquid lumps (ligaments) in the VOF model. Lumps are classified based on asphericity and size criteria defined by the user. When two asphericity criteria and a diameter criteria are met, the liquid lump is converted into a discrete parcel. The two geometrical criteria for transition are a measure of the asphericity of the liquid lump or how closely it resembles a perfect sphere. The first asphericity criteria is the normalized radius standard deviation. The normalized radius is the distance between a facet centroid and the lump center of gravity, divided by the average radius. The second asphericity criteria is the average radius-surface orthogonality. It is defined as the relative orthogonality between the vector connecting the lump centroid to the facet centroid and the facet normal. These two vectors overlap in the case of a perfect sphere. Relative orthogonality ranges from 0 to 1 [52]. Fig. 3.5 shows an example of liquid lumps colored by the relative orthogonality asphericity criteria. The range is between 0.5 and 1 since the transition criteria was set to 0.5 during the simulation.

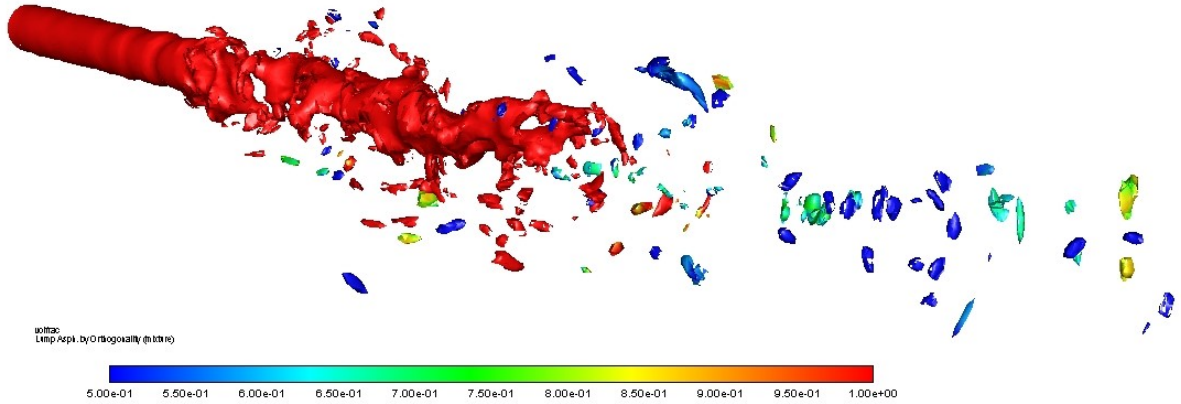


Figure 3.5: Liquid ligaments colored by asphericity

The cells where the transition occurred are filled with enough air to conserve volume [51]. The mass source term found in the continuity equation represents the added mass (see section 3.1). It is also unusual that the documentation mentions enforcing conservation of volume (as opposed to conservation of mass) [51]. Furthermore, it is stated that the mass source required to enforce volume conservation (in other words the mass source of gas added to the continuity equation) affects overall mass balance. It is unclear from the text, but one could deduce that mass is in fact not conserved when the transition occurs. It is the author's interpretation of the currently available documentation that mass is added to the overall system with every vof/dpm conversion. This occurs because all liquid is converted into a discrete particle in a cell and the volume that the liquid occupied is filled with gas.

It is unclear from the documentation, how the number of particles per parcel is calculated. Conversations with Ansys staff (through Ansys Student Community forum) have indicated that a single liquid lump is converted into a parcel containing a single droplet or less than one droplet based on a setting labeled : "Split any DPM Parcel that Exceeds the Cell Volume by Factor". This setting will be referred to as the Over-Fill Factor (OVF) from this point forward. This parameter controls the factor by which the volume of a converted DPM parcel may exceed the volume of its parent cell. This may happen in cases where the volume of the original cell size is less than that of the VOF ligament converted to the discrete phase. Based on the documentation, this feature is necessary to avoid too many parcels forming from a single ligament. Forming more parcels from one ligament can reduce instabilities in the continuous phase solution [51]. If the factor is set to a high value, then more ligaments will be converted to a single parcel containing a single droplet. A low value will mean that if the factor is exceeded, the ligament will be split into as many parcels as the number of cells that contain it, such that the mass of all the created parcels add up to the mass of the converted VOF ligament.

When used in conjunction with an adaptive mesh, the solver allows an efficient use of computational resources by coarsening the mesh after lumps are converted into the DPM. This can be seen in Figs. 3.6a & 3.6b below. Both figures show the 0.5 volume fraction isosurface (green) of a round liquid jet and the discrete particles formed. The circled areas indicate the location of a liquid lump that gets converted to the discrete phase. The mesh is refined based on the curvature of the gas-liquid interface. When the transition between the models occurs, the interface for the particular lump is eliminated and the mesh is coarsened to its original size. This method is a potential solution to the high computational cost of the VOF model in the dilute regime of gas-liquid flows.

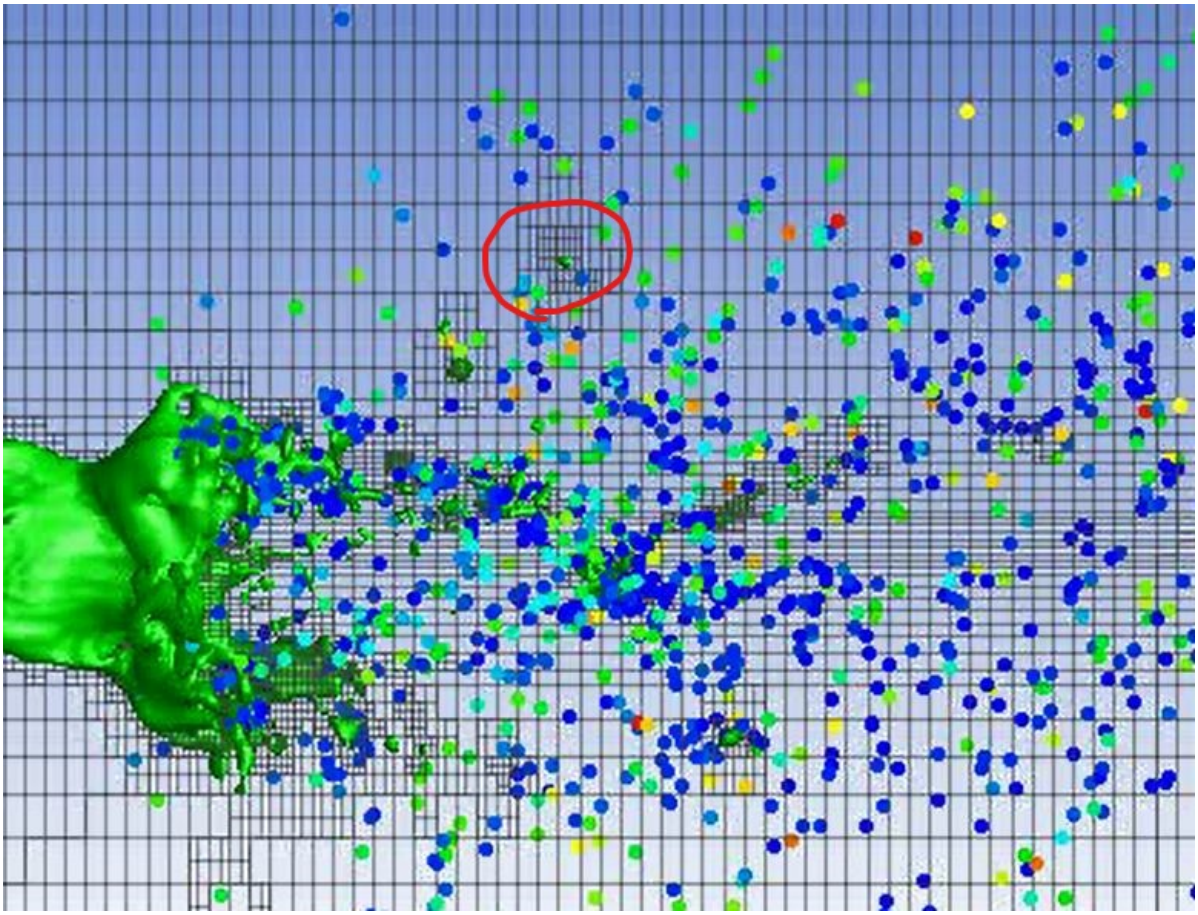

(a)

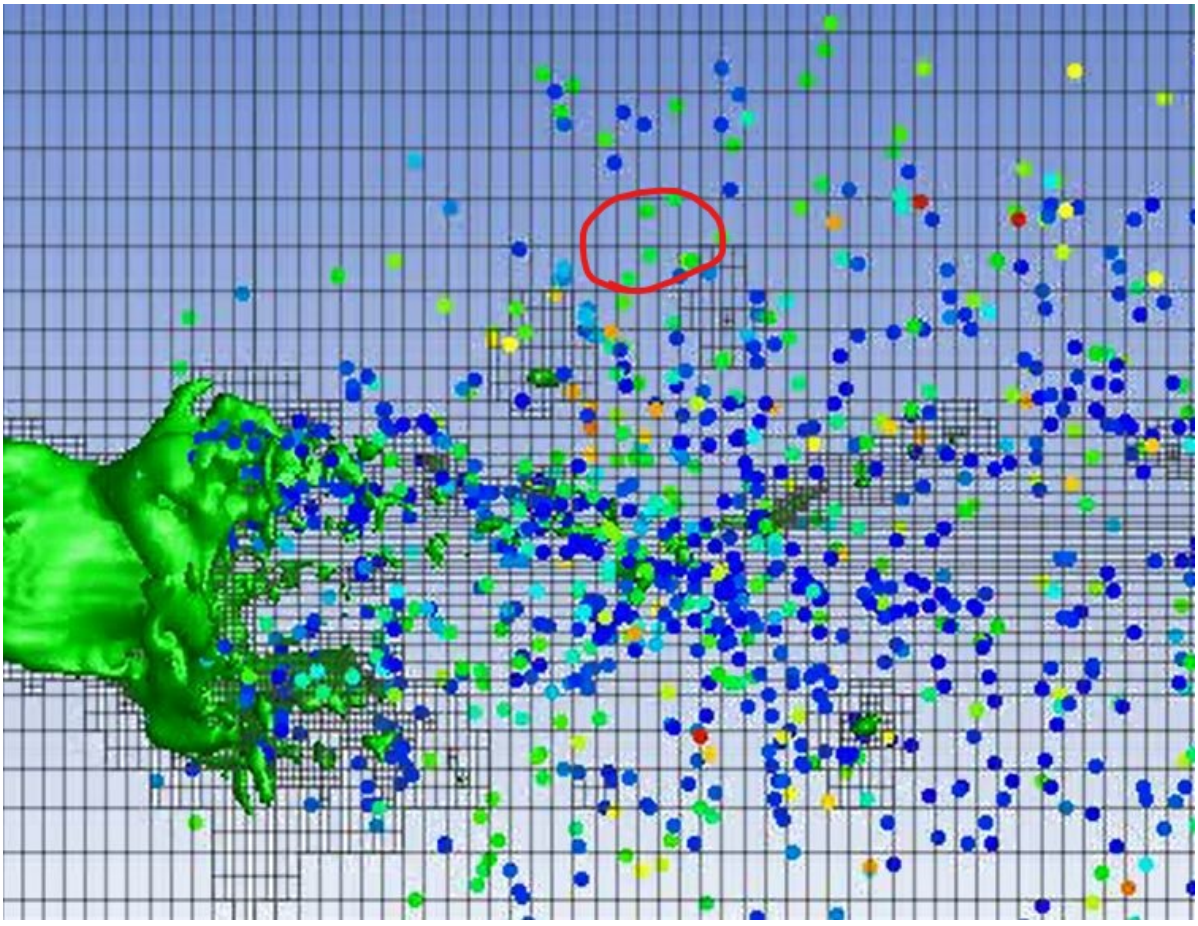

(b)

Figure 3.6: (a) Before transition (b) After transition

# 4

# Preliminary Work

One of the cases used by Ansys to validate the VOF-DPM solver is based on the work of Sekar et al. [54]. The topic is the well studied problem of a liquid jet injected into a gaseous crossflow. The reason why this problem is a good test case for spray modeling is due to the complex phenomena that can be observed: jet trajectory evolution, surface breakup, column fracture and particle dispersion [54]. It was the intent of the author to reproduce the simulation results shown by Ansys during a webinar during which the new solver is introduced [52]. Successfully reproducing Ansys' data would have proven the reliability of the solver and provided a test case to base future simulations on. This work was not completed, as the decision was made to use a case with better experimental data available for validation purposes. The goal of this chapter is to portray the difficulties encountered and some of the lessons learned.

## 4.1. Geometry and Domain

The experimental setup of Sekar et al. [54] is presented in detail in the work by Gopala et al. [24]. Fig. 4.1 illustrates the test section and the expected spray geometry.

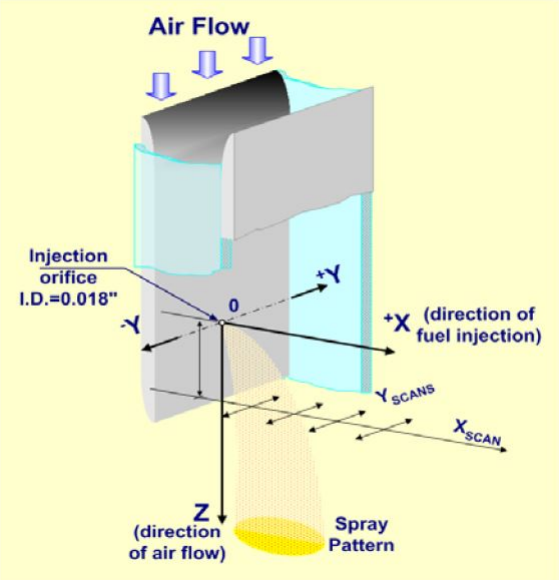


Figure 4.1: PDPA test section of Gopala et al. [24]

Jet A fuel is injected through a centered, circular orifice into a cross-flow of air. The test section contains two flat plates at the top and bottom. Glass plates on the sides allowed

visual access to the test chamber for a Phase Doppler Anemometry (PDA) system which would record droplet diameters and velocities.

Several simulations were carried out. The domain of the first simulation is represented in Fig. 4.2, viewed along the y direction using the coordinate system shown above. In the third dimension, the domain forms a rectangle with a total y dimension of 20mm. The distance between the inlet was modified for the second simulation. This was the only geometrical change made in later simulations. Changes between simulation setups in general will be discussed in subsequent sections.

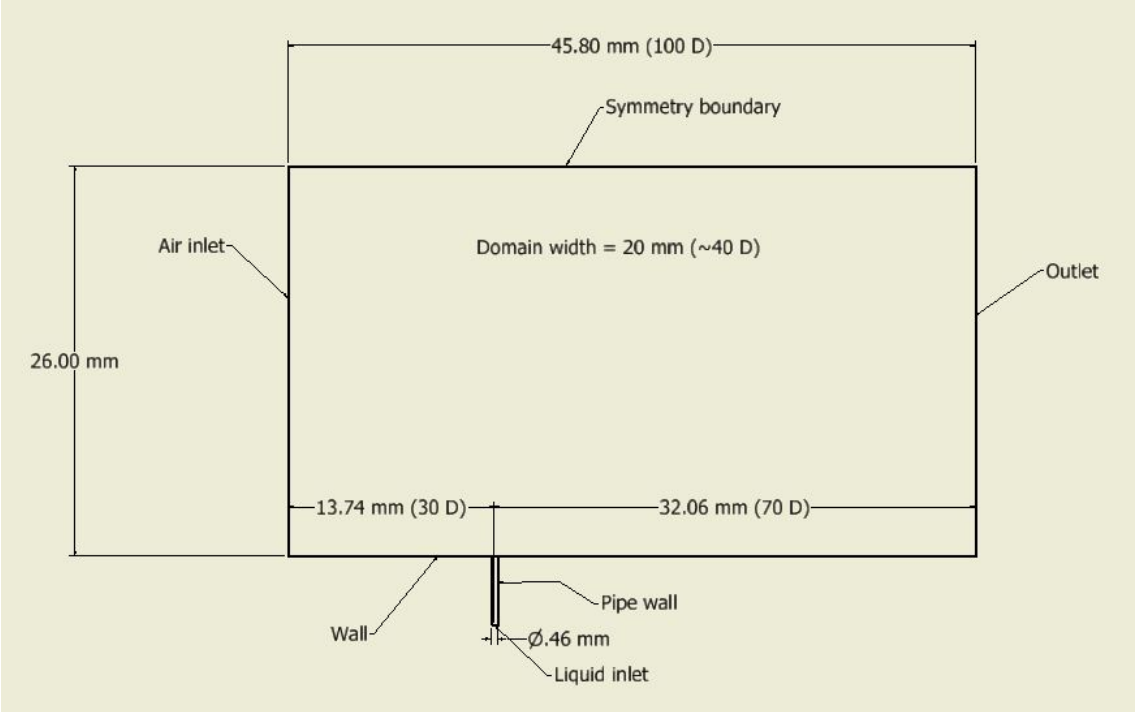


Figure 4.2: Simulation domain

For reference, Fig. 4.3 shows a side view of the simulation domain near the injection site. Liquid ligaments in the VOF description are shown in green and discrete particles in blue. The line on the left side is the air inlet and the one on the bottom is the bottom wall. The pipe walls are not shown.

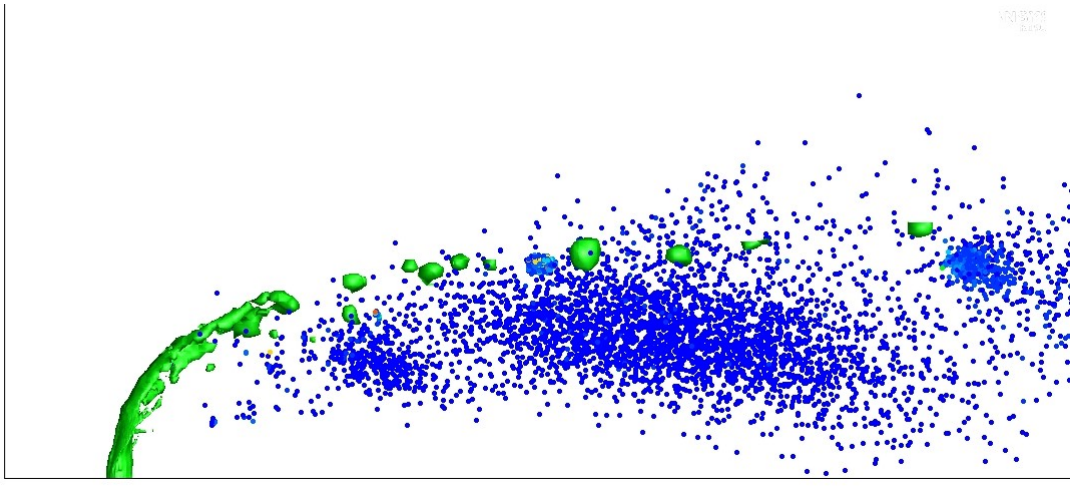

Figure 4.3: Simulation side view

Table 4.1 shows a comparison of the simulation domain size and the experimental test section size. The thickness of the plates in the test section is unclear from literature [24], so the height provided includes the thickness of both plates.

Table 4.1: Simulation vs Test dimensions

| | x | y | z |
|---|---|---|---|
| Measurements | 68.6mm (incl. plates) | 43.18mm | N/A |
| Simulation | 26 mm (excl. plates) | 20mm | 45.8mm |

## 4.2. Simulation setup

The boundary conditions used are listed in Table 4.2. The air inlet had a velocity inlet so as to allow for a profile to be used as an input. The outlet is a classic pressure outlet and the walls are no-slip, which means that velocity is zero at the walls. The top, front and back faces of the domain use the symmetry condition which is essentially a zero normal gradient condition for all variables. The normal velocity at a symmetry plane is set to zero. The liquid inlet has a mass flow rate boundary condition in order to ensure that a proper momentum ratio between liquid and gas are maintained. For further details on boundary condition definitions, the reader is referred to the Ansys Fluent Theory Guide [51].

Table 4.2: Simulation Parameters

| Boundary name | Boundary condition |
|---|---|
| Air inlet | Velocity Inlet |
| Outlet | Pressure Outlet |
| Pipe wall | No Slip Wall |
| Wall | No Slip Wall |
| Top | Symmetry |
| Front & Back (z dir) | Symmetry |
| Liquid Inlet | Mass Flow Rate |

A summary of key input values can be found in Table 4.3 below. These values match the experimental conditions [54]. The liquid velocity is based on the value used by Ansys in their test case [52].

Table 4.3: Simulation Parameters

| Parameter Name | Value |
|---|---|
| Liquid bulk velocity | $32m/s$ |
| Air bulk velocity | $105m/s$ |
| Liquid density | $780.6kg/m^3$ |
| Air density | $5.88kg/m^3$ |
| Liquid viscosity | $7e-04Pas$ |
| Chamber temperature | $300K$ |
| Absolute Pressure | $5bar$ |
| Surface tension | $.0197N/m$ |
| Weber number | 1500 |
| Liquid Reynolds number | 16414 |
| Jet Momentum Ratio (J) | 10 |
| Mesh topology | $Hexahedra\&Polyhedra$ |
| Mesh count | $500kcells$ |

Note that the Weber number is calculated using air velocity, air density and orifice diameter in this case (see Eq. 2.10). The Jet Momentum Ratio (J) is defined by Sekar et al. as the ratio of liquid to gas momentum seen in Eq. 4.1:

$$J = \frac{\rho_l U_l^2}{\rho_g U_g^2} \tag{4.1}$$

The values in Table 4.3 were chosen to match the values used by Ansys in their test case [52]. The default simulation settings used in all runs are detailed in table 4.4 below. These settings are shared by all simulation runs unless specified otherwise.

Table 4.4: Needle burner - simulation settings

| **Setting** | **Value** |
|---|---|
| Transient/Steady State | Transient |
| Gravity | -9.81 $m/s^2$ in X dir. |
| Pressure/Velocity Coupling | SimpleC |
| Gradient discretization | Least Squares |
| Pressure discretization | PRESTO! |
| Volume fraction discretization | Geo-Reconstruct |
| Momentum discretization | Second order upwind |
| Turbulent quantity discretization | First order upwind |
| Gradient adaption settings | Curvature Method; Standard Normalization; 3 Refinement Levels |
| Adaption algorithm | Hanging Node |
| Breakup model | WAVE w/ constants $B_0$=.61 , $B_1$=1.73 |
| Turbulent Dispersion Settings | DRW model w/ random eddy lifetime and $C_l$=.15 |
| Turbulence model | k-$\epsilon$ Realizable |
| Overfill factor | 10 |

The settings in Table 4.3 are provided for reproducibility and as a general guideline for future work. These were selected based on the recommendations of the Ansys manual and introduction webinar of the new solver [51][52]. The Breakup model and Turbulent Dispersion model are physical models that can be switched on or off. Turbulent dispersion was switched off for the first simulation.

Several simulations were performed in order to progress from a simple to a more complex model. The goal of the first simulation was to simply produce a distribution and a reasonably physical set of results. A summary of the set of simulations performed can be found in table 4.5 below, along with the changes implemented between simulations:

Table 4.5: Simulations summary

| Simulation nr. | Description |
|---|---|
| 1 | Simulation with uniform inlet velocity and WAVE breakup model |
| 2 | Implemented experimentally measured velocity profile at the inlet |
| 3 | Enabled turbulent dispersion |

The first simulation made use of a uniform velocity at the inlet of 105 m/s, to match the momentum flux ratio and the liquid velocity used by Ansys for solver validation. Simulation nr. 2 used a velocity profile at the inlet, obtained via measurement by Sekar et al. [54]. The velocity profile can be seen in Fig. 4.4 denoted by circular dots and labeled ”DATA”. This change was expected to influence the distribution significantly, since most of the jet is within the boundary layer.

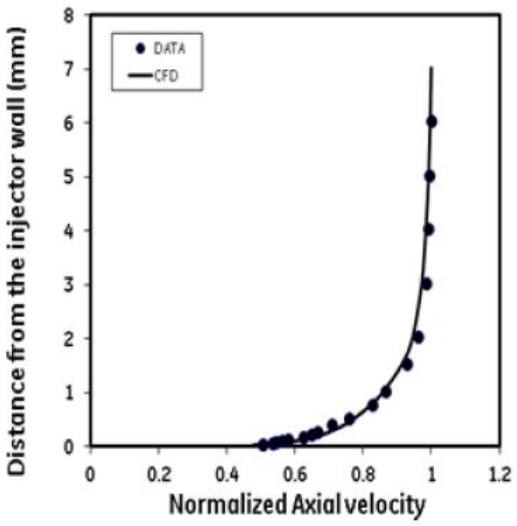


Figure 4.4: Simulation 2 velocity profile [54]

The third simulation modeled turbulent dispersion. In the first two runs, the discrete phase particles were only affected by the mean flow. It was expected that modeling the effect of turbulence velocity fluctuations on the particles would facilitate spreading and present a more physical result. The coordinate system used for the simulations is not the same as shown in fig. 4.1. The positive x axis is in the flow crossflow direction and the positive y axis is in the direction of liquid injection. Droplet diameter and velocity values were sampled at two planes downstream of the injection site. The first was at 30 diameters and the second at 60 diameters. These locations match those of the work of Sekar et al. [54].

## 4.3. Results

Figures 4.5 & 4.6 show the results of Simulation 1 at 30 and 60 diameterss downstream of the injection point.

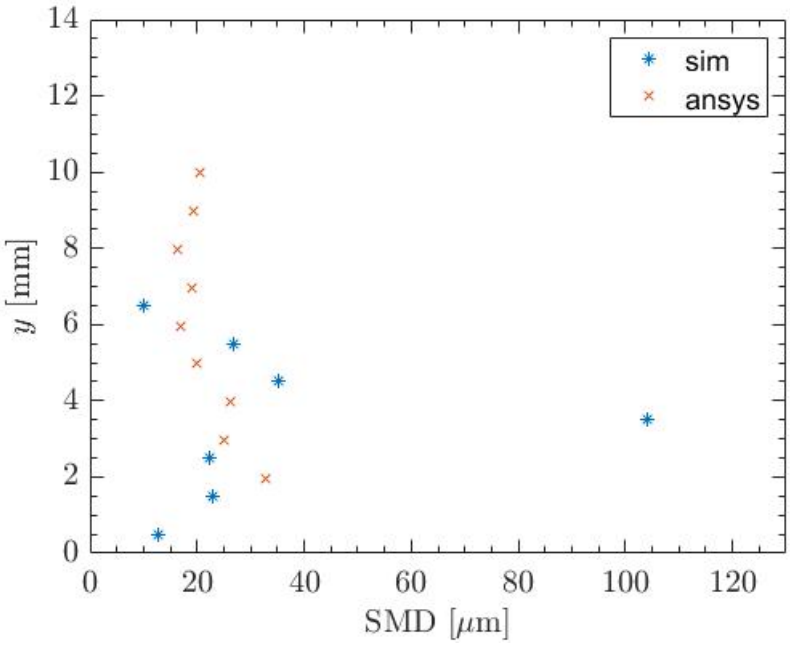


Figure 4.5: Simulation 1 vs Ansys results at 30D downstream

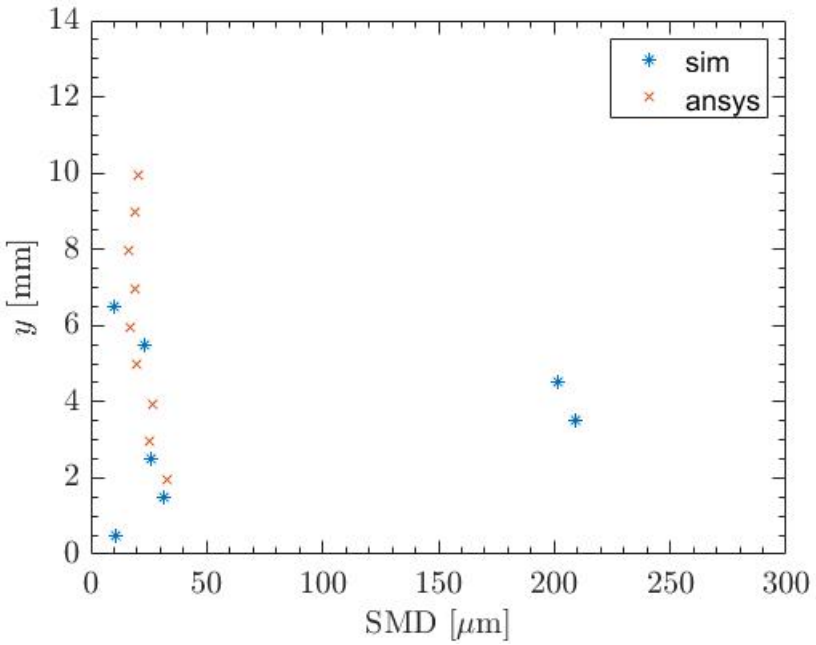


Figure 4.6: Simulation 1 vs Ansys results at 60D downstream

For reference, the results are compared to the results of Ansys as presented during a webinar introducing the new VOF-to-DPM solver [52]. Two major discrepancies are noticeable between the results and those of the software authors: one is the insufficient spreading of the jet, the other is high SMD values in a certain height range (as compared to the difference between the two datasets at other heights). Fig. 4.7 shows the results from the two downstream distances.

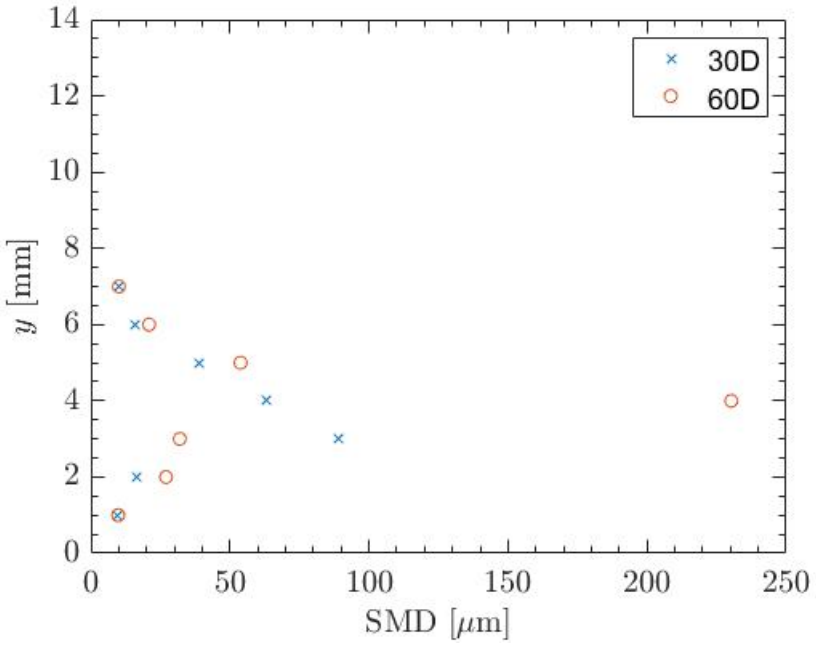


Figure 4.7: Simulation 1 @ 30D vs 60D

At first glance, one can see that the SMD values at certain heights are several times larger than the average value over the measured height. It is also noticeable that the values at

60 diameters downstream are not always smaller than the values at 30 diameters from the injection point. This should not be possible considering that coalescence is not modeled. From the physical standpoint it is also unlikely that a mean droplet value such as SMD would be higher at downstream vs upstream. This could occur locally over small distances due to coalescence of droplets, but not on average. This can be seen from the experimental measurements presented later in this section.

The second simulation implemented a velocity profile at the inlet that was uniform in the z direction. The results of Simulations 1 & 2 at the 30D location are compared in figure 4.8. The velocity profile implemented in the second simulation did affect the magnitudes of the SMD values, but the distribution pattern (with height) from the first simulation remained. The jet has also not spread any further in the y direction.

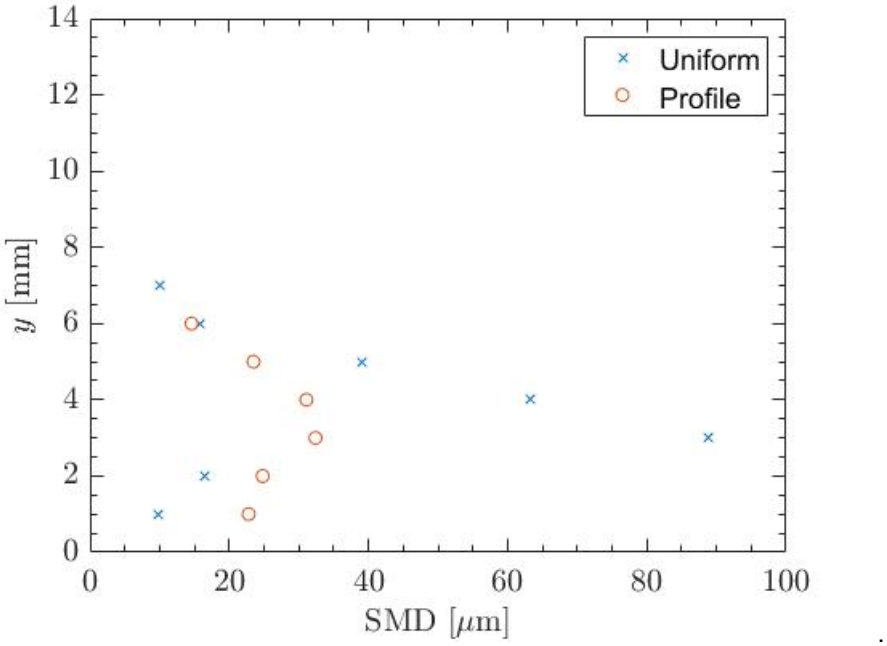


Figure 4.8: Simulation 1 (Uniform) vs Simulation 2 (Profile)

At this stage, it was expected that the simulation would produce particle diameters comparable to experiment, due to the implementation of the experimentally measured velocity profile. To demonstrate reliable results, a convergence study was necessary. Specifically, the aim was to show that the SMD distribution settles to a certain range after a certain sample size from which it does not deviate. The sample could then be considered converged within a given tolerance. A sampling time of 1 ms was used for all the datasets presented. This was chosen as a compromise between a reasonable calculation time (roughly 24 hrs) and an adequate sampling time for a case with a particle residence time of roughly .3 ms. In other words, a tracer particle injected at the x coordinate where the liquid is injected would exit the domain in .3 ms. This implies that the sample sizes are three times the dwell time of the particles in the domain. Since no data on sample sizes or sampling times was available from the works used for validation purposes, a sample size based on computing costs was considered a good starting point.

Fig. 4.9 shows the results of the convergence study of Simulation 2. Three datasets of 1ms length each are presented (labeled by absolute simulation time). Clear differences in the resulting patterns indicate that 1ms is not an adequate sample size. Given the significant time required for the convergence study (roughly one week), this was concerning from a timeline point of view. It was decided to continue with Simulation 3 despite the results being qualitative only, as the effect of the turbulent dispersion model would still be noticeable.

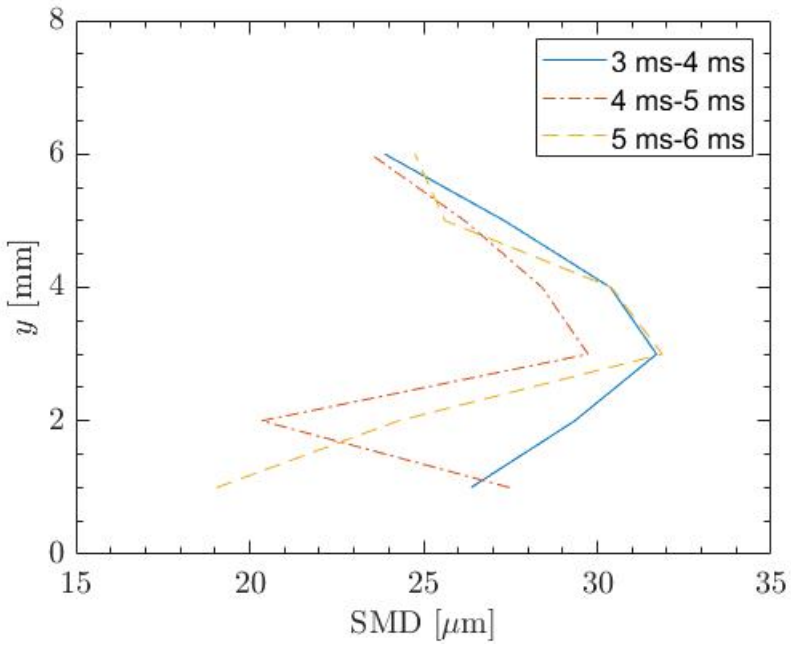


Figure 4.9: Simulation 1 (Uniform) vs Simulation 2 (Profile)

The results of the third simulation, seen in Fig. 4.10, show better spreading of the jet, reaching a height of 8mm vs the 6mm of the first two simulations . The SMD values are, on average significantly smaller than the previous two simulations. This can be attributed to an additional velocity (turbulent fluctuating velocity) component being taken into account in the breakup model. The problem of outlying SMD values reappeared in the results of Simulation 3 in Figs. 4.10 & 4.11. Specifically, the data point at the height of 4mm is significantly larger in magnitude than the rest of the distribution. It is unlikely that this result is physical.

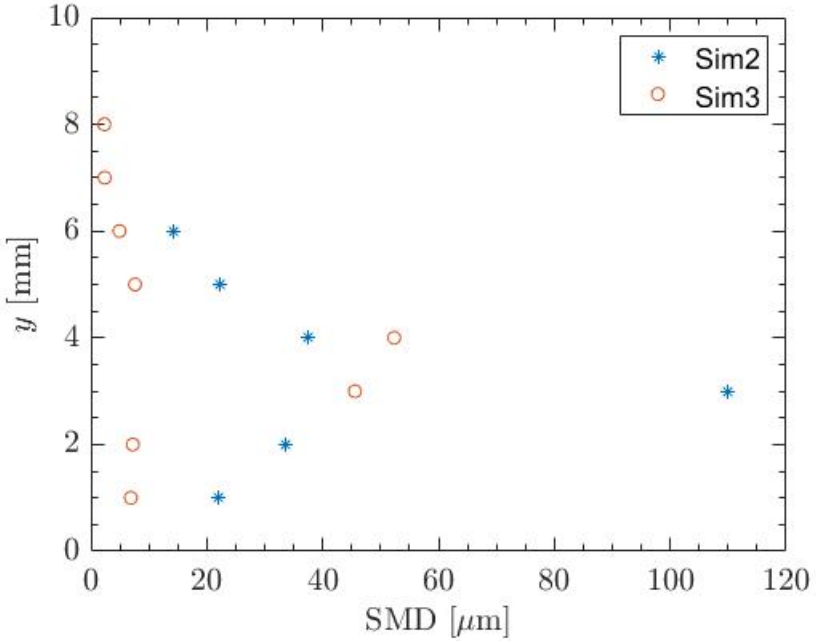


Figure 4.10: Simulation 2 vs Simulation 3 at X/D=30

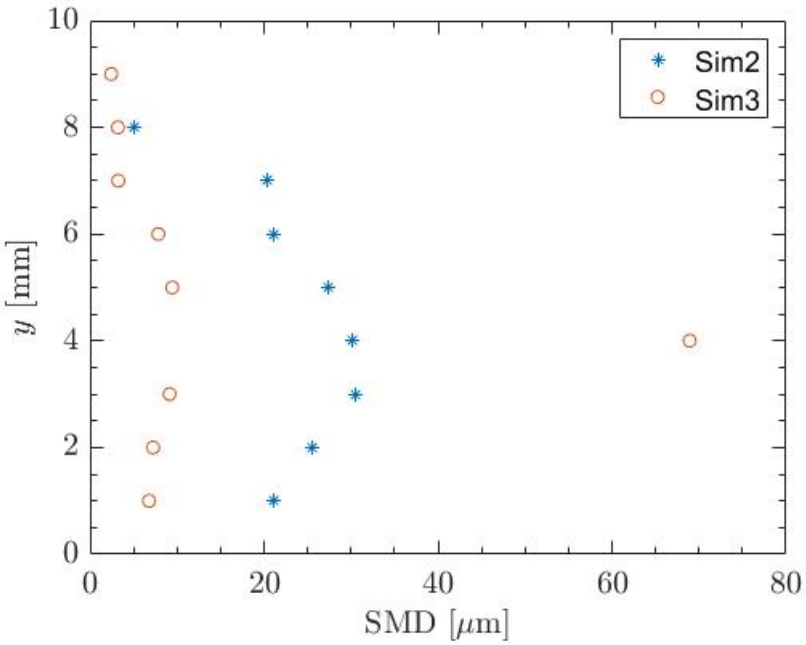


Figure 4.11: Simulation 2 vs Simulation 3 at X/D=60

The aphysicality of the simulation results are confirmed by the experimental results found in figures 4.12 & 4.13. It should be noted that the first datapoint (closest to the wall) was not shown by Ansys during the introductory webinar. A comment was made that their simulation presented discrepancies close to the wall possibly due to an improperly resolved boundary layer [52]. Before proceeding with further studies, it was decided to investigate the causes of unusually high SMD values at select heights for all simulation runs. This was a systematic error that could not be explained by lack of statistical convergence.

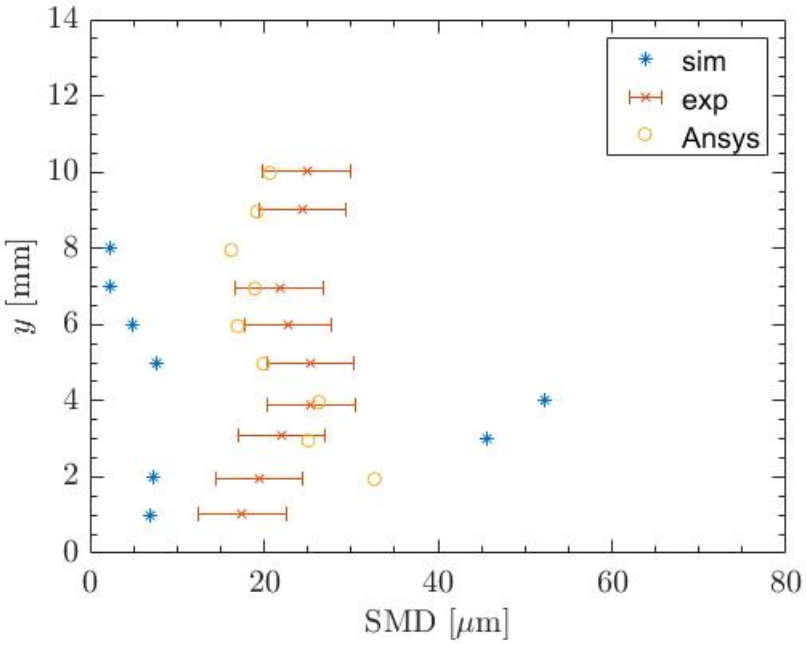


Figure 4.12: Simulation 3 results at X/D=30

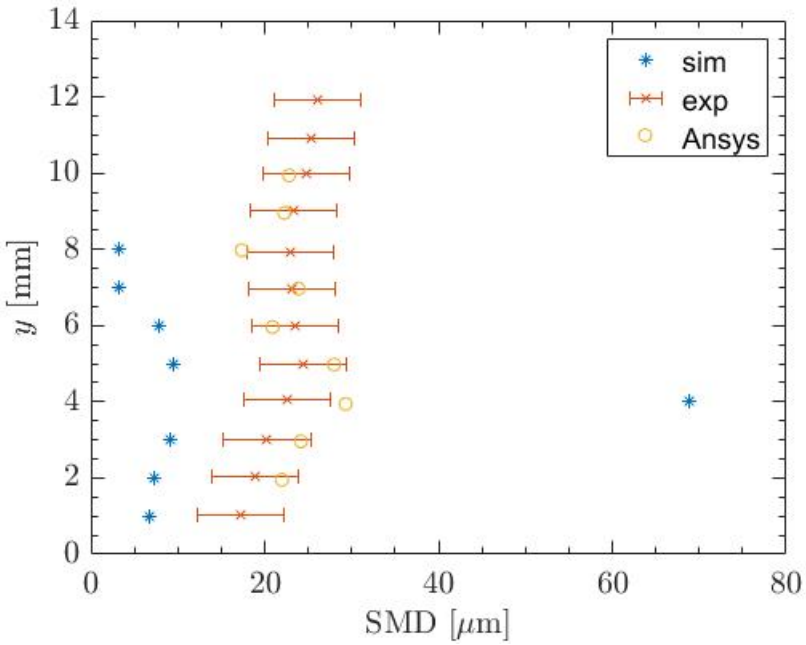


Figure 4.13: Simulation 3 results at X/D=60

Examining the droplet sizes obtained at the y values that produced high average SMD values, one can see that a small number of large droplets are responsible for skewing the height distribution. This can be seen by examining the droplet sizes at y=4mm from Fig. 4.10. These results are visible in Fig. 4.14. One hypothesis was that due to limits on the mesh size, the interface at the surface of certain ligaments could not be refined further and this resulted in unnaturally large ligaments meeting sphericity criteria and being converted to the discrete phase. In addition, it was observed that the wake created by the jet resulted in a significant variation of velocity magnitude with time.

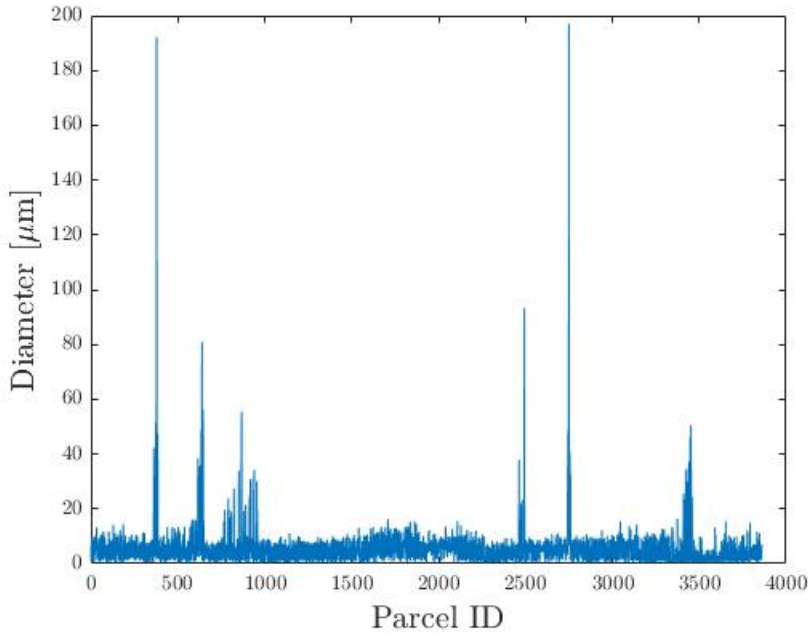


Figure 4.14: Simulation 3 droplet population at y=4mm at 60D downstream

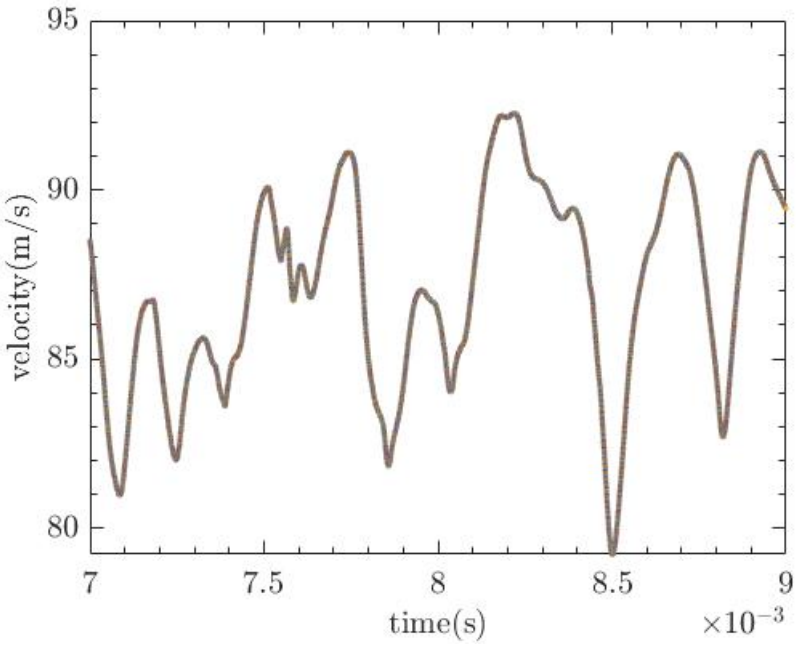


Figure 4.15: Velocity magnitude at X/D=30 and y=3mm

This can be seen in fig. 4.15 for simulation 3, 30 diameters downstream and at a height of 4mm. Sekar et al. indicated difficulty in resolving the wake created by the liquid column in simulations of the same experiment. A brief literature study revealed that LJICF cases can be characterized by a complex flow-field in the wake of the liquid column. Fig. 4.16 is a depiction of the three types of vortices typically formed in the wake of a liquid column injected into cross-flowing gas [12].

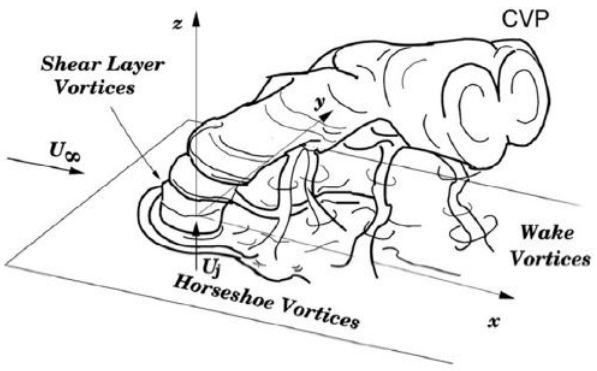


Figure 4.16: Conceptual depiction of LJICF wake

This fluctuation of the mean velocity field means that obtaining a converging (in time) distribution of SMD with height is a strong function of the sampling time. In other words, the sampling time needs to be much longer than the frequency of the velocity field fluctuation. In contrast, for a steady velocity field, the distribution would converge with an increasing number of droplets sampled. The sampling times of 1 ms to 3 ms performed during the different simulations have proven to be too short to obtain a converging droplet distribution. This means that even though certain sets of results may appear to be reasonably close to the experimental values, only qualitative information can be extracted from the results.

**Due to the limited experimental data available and the complexity of the flow-field in the wake of the jet, it was decided to simulate a case with a simpler flow-field. The**

**availability of quality measurement data and possibility of contact with the experimental team were also contributing factors to this decision.**

Some of the lessons learned from the early results were the following:

- It is possible that the solver produces a highly uneven distribution of droplet diameters
- Resolving unsteady regions in the flow-field can be instrumental to obtaining accurate results
- An accurate velocity profile for the gas phase is necessary to correctly resolve the atomization process

Some of the practical lessons learned relating to the use of the solver are summarized below:

- The velocity field tends to diverge at seemingly random points in space, likely due to the formulation of the turbulence model
- The dynamic adaption may stop if the adaption limits are not set properly
- The speed of the simulation is limited by the highest velocity found at any point in the domain. It is thus possible that non-physical high velocity regions in the flow-field limit the time-step size prohibitively.

The above conclusions/hypotheses reflect those of the author at the conclusion of the LJICF segment of this work. Subsequent chapters provide clarification on the solver behaviours encountered during the LJICF trials. The further learning that resulted from the primary research described in the next chapter could be used to improve the results of the work presented so far. The work presented in the current chapter is not complete and was included only to show early results and serve as a reference for the progress made throughout this thesis project.

# 5

# Experimental Setup

This chapter concerns the experimental setup of the air-blast atomizer simulations. The domain, mesh and numerical settings are presented and discussed. The final section provides an overview of expected results using examples from literature.

## 5.1. Sydney Piloted Needle Spray Burner - Problem description

The working principle behind the experimental setup is the use of air-blast atomization to stabilize a spray flame for industrial applications. A central needle injects acetone into a stream of coflowing gas. An additional coflowing gaseous stream surrounds the central pipe containing the needle, referred to as the pilot stream. The needle from which the liquid fuel is injected (acetone) can be moved axially closer to or away from the exit plane, thus allowing control over the fineness of the fuel that comes into contact with the pilot stream. A cross-section of the geometry can be seen in Fig. 5.1 [34].

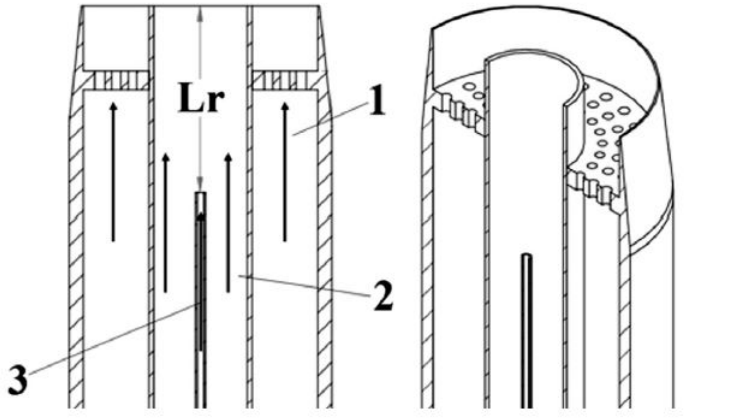


Figure 5.1: Geometry cross-section [34]

The pilot stream is labeled with the number 1. The needle injecting the liquid and the surrounding coflow are labeled 3 and 2 respectively. Fig. 5.2 shows the simulation domain (drawing not to scale) with dimensions provided in mm. The needle and coflow inlet were taken roughly 7 coflow diameters upstream from the needle exit plane. This was a compromise between a length sufficient to let the boundary layer fully develop but small enough not to require an excessive number of cells. The 25mm distance from the needle exit plane to the coflow exit plane is referred to as the recess length and matches the experimental setup.

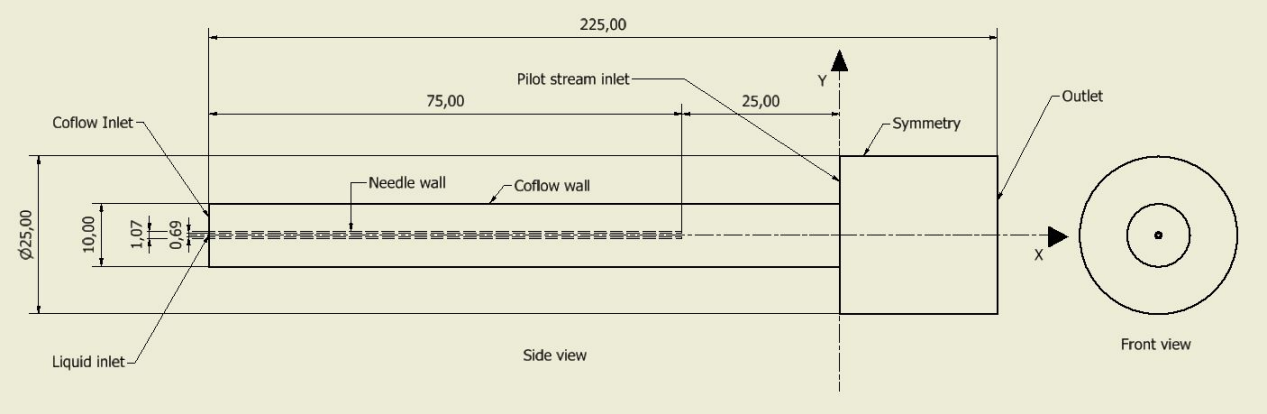


.

Figure 5.2: Needle burner domain

It is worth noting that the wall thickness of the coflowing stream was neglected for the purpose of the simulation. The thickness of the needle wall was taken into account. The inlet of the pilot flow was placed at the exit plane of the coflow. This was also a compromise in an effort to reduce cell count. Placing the inlet at this location does not allow the wall boundary layer to develop, so the most accurate setup would necessitate a velocity profile specification. Due to the low velocity of the pilot stream with respect to the coflow stream, it is reasonable to assume that the effect of the pilot inlet placement is not as significant as the other inlets. The distance from the pilot inlet to the exit plane was based on cell count and reverse flow balance. If the outlet is too close, reverse flow may be encountered, which can alter the simulation results. A value of 5 pilot stream diameters was found to be a reasonable initial value for this length.

A front view is provided as a reference, to show that the domain is cylindrical. The perforated plate in the pilot stream (see Fig. 5.1) is not visible since is is not included in the geometry (pilot inlet plane coincides with the coflow exit plane). The most important geometrical parameters are summarized in Table 5.1.

Table 5.1: Simulation Geometry

| Parameter Name | Value |
|---|---|
| Needle diameter ($D_n$) | $686e-06m$ |
| Coflow diameter ($D_c$) | $10e-03m$ |
| Pilot diameter ($D_p$) | $25e-03m$ |
| Needle wall thickness | $.5e-03m$ |
| Needle recess length | $25e-03m$ |

To summarize, in an effort to keep a reasonable cell count, the domain has a number of simplifications and shortcomings. These are the areas that will need refinement in a domain sensitivity study. The thickness of the wall between the coflow stream and the pilot stream was neglected (infinitely thin). The distance to the outlet from the pilot inlet could be increased up to 10-20 pilot diameters. The distance between the coflow inlet and the needle outlet could also be increased up to 30-40 diameters. These estimates are based on common values found throughout literature. The radius of the domain after the exit plane could also be a variable in a domain size sensitivity study. It is worth noting that the entire assembly was placed in a vertical wind tunnel when the measurements were taken. Extending the domain radially will mean modeling an additional coflow at a different speed which may or may not increase the complexity of the simulation significantly.

A summary of the operating conditions and material properties can be found in Table 5.2. All velocities are normal to their respective inlets. Material properties are provided by the

authors of the experiment. Relevant non-dimensional numbers such as the Reynolds and Weber numbers are also provided for reference.

Table 5.2: Simulation Parameters

| Parameter Name | Value |
|---|---|
| Liquid bulk velocity | $2.58m/s$ |
| Air bulk velocity | $48m/s$ |
| Liquid density | $786kg/m^3$ |
| Air density | $1.225kg/m^3$ |
| Liquid viscosity | $3.33e-04Pas$ |
| Coflow Reynolds nr | 28374 |
| Liquid Reynolds nr | 4180 |
| Chamber temperature | $293K$ |
| Absolute Pressure | $1bar$ |
| Surface tension | $.0237N/m$ |
| Weber number | 80 |
| Momentum ratio (M) | .53 |
| Mesh topology | Hexahedral |
| Mesh count (original) | $450kcells$ |

The values seen in Table 5.2 can be found in the document describing the experimental database of the Sydney Needle Burner [28]. The momentum ratio (M) is a commonly defined metric for atomization studies alongside the Weber and Reynolds numbers. It is important because it is a measure of the relative momentum between the two fluid streams.

$$M = \frac{\rho_g U_g^2}{\rho_l U_l^2} \tag{5.1}$$

The Weber number in Table 5.2 is defined by the experimenters as [28]:

$$We = \frac{\rho_g U_g^2 D_n}{\sigma} \tag{5.2}$$

## 5.2. Simulation setup

This section will cover the mesh, boundary conditions, numerical models and settings used for all simulations. The features of the mesh and the general meshing strategy are discussed in the first part, continuing with an explanation of boundary conditions used. After an overview of numerical models used and their settings, the section ends with a brief overview of expected results based on experiments.

### 5.2.1. Mesh overview

The mesh or grid is the discrete domain that calculations are performed over. The most important concern of the CFD user when it comes to creating the mesh should be discretization error. This is the error that results from representing governing equations as algebraic expressions over a discrete domain of space and time [41]. Temporal discretization error is a function of the time-step size used. Discretization error is a function of the quality of the grid. Quality metrics of relevance are: resolution, density, orthogonality, aspect ratio etc. In cases where the implemented equations do not depend on the grid size directly (RANS models), a mesh convergence study can be carried out in order to determine the resolution at which the solution becomes ”grid independent”. In these cases, the discretization error tends to zero as the grid size tends to zero [41]. In cases where equations for physical models depend on the grid size directly (LES turbulence models), a different approach must be taken to error quantification. Having discussed the significance of the mesh in a simulation, following paragraphs will present the features of the mesh used throughout this work.

The general meshing strategy was based on two goals: ensuring high resolution in the areas of primary atomization and keeping a structured mesh to reduce cell count. Fig. 5.3 shows a side view of the mesh. The gradual decrease in cell size in the axial direction can be seen from the coflow inlet plane towards the needle exit plane. The same is true for the resolution variation from the outlet to the pilot inlet. It is easy to see that the cell aspect ratios are very high at the inlets on the far left and the outlet on the far right of Fig. 5.3. These are areas that can use refinement.

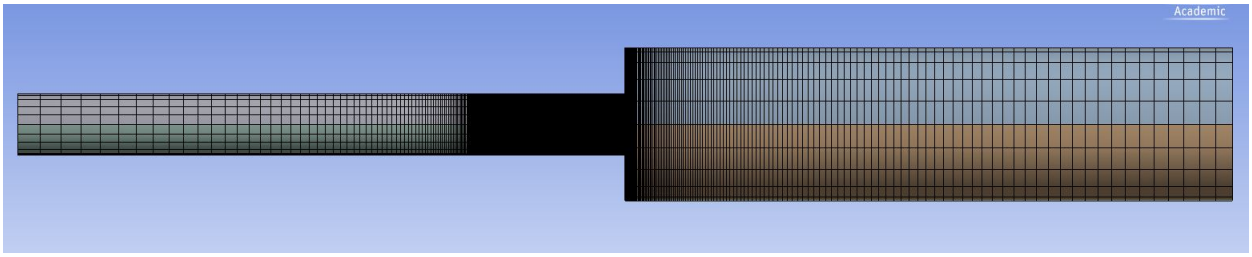


Figure 5.3: Mesh side view

A front view of the mesh seen in Fig. 5.4 will show that the mesh is finest at its center and the cell sizes gradually increase radially outwards. Again, the rationale was to have the highest resolution in the region where primary atomization occurs. The quickly increasing aspect ratio of the cells in the radial direction is easily visible here. Refinements in the radial direction are the most expensive from a total cell count point of view, since the mesh has the same cross section (cell shape and layout) at every axial point.

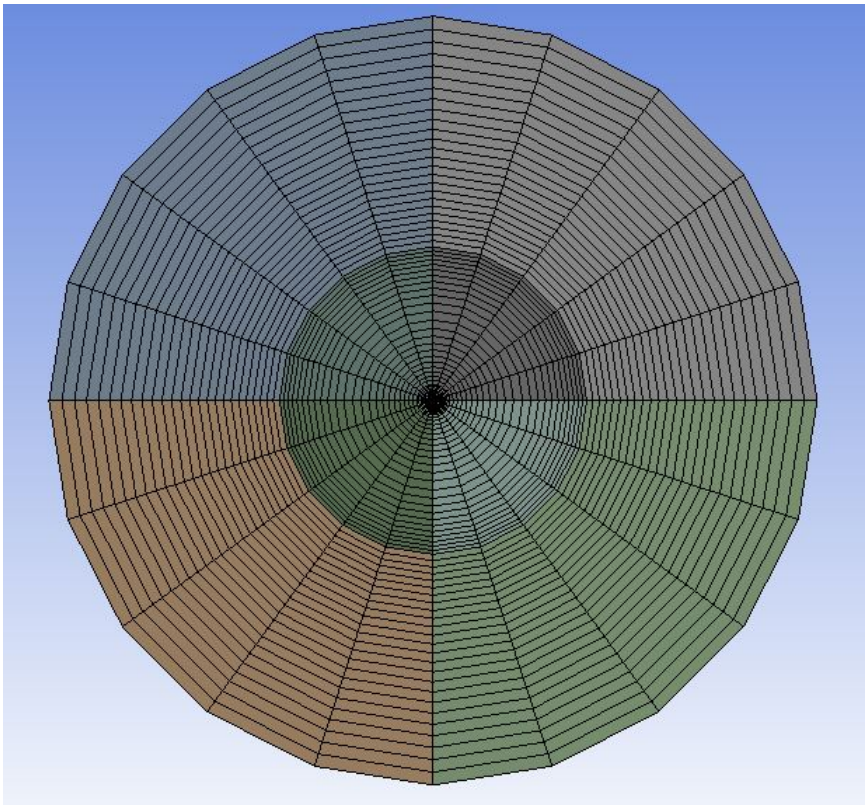

Figure 5.4: Mesh front view

Fig. 5.5 shows the upper-half of the mid-plane of the domain in the region after the needle exit plane and before the pilot inlet plane. The dense region towards the bottom is

the centerline of the domain. The cell aspect ratio is highest in the middle (looking in the y direction), this was done to manage the cell count while maintaining adequately small cells near the wall to ensure a correct shear stress prediction. (Note: The difference in contrast between some of the vertical lines is an unintended software glitch and bears no significance).

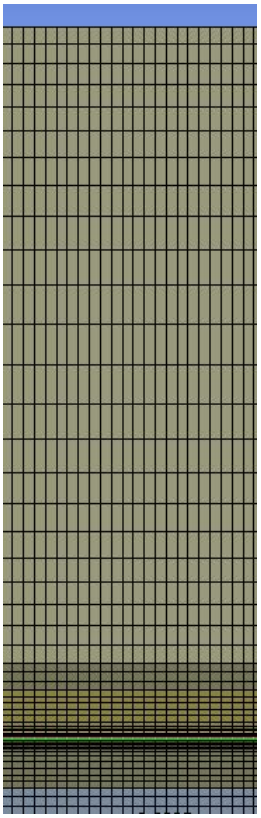

Figure 5.5: Mesh mid plane view

The total cell count of the domain was 4.5e04 hexahedral cells. This is a conservative amount by any measure (as most LES simulations in literature are in the range of 2-3 million cells). It is important to note however, that the cell count can increase significantly depending on the mesh adaption settings. In addition, the simulation makes use of a hybrid RANS-LES turbulence model which makes the resolution requirements lower than those for traditional LES. The final cell count after adaption remained roughly at the 5.1e04 value.

It should be possible to estimate the sizes of the droplets that the mesh will be able to resolve using geometrical reasoning. Because the diameters of the discrete parcels are determined by the ligaments that the VOF model is able to resolve, a relationship can be established between the resolution of the mesh and the smallest resolved parcels. The structure of the mesh is such that the length of the cells in the x direction, from the exit plane of the needle to the exit plane of the burner, is constant. Cell edges in the y direction are not constant. In the circumferential direction, cell sizes are constant. Knowing that cell edge lengths must be smaller than the size of the particle in order to capture its geometry, it can be said that the largest edge length will determine the smallest particle that can be captured. Fig. 5.6 shows a closeup of the mesh around the needle exit plane:

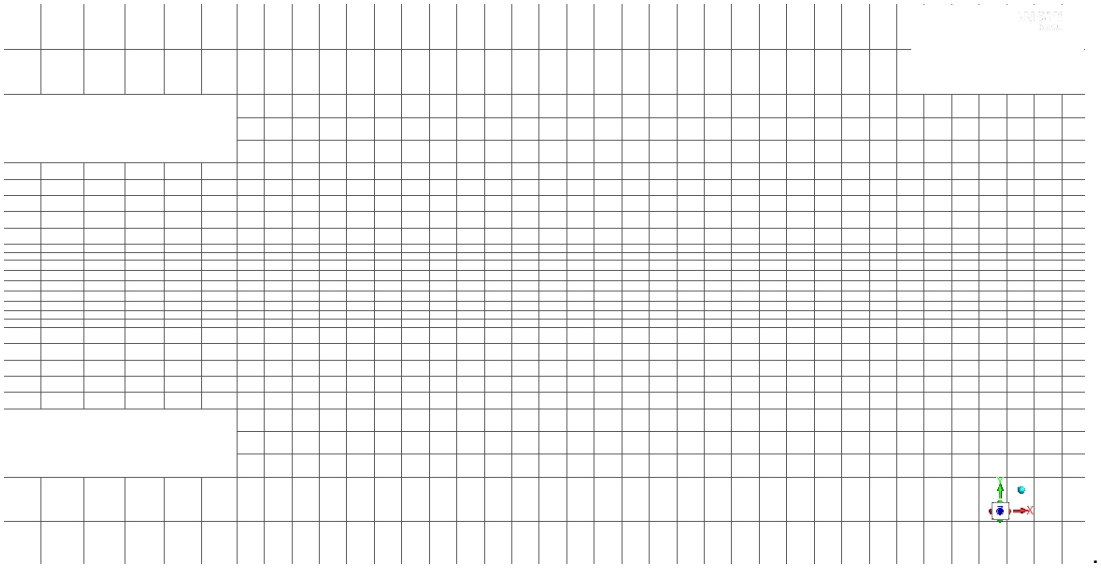

Figure 5.6: Needle exit plane side view

Knowing the diameter of the needle (686 $\mu m$), estimates can be derived for the edge lengths of the cells. Fig. 5.4 also clearly shows that there are 20 divisions in the circumferential direction in total. Using the radius of the needle, an estimate can be obtained for the circumferential edge lengths at the walls of the needle. Using hanging node refinement and a maximum refinement level of 2, estimates can be obtained for the smallest refined edge lengths. If it is further assumed that a minimum of two edges are required in each direction to capture a spherical ligament, an estimate for the smallest resolvable diameter can be obtained. This data is shown in Table 5.3. One can conclude based on the presented estimates, that in the best case scenario, the smallest droplet diameter that can be resolved in the primary atomization zone is in the region of 86 $\mu m$.

Table 5.3: Mesh resolution

| Direction | X | Y | Circumferential |
|---|---|---|---|
| Base mesh | 45 $\mu m$ | 90 $\mu m$ | 172 $\mu m$ |
| Refined 2x | 11.25 $\mu m$ | 22.5 $\mu m$ | 43 $\mu m$ |
| Smallest resolvable diameter | 22.5 $\mu m$ | 45 $\mu m$ | 86 $\mu m$ |

### 5.2.2. Boundary conditions

The boundary conditions used are listed in Table 5.4. Inlets require either a pressure or velocity specification which is usually dictated by what data is available from experiment. In this case it is bulk velocity for all three inlets. The walls all use a ”No Slip” boundary condition which sets the velocity at the wall to zero with the aim of including wall shear stress effects on the velocity field. Static pressure is specified at the outlet boundary which is standard procedure for incompressible simulations and works well if the simulation domain is large enough to allow the flow to reach a fully developed state. No changes in flow properties should be observed in the flow direction at this point. The boundary condition sets all gradients to zero at the outlet. The edges of the domain beyond the exit plane of the coflow use a symmetry boundary condition which is the same as a ”Slip Wall”. This option was chosen because it is the closest alternative to the experimental setup. Both normal velocities and normal gradients are set to zero at the boundary surface. In reality there is likely some flow across this boundary due to the difference in velocity between the pilot stream and the wind tunnel speed. Given that a more accurate representation would’ve required a significantly larger domain, this solution was deemed an acceptable compromise. This boundary is also

reasonably far from the centerline, where measurements were taken and so it is possible that the effects of not resolving the mixing layer between the wind tunnel and the pilot stream are insignificant on drop sizes and velocities (especially at the coflow exit plane).

Table 5.4: Boundary conditions

| Boundary name | Boundary condition | Values |
|---|---|---|
| Liquid Inlet | Velocity Inlet | 2.58 m/s axial |
| Coflow Inlet | No Slip Wall | 48 m/s axial |
| Outlet | Pressure Outlet | 0 gauge |
| Needle Wall | No Slip Wall | N/A |
| Coflow Wall | No Slip Wall | N/A |
| Symmetry | Symmetry | N/A |
| Pilot stream inlet | Velocity Inlet | 1.5 m/s axial |

### 5.2.3. Inputs and settings

The default simulation settings used in all runs are detailed in table 5.5 below. These settings are shared by all simulation runs unless specified otherwise.The above settings are provided for reproducibility and as a general guideline for future work. These were selected based on the recommendations of the Ansys manual and introduction webinar of the new solver [51][52].

Table 5.5: Needle burner - simulation settings

| Setting | Value |
|---|---|
| Transient/Steady State | Transient |
| Gravity | -9.81 $m/s^2$ in X dir. |
| Pressure/Velocity Coupling | Coupled |
| Gradient discretization | Least Squares |
| Pressure discretization | Body Force Weighted |
| Volume fraction discretization | Geo-Reconstruct |
| Momentum discretization | Bounded Central Differencing |
| Turbulent quantity discretization | First order upwind |
| Gradient adaption settings | Curvature Method; Normalized; 2 Refinement Levels |
| Adaption algorithm | Hanging Node |
| Breakup model | WAVE w/ constants $B_0$=.61 , $B_1$=1.73 |
| Turbulent Dispersion Settings | DRW model w/ random eddy lifetime and $C_l$=.15 |
| Turbulence model | k-$\omega$ SST SBES with WALE SGS model |
| Overfill factor | 2 |
| Asphericity criteria | 0.5 for both |
| Maximum ligament diameter considered for conversion | 120e-06 m |

The details of the discretization schemes and the pressure-velocity coupling algorithms can be found in the Ansys Theory Guide [1]. These are well-known and documented and will not be discussed for the sake of brevity. The remaining settings have been discussed in chapter 3.

The author would like to point out a significant difference in one setting versus the Ansys example case [52]. When setting the limits for gradient adaption, the normalization of the adaption function values can impact results significantly. The default settings (also used in the example by Ansys) do not use normalized limits for the adaption function. In other words, the limits on the adaption function are absolute values and it is difficult to set them properly. This can result in inadequate refinement during the simulation due to the difficulty

in estimating reasonable absolute limits. The solution to this is to normalize the adaption function values using the largest value in the domain. This will keep the limits for refinement and coarsening between 0 and 1, making it easier to set these values appropriately. The reader is referred to sec. 3.4.6 for details on gradient adaption.

## 5.3. Expected results

This section briefly discusses what one would expect from the experimental setup described in preceding sections. The goal is to give the reader a general overview of what the flow-field looks like in similar simulations. Some of the presented experimental figures will be used as a basis for comparison with simulation results in Chapter 8. A conceptual depiction of the flow field in front of a coaxial atomizer can be seen in Fig. 5.7:

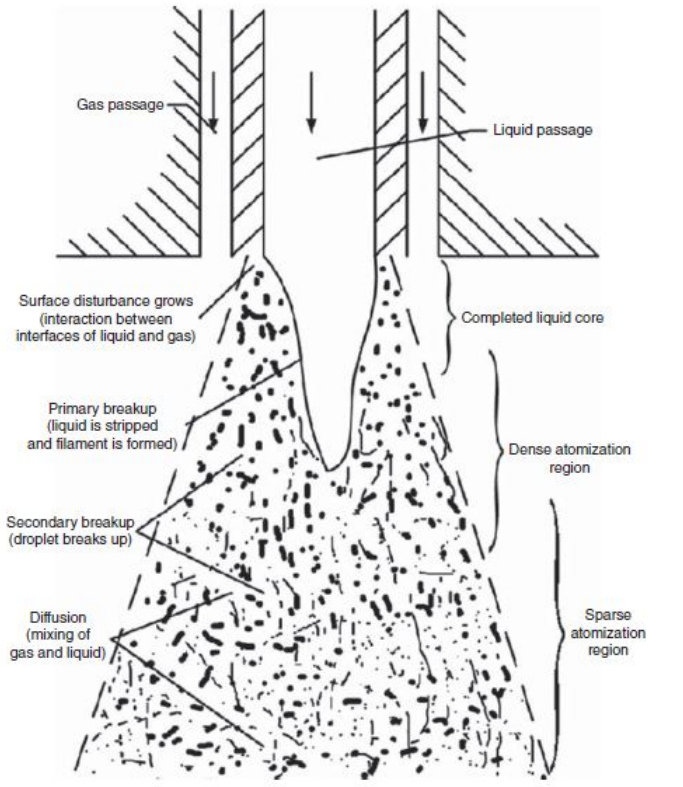


Figure 5.7: Coaxial shear injector flow field [65]

Three distinct regions are distinguished: the liquid core, the dense atomization region and the sparse atomization region. The last two are also referred to as the primary and secondary atomization regions. The dense or primary atomization region is seen in front of the liquid core. This is the region where ligaments begin to break off from the liquid core as a result of internal turbulence of the jet and the formation of unstable surface waves. The sparse or secondary atomization region follows, where small ligaments or droplets break up further into even smaller structures. Snapshots of round liquid jet in coflow experiments can be seen in Fig. 5.8. The velocity of the coflowing gas increases from left to right. It is worth noting how the liquid core breakup location shifts and the shapes of the ligaments change with increasing gas velocity.

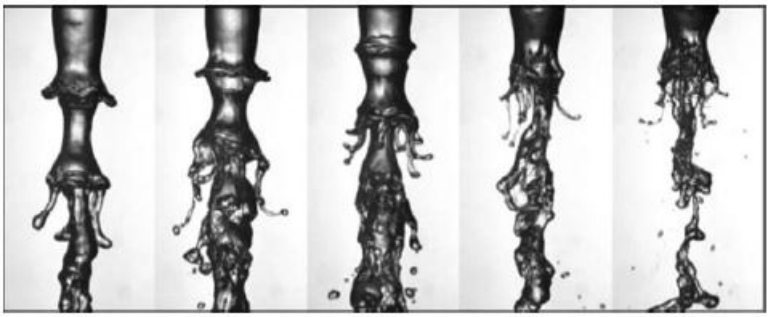

Figure 5.8: Round liquid jets in different velocity coflows [64]

For a better comparison and an overall view of the liquid core, the work of Charalampous et al. will be used as a reference [22]. The work explores the properties of round liquid jets in a coflow of air at different flow conditions. The selected figure was chosen based on the proximity of the Weber and Reynolds numbers to the case studied in this work. Fig. 5.9 shows a snapshot of the jet:

Figure 5.9: Round liquid jet in gaseous coflow [22]

For reference, Tab. 5.6 shows the Weber/Reynolds numbers and the momentum ratio for the studied case and that of Fig. 5.9.

Table 5.6: Simulation Parameters

| Parameter name | Charalampous et al. | Current study |
|---|---|---|
| Weber number | 80 | 80 |
| Liquid Reynolds number | 5440 | 4180 |
| Momentum ratio (M) | .66 | .53 |

A matching Weber number makes the experimental snapshot a good reference for a comparison of the development of surface instabilities. A higher Reynolds number than the simulated case may mean an earlier breakup of the liquid core in the case of Fig. 5.9 as opposed to the simulated case. This has to do with the internal turbulence intensity of the liquid jet.

# 6

# Simulation results

The focus of this chapter is presenting the obtained results. These are presented with the original research questions in mind. The structure of the chapter follows that of the research questions asked in Chapter 1. Section 6.1 discusses droplet diameters, velocities and section 6.2 presents results on what models and parameters were most accurate.

## 6.1. Droplet Size and Velocity Results

Measurements of parcel properties were carried out by defining a sampling plane at an axial distance from the burner exit plane that matches the location of experimental measurement. The properties of any discrete parcels that pass through the sampling plane are recorded. In this case, sampling was done over a plane parallel to the exit plane at a distance of $X/D_c$=0.3 in the positive x direction from the burner exit plane. The coordinate system is zeroed on the center line of the burner at the exit plane. This is visible in Fig. 5.2 in Chapter 5. Because primary and secondary atomization are modeled in the simulation, there is a relationship between parcel sizes and velocities. Both are also primarily functions of the continuum phase velocity magnitude.

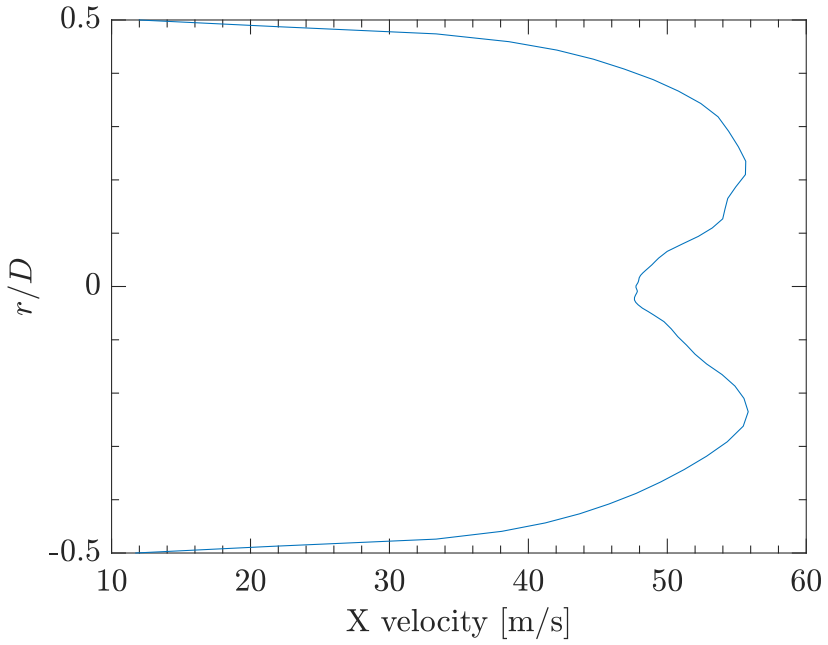


Figure 6.1: Axial velocity magnitude at exit plane

For this reason, it is wise to examine the velocity field inside the burner. Figure 6.1 shows the mean axial velocity magnitude radially across the exit plane. The profile is almost perfectly symmetrical about the centerline. The reason for the slight asymmetry is likely due to liquid ligaments passing through at slower velocities than that of the gas. Near the centerline there is a decrease in velocity. This can be explained by the presence of slower moving liquid ligaments in the core and their wakes. The two peaks are roughly halfway between the centerline and the wall, which intuitively makes sense because on either side there must be slower moving liquid (wall on the outside and low velocity liquid in the core). Examining the near-wall region, the shape of the velocity profile resembles the typical turbulent velocity boundary layer and reaches zero at the wall (per the no-slip boundary condition).

Because the break-up model is based on the relative velocity between liquid and gas, one would expect an inverse pattern of diameter vs height to the pattern seen in Fig. 6.1. Physically, this also makes sense since higher Weber numbers (or higher inertial to viscous force ratios) will act to destabilize ligaments and initiate breakup. Fig. 6.2 portrays SMD values across the coflow radius. Each data point is plotted at the center of the radial interval over which the discrete parcels were recorded. For example, the SMD value of 133 at r/D=.55, represents the Sauter Mean Diameter of all the particles recorded over the interval r/D=[.5,.6]. SMD values are highest at the center line and decrease in the peak velocity area. Values then increase with the radial coordinate and decrease towards the end of the measurement area. The decrease seen above the r/D=.5 height could be the result of an increase in turbulence intensity due to the mixing layer formed by the interaction of the pilot stream with the coflowing stream.

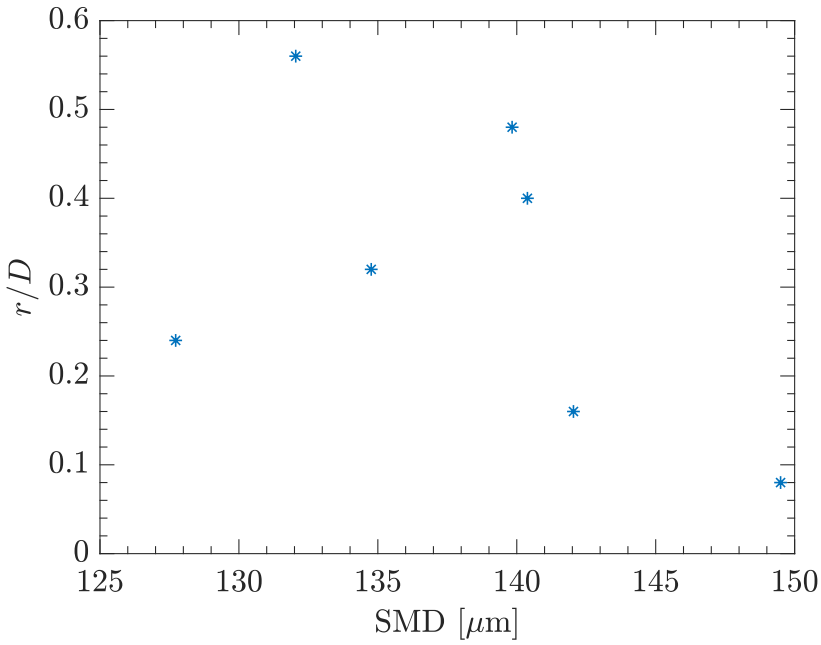


Figure 6.2: Droplet SMD at X/D=.3

Regarding the velocity of the droplets, it is a function of drag. Considering the physics of the studied problem, the expected trend is that the droplets will accelerate in the axial direction and eventually reach the bulk velocity of the flow. This process is complicated by breakup, because smaller droplets will react differently to a disturbance than larger droplets. If one examines the mean flow velocity vs the mean droplet velocity in the radial direction, the pattern should be similar even if the particles have not yet reached the flow bulk velocity. Fig. 6.3 shows the mean particle velocity magnitudes in the radial direction. Intuitively the pattern looks reasonable since velocities decrease radially outward with a slight increase at the last point, which may be a result of the pilot stream momentum.

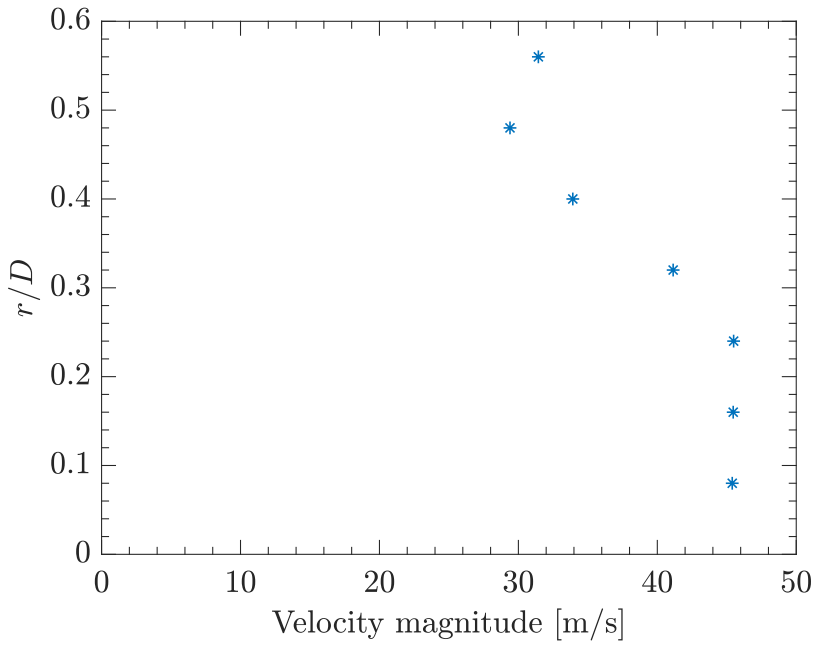


Figure 6.3: Mean droplet velocity magnitude at X/D=.3

A comparison with the flow velocity at the same locations, seen in Fig. 6.4, shows some discrepancies. At the top of the curve, there is a noticeable difference in the magnitude of the flow vs the magnitude of droplet velocity. This is likely caused by the fact that the pilot stream velocity is about 2.5 m/s, which is the velocity seen above r/D=.5. The droplets in this region have likely retained most of their energy picked up from the coflow of the burner. This would explain the significantly higher droplet velocity (compared to the flow mean velocity) at heights above r/D=.3.

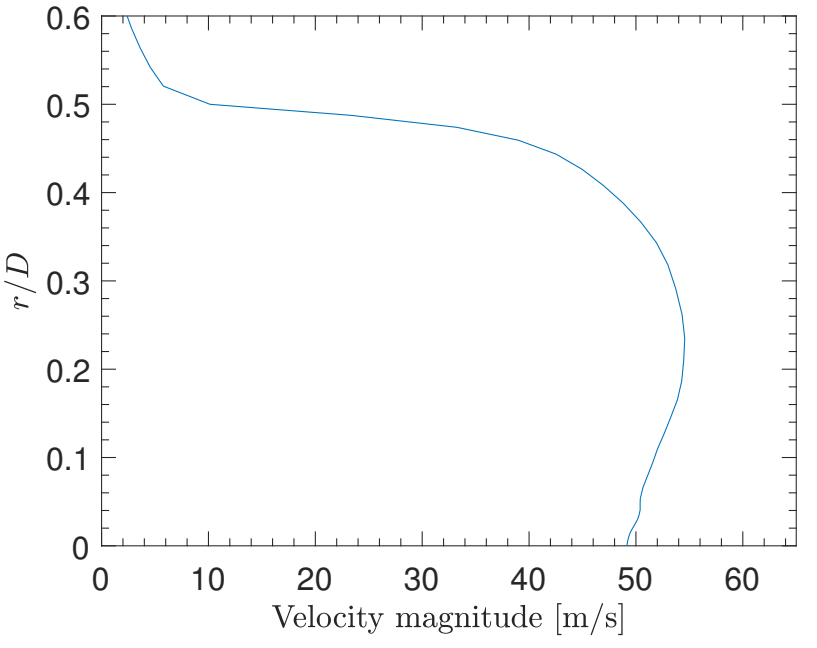


Figure 6.4: Mean flow velocity magnitude at X/D=.3

## 6.2. Sensitivity studies

A comparison of results obtained using different settings or physical models can shed light on the reliability of the results as well as the adequacy of the implemented models to the problem being solved. This section will attempt to provide answers to research questions 1.2 & 2.2. Table 6.1 summarizes the different simulations conducted and the changes made as compared to the control simulation:

Table 6.1: Simulations Summary

| Simulation nr. | Parameter varied | Values |
|---|---|---|
| 1 | Control | N/A |
| 2 | Overfill factor | From 2 to 1 |
| 3 | Breakup model | From WAVE to TAB |
| 4 | Discretization order | 1st to 2nd |

### 6.2.1. Over-Fill Factor

The Over-Fill Factor was chosen as a parameter for a sensitivity study because it is fundamental to the transition mechanism of the VOF-to-DPM solver. As explained in Ch. 5, the OVF governs the number of parcels that are formed from a liquid ligament. Because mass conservation is enforced, it subsequently also governs the diameters of the parcels that are formed. Fig. 6.5 shows SMD results at an OVF value of 2 compared with an OVF value of 1.

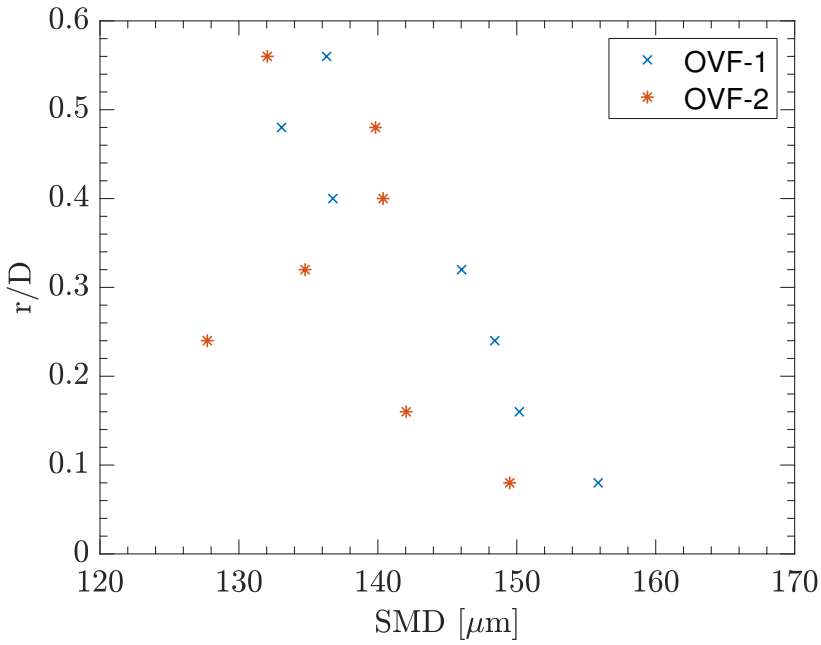


Figure 6.5: SMD distribution at X/D=.3

If one were to assume that the effects of secondary breakup are negligible compared to primary breakup at the measured location, then reason dictates that the SMD values for OVF-1 must be smaller overall. This is not the case however. SMD values for OVF-1 are only smaller at 2 out of the 7 locations in question. The first possible explanation is that even if larger parcels are formed initially, secondary breakup will result in a net decrease in parcel sizes by the time the sampling plane is reached. The second, less likely explanation is a non-converged sample in either or both cases. Convergence studies and criteria are discussed in Ch. 8.

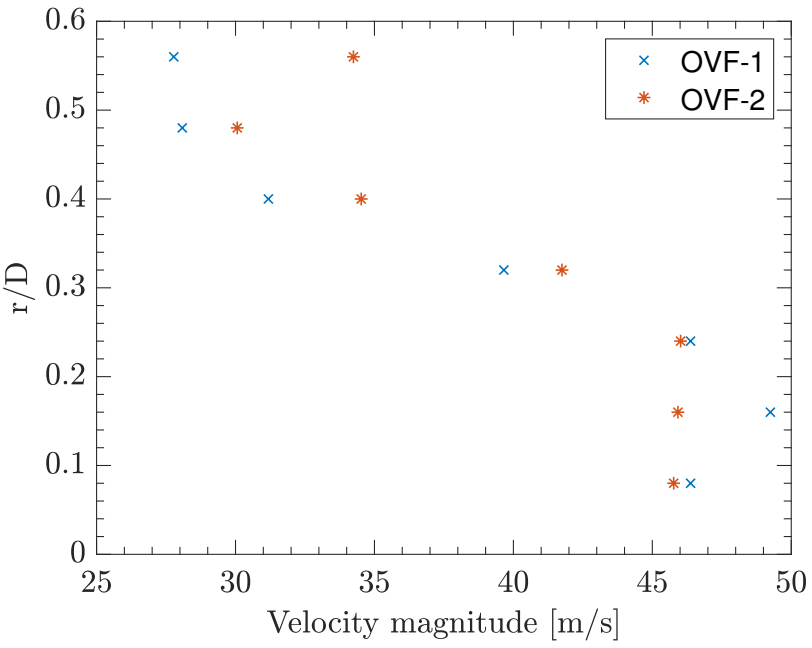


Figure 6.6: Parcel axial velocity magnitude distribution at X/D=.3

Fig. 6.6 shows the axial velocities of OVF-1 and OVF-2 data sets seen in Fig. 6.5. Larger particles should take longer to react to the velocity of the flow and therefore the expectation is that the velocities of OVF-1 be smaller than those of OVF-2 for locations where the SMD is smaller. Again, this does not apply for all locations. Therefore, there are discrepancies between the obtained results and the expected outcome. These findings may provide a basis for future work. Specifically, an investigation of results using different OVF values without a secondary breakup model might provide further insight.

### 6.2.2. Breakup models

The breakup model of the discrete phase is essential in correctly predicting secondary atomization. It was therefore decided to include a sensitivity study focusing on two classical breakup models (WAVE and TAB). The Fluent Theory Guide claims that the WAVE model is applicable for Weber numbers above 100 and the TAB model is effective for ”low Weber number” sprays. Based on this information only, a sensitivity study using these two models could shed light on the limits of the influence of secondary breakup modeling on droplet sizes. The reader is reminded that the Weber number of the studied case is 80.

Figs. 6.7 and 6.8 show SMD and axial velocity magnitude results at the plane of interest (X/D=.3). It is clear that the TAB model has produced smaller SMD values at all radial height intervals. Reason then dictates that velocity values would be the same as the WAVE model velocities or higher, due to smaller droplets reacting to the flow in a shorter time. This is only true if breakup has occurred far upstream of the location of measurement however. The velocity results indicate lower velocity values for the TAB model at almost all heights. Another significant difference is the shape of the velocity curve, which shows a decrease between the last two data points for the TAB model. This difference will be significant for validation purposes.

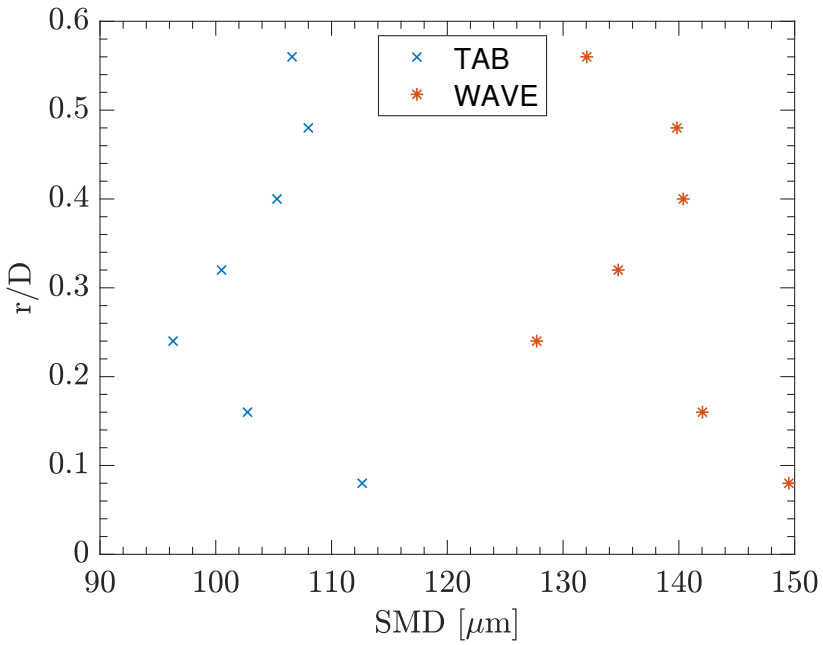


Figure 6.7: SMD distribution at X/D=.3

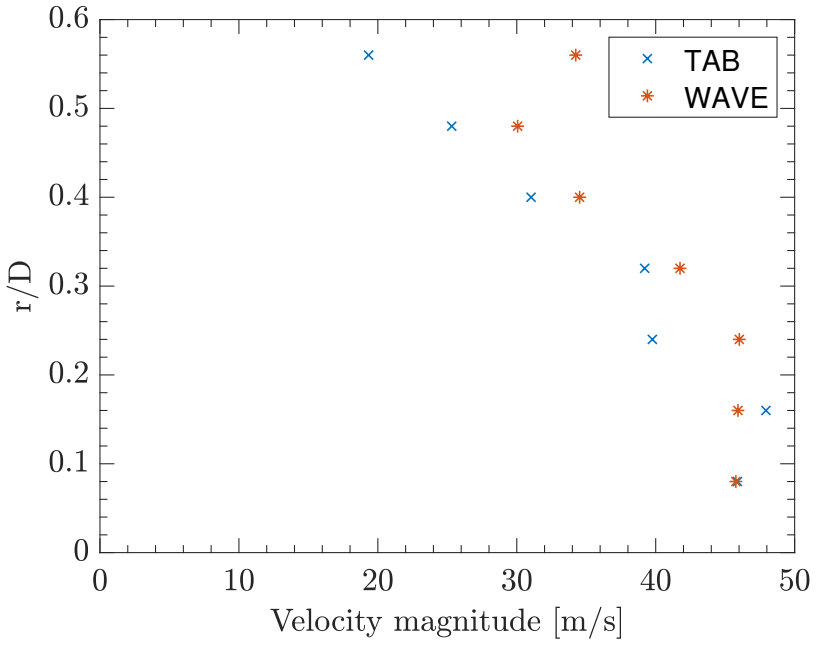


Figure 6.8: Parcel axial velocity magnitude distribution at X/D=.3

Having examined the results, the fundamental question becomes: why does the TAB model predict smaller droplet sizes than the WAVE model. Some possible answers can be found in the original work on the TAB model by O'Rourke et al. [43]. It is stated that one of the advantages of the TAB model over the WAVE model is the inclusion of the effect of liquid viscosity. Another mentioned advantage over the WAVE model is the ability of the TAB model to predict that breakup does not necessarily occur at a well defined critical Weber number. Since the Weber number for the problem in question is below the recommended range for the WAVE model (above 100), it is to be expected that the results will not be optimal. The diffi-

culty lies with the the intermediate Weber number range of the problem, which is likely not the ideal range for the TAB model either (it is too high). Future studies could be conducted on the appropriateness of other breakup models for the studied experiments.

### 6.2.3. Discretization order

Discretization order refers to how many terms are left out during the representation of a differential equation as a finite, algebraic expression. The lower the discretization order, the higher the truncation error that results. For the same reason, if the mesh is refined, the factor by which truncation error is reduced is dependent on the discretization order. It is common practice to start simulations with first-order discretization settings in order to avoid instability in the early phase of the simulation. Once a solution has been reached with these methods, higher order schemes can be used to obtain more accurate results. In this case, three discretization schemes were changed from their settings in Simulation 1: pressure, turbulent kinetic energy and specific dissipation rate. Table 6.2 shows an overview of the changes in the discretization settings.

Table 6.2: Settings variation

| Term | Sim 1 value | Sim 4 value |
|---|---|---|
| Pressure | Body Force Weighted | PRESTO! |
| Turbulent Kinetic Energy | First Order Upwind | Second Order Upwind |
| Specific Dissipation Rate | First Order Upwind | Second Order Upwind |

The PRESTO! interpolation scheme should yield more accurate results than the Body Force Weighted scheme according to Ansys [52]. The reasons for this likely have to do with the methods used to calculate pressure values at cell faces. The details are purely a topic of numerical methods and are beyond the scope of this work. The aim of this study is merely to get a sens of the degree to which the simulation results are influenced by these settings. Figs. 6.9 & 6.10 show a comparison of second order and first order SMD and parcel axial velocity values.

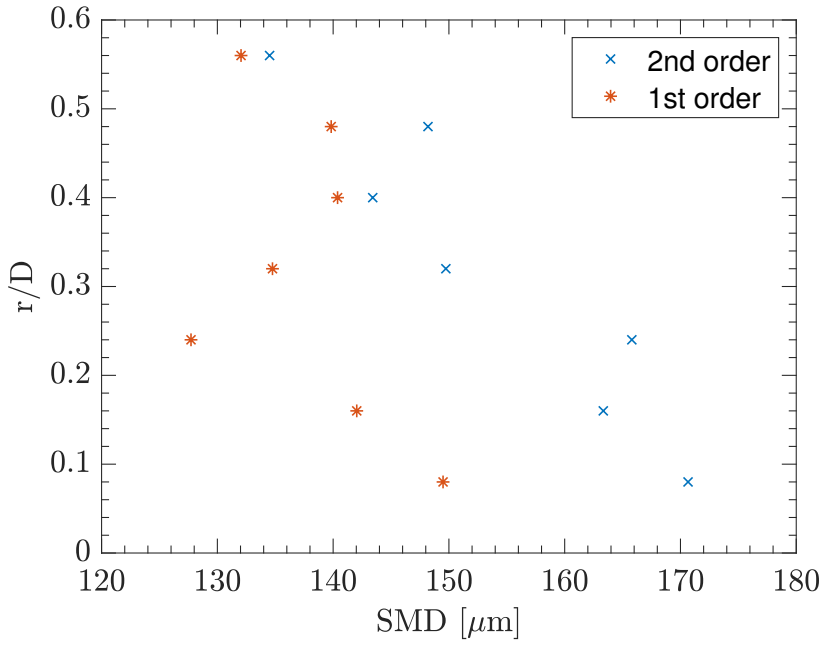


Figure 6.9: Parcel SMD distribution at X/D=.3

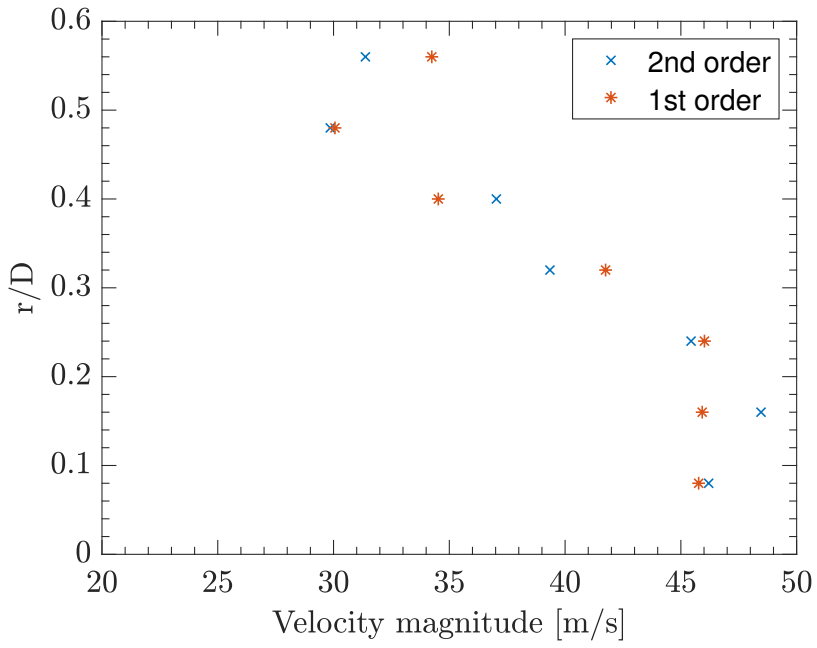


Figure 6.10: Parcel axial velocity magnitude distribution at X/D=.3

The SMD values are consistently higher for the 2nd order data set, whereas the velocity values do not differ significantly. The likely cause of this is lower relative velocities between the flow and the discrete parcels. This is true if one assumes that statistical convergence has been achieved. The velocity profiles at the burner exit plane and the SMD distributions both indicate that convergence has occurred. Reason then dictates that the velocity field predicted by the second order simulation may differ significantly from the first order simulation, resulting in a different range of parcel sizes.

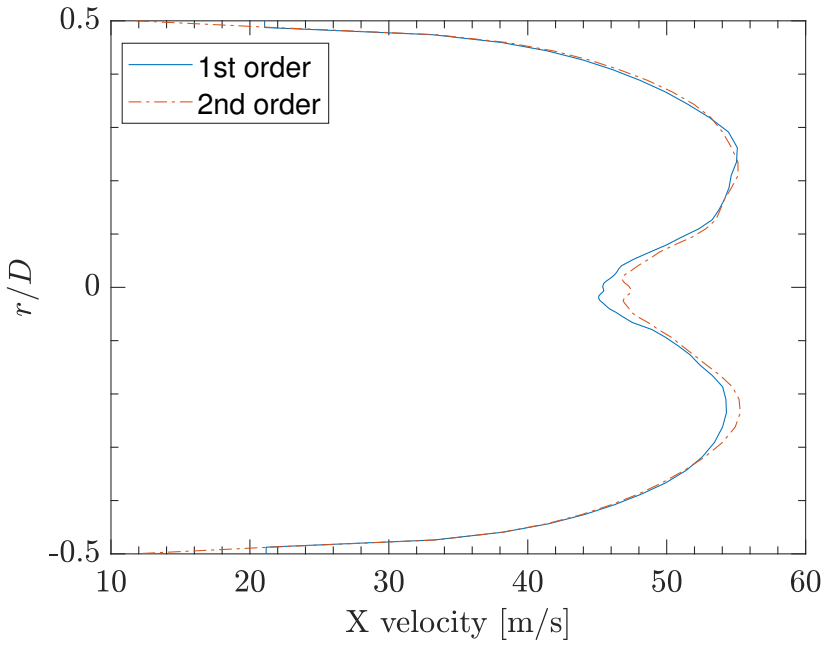


Figure 6.11: Exit plane axial velocity comparison

One method of verification is a comparison of axial velocity profiles at the burner exit

plane. This is visible in Fig. 6.11. It is easy to see that the difference between the two profiles is near-negligible. Perhaps the most striking inconsistency between the 2nd order velocity profile and the corresponding SMD values is the shape of the SMD curve which does not correlate with the velocity curve as expected. In other words, there is not an inverse relationship between velocity magnitude and SMD values per location. This is true for the first order data and also intuitively makes sense due to the role of slip velocity. Since the turbulence quantities are only relevant near the wall (RANS zone), it is likely that the pressure discretization scheme is primarily responsible for the variation in the results. It is conceivable that since the calculation of pressure values at cell faces is carried out differently, the primary atomization region behaves differently between the two simulations. This may cause larger ligaments to form, which subsequently form larger parcels. At the least, these results form a basis for further studies on the effects of discretization/interpolation settings when using the VOF-to-DPM solver.

## 6.3. Droplet population distribution

SMD values are representative of a spray/group of droplets. In order to compare with experiment, parcel properties were averaged across fixed radial intervals. The quantities of interest (SMD, velocity) were then displayed at the center of each interval. The number of parcels per interval is not arbitrary however, as it can provide insight into how the liquid phase spreads inside the domain. Fig. 6.12 shows the number of parcels for each radial interval. Fig. 6.13 shows the same data as Fig. 6.12, but in percentages of the total sample size for clarity. The data shown is that of Simulation 1. The pattern of the distribution is in line with expectations. The largest number of samples was captured not at the center line, but somewhere above. The number of samples declines radially after reaching a peak at roughly r/D=.15. The overall profile is similar in shape to the velocity profile shown in Fig. 6.4. This is due to the higher velocity coflowing stream entraining liquid which eventually reaches the velocity of the gas.

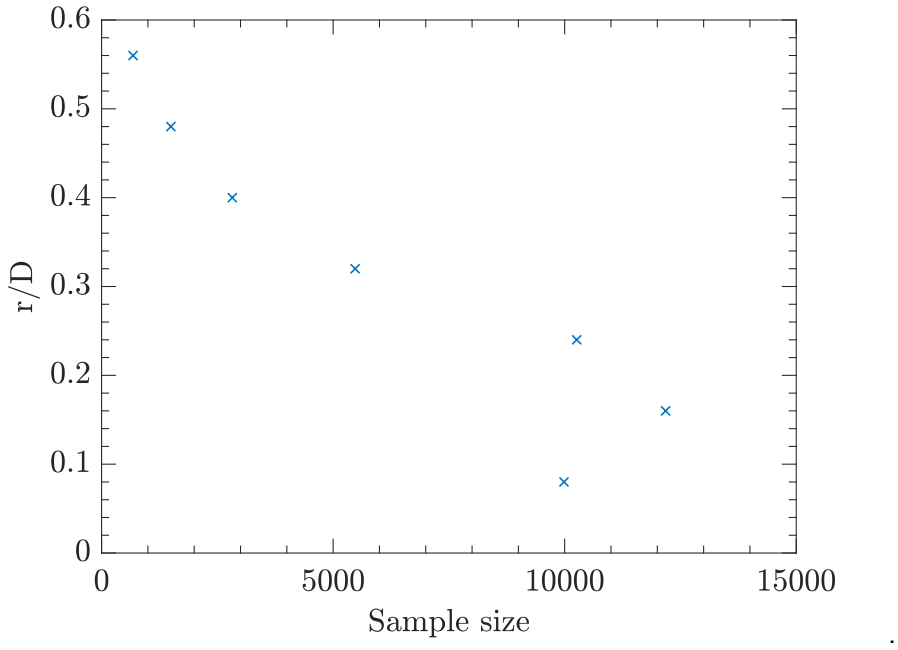


Figure 6.12: Parcels per interval at x/D=.3

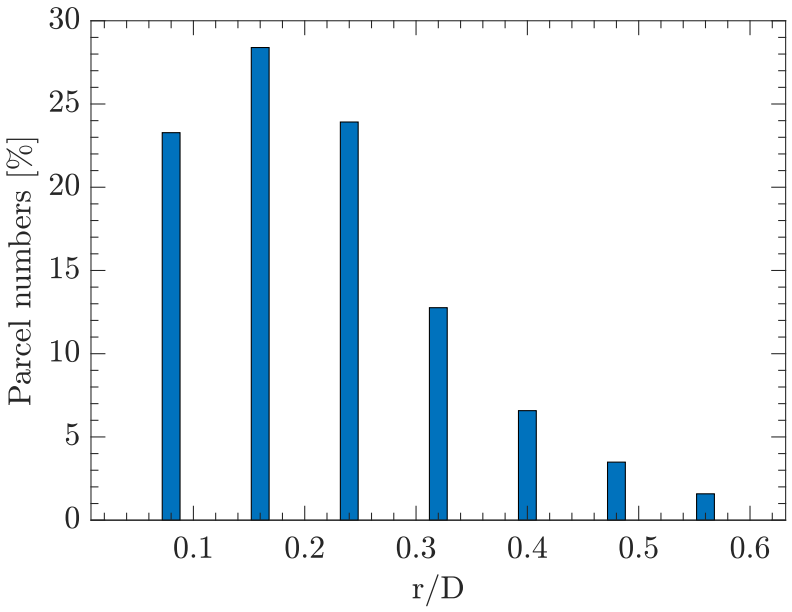


Figure 6.13: Parcel numbers percentages at X/D=.3

As an example of a Rosin-Rammler curve fit, Fig. 6.14 shows the volume percentages of the total sampled droplets from Simulation 1 versus a Rosin-Rammler curve with q=4 and a maximum diameter of 260 microns. For details on the Rosin-Rammler distribution, the reader is referred to section 2.2.

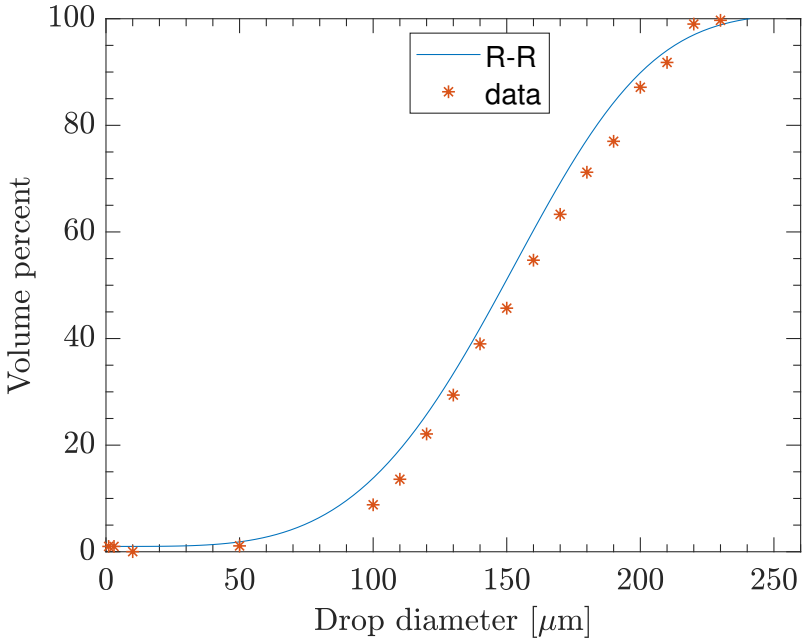


Figure 6.14: Rosin-Rammler fit

The parameters of the Rosin-Rammler distribution can be adjusted to obtain the desired goodness of fit. Once this has been achieved, fully Lagrangian simulations can be performed using the parameters of the Rosin-Rammler curve as an input for injected droplet populations. As a reference for possible subsequent studies, Table 6.3 contains the total number of parcels sampled per simulation and the simulated sampling time. These values provide

an order of magnitude indication of the numbers of samples required for convergence in the case of this study.

Table 6.3: Sample sizes

| Simulation nr | Sample size | Sampling time (ms) |
|---|---|---|
| 1 | 44952 | 4.3 |
| 2 | 45001 | 5.6 |
| 3 | 11444 | 2.4 |
| 4 | 26376 | 2.6 |

The sample sizes are not optimal. In other words, some samples are larger than the bare minimum enforced by the convergence criteria. In addition, some samples required a smaller number of parcels to converge because the changes from one simulation to the other did not affect the flow-field. This is the case for Simulation nr 3, where only the secondary atomization model changed.

## 6.4. Difficulties and solver behaviour

This section contains brief guidelines and observations based on the experience of the author using the VOF-to-DPM solver of Ansys Fluent 19.2. The aim is to aid the work of future users of the solver by pointing out expected solver behaviour.

- The VOF segment is highly sensitive to mesh resolution and cell aspect ratio. There is a minimum amount of resolution required in order for transition from VOF-to-DPM to occur. If transition does not occur and there are no anomalies in the flow-field, it is likely that the mesh is of poor quality (high transition ratios, aspect ratios) or not fine enough.
- Care must be taken when using high refinement levels as cell numbers can increase very rapidly. It is recommended to start with a refinement level of 2 and increase gradually. All simulations presented in this work used a maximum refinement level of 2.
- The k-$\epsilon$ family of turbulence models are known to diverge when using the VOF method due to the sharp difference in velocity at the interface. K-$\omega$ models have built-in turbulence damping which alleviates diverging TKE values [51].
- A common drawback encountered was a prohibitively low time step requirement due to the appearance of small, high velocity areas in the domain. Further work is required to identify the causes for this. The author suspects it may be due to the transition mechanism destabilizing the momentum equation, when using second order discretization. An example of this can be seen in Fig. 6.15. It shows the mid plane velocity magnitude of Simulation 1. Velocity increases from blue to red.
- The Implicit VOF formulation has shown not to yield physical results. The shape of the liquid phase turned out to be counterintuitive and transition did not occur between the VOF and DPM models. Based on the author's experience, the implicit VOF formulation is not recommended for atomization simulations.
- High OVF values can destabilize the simulation in certain cases. If stability issues are encountered, reduce this parameter first. If the simulation still diverges after a reduction of the OVF parameter, momentum discretization should be set to first order. If this does not help, time steps should be reduced until a stable simulation is achieved. The current work has used time steps as low as 1e-08 seconds.
- Solver may not always respect maximum set diameter for ligament conversion to discrete phase. Reasons for this are unclear.

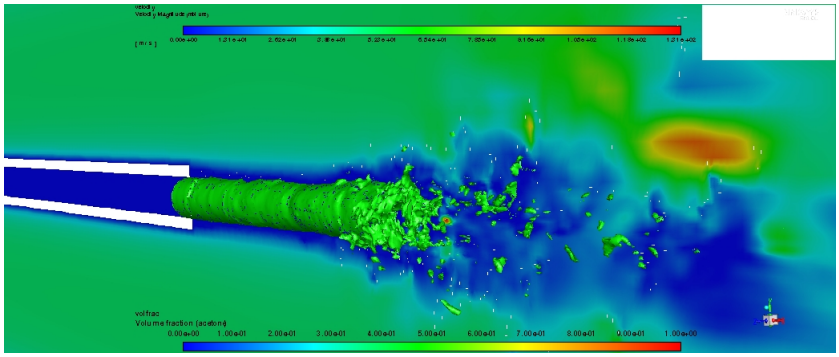

Figure 6.15: High velocity areas

## 6.5. Computation time

An important property of any solver is the computational demand. Since the solver used for this study is relatively new and test cases have not been publicly released at the time of writing of this document, the author considered it relevant to briefly discuss computation time. All simulations were run on a single Dell Precision T5600 machine. Simulations 1-4 were run using 8 cores of the 16 that the Intel Xeon E5-2665 CPU has (this was found to be optimum).

On average it took roughly one week for the transient effects (from initialization) to disperse. This includes time for troubleshooting and dealing with crashes. In the rare case that everything ran smoothly, this would amount to 2-3 days of continuous run time. These values are rough estimates and are to be taken as guidelines only. The sampling run time required for a statistically converging sample is of the order of 2-3 days of continuous run time. This had to be done for each simulation (4 in total). It should also be noted that crashes were quite common, which resulted in at least 7-10 days work per simulation.

An interesting observation regarding computation time is the cost breakdown of different operations. In the experience of the author, the most costly (time-wise) operation was the mesh adaption and not the calculation of flow variables. It was necessary to carefully select how often to adapt the mesh (every n-th iteration) and how often to check the domain for lumps that meet the sphericity criteria. Whenever lumps were converted, the mesh was adapted immediately. If no lumps were converted, the mesh was adapted at intervals selected by the user. Reference values that have shown to produce a stable, reasonably fast simulation can be seen in Table 6.4. The first two parameters from the top are the adaption function limits for coarsening and refinement. The third parameter defines how often dynamic grid adaption takes place (every n-th timestep). The Max Refinement Level indicates how many times a cell may be divided during refinement. The last parameter from the top defines how often (every n-th time step) the algorithm checks if any ligaments have met the conditions for transition into the discrete phase.

Table 6.4: Reference refinement settings

| Simulation nr | Setting |
|---|---|
| Coarsen Threshold | .05 |
| Refine Threshold | .1 |
| Mesh Refinement Interval | 5 |
| Max Refinement Level | 2 |
| Transition criteria check interval | 10 |

The above observations are meant only as a reference for potential future users of the solver. The intent is to convey a sense of how long such a study might take, in order to facilitate planning of future projects.

# 7 Verification

The method used to verify the software employed during this study is the topic of this chapter. The mass balance of the simulation domain is verified via comparison of outflow and inflow quantities. Some of the uncertainties related to the working principle of the solver and its effect on mass conservation are discussed.

## 7.1. Verification

As discussed in the literature study by Pal, there are numerous methods verifying different types of errors in numerical simulations [45]. It is often not possible to properly or fully verify results due to time or resource constraints. Due to the time constraints of the study, it was decided to verify mass flow rate only.

### 7.1.1. Mass flow rate

One of the most important verification metrics, that is also relatively easy to monitor, is the mass imbalance. Mass conservation is fundamental to the mathematical model of any fluid flow problem. If there is a significant mass imbalance in the system, there is no doubt that either the governing equations have not been properly implemented or auxiliary models (such as physical models for multi-phase systems) are introducing unwanted errors.

The mass flow rate of the discrete phase and the continuum phase are treated separately in the VOF-to-DPM solver. The continuum phase does not take the mass of the discrete phase into account. When the transition between the VOF and DPM models occurs, the cells where discrete particles are placed are filled with enough gas to conserve the volume of the cell. In other words, the liquid volume fraction is replaced with gas. At the individual cell level, this will result in a sudden decrease in mass and consequently an increase in velocity in an effort to conserve momentum. At the level of the domain, as a whole, this method should result in an increase of the total mass in the system. This can be verified by checking the mass flow rate at the inlet(s) vs the outlet. Fig. 7.1 shows a sample of the mass flow rate of the discrete phase at the outlet.

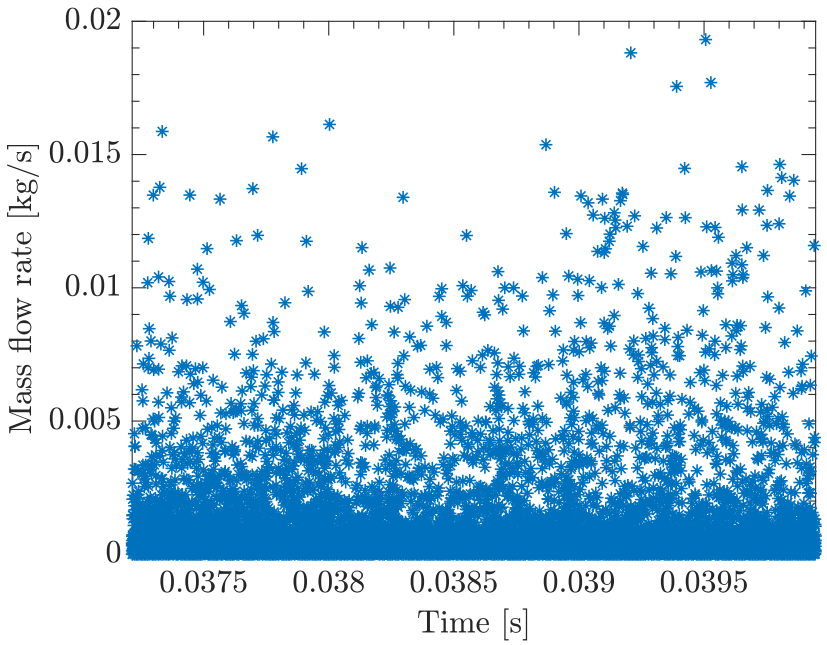


Figure 7.1: Discrete phase mass flow rate

As expected, there are discontinuous increases and decreases in the mass flow rate. These correspond to groups of parcels exiting the domain. The mass flow rate of the continuous phase is kept track of separately and can be seen in Fig. 7.2 for the same time interval.

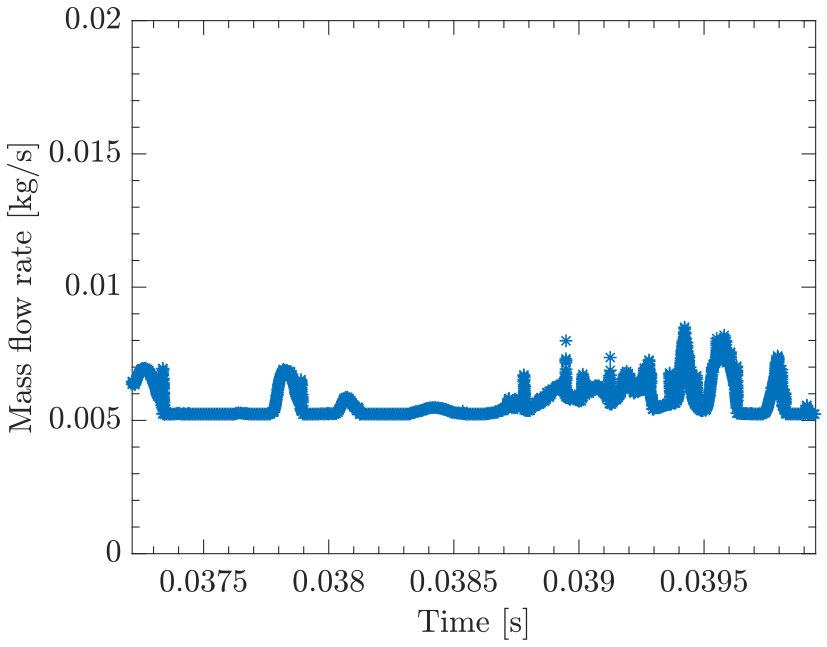


Figure 7.2: Continuum phase mass flow rate

The negative sign indicates outflow. The changes in magnitude likely indicate ligaments still in the VOF phase exiting the domain. The constant mass flow rate in the early segment is probably a time period where only gas is exiting the domain. In order to verify conservation of mass, the mass flow rate of both phases must be summed and examined. This is visible in

Fig. 7.3 below. To obtain the average mass flow rate, the data of Fig. 7.3 is integrated over the given time period. The results can be found in Tab. 7.1:

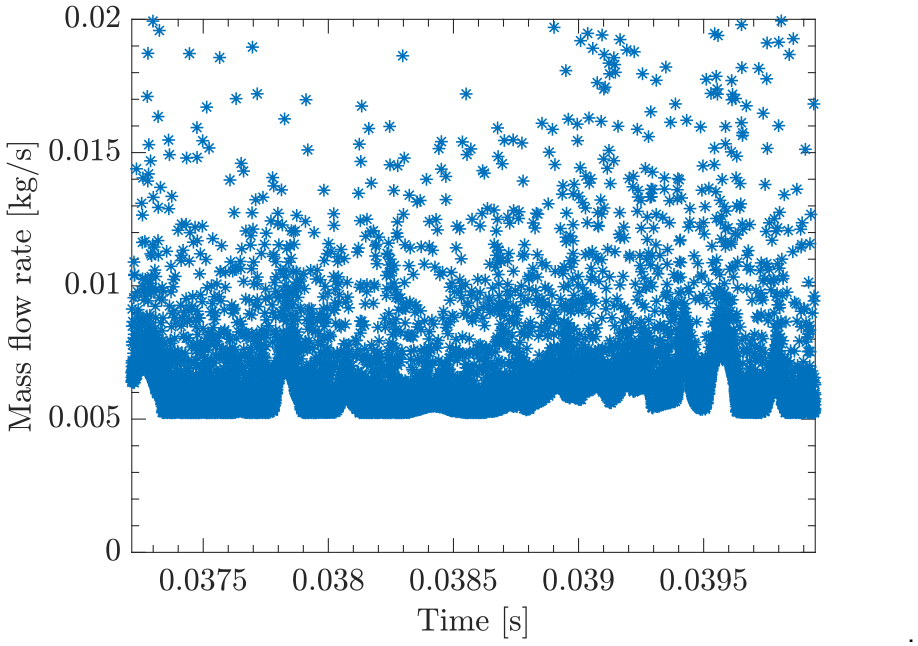


Figure 7.3: Total mass flow rate

Table 7.1: Mass flow rate imbalance

| | Inlet Mass Flow (kg/s) | Total Outlet Mass Flow (kg/s) |
|---|---|---|
| Needle | .737e-03 | N/A |
| Coflowing stream | 4.49e-03 | N/A |
| Pilot stream | .737e-03 | N/A |
| Total | 5.97e-03 | 5.96e-03 |
| % Difference | 0.16 | |

The results from a 2.73 ms sample indicate a mass flow rate that is .16% lower at the outlet than the sum of the inlets. While this is an acceptable error, the important question to answer would be: is the sample size large enough?

### 7.1.2. Discussion

The results seen in Table 7.1 indicate that less mass is leaving the domain than entering. The value of 0.16% is small enough that it can be attributed to integration error since the trapezoidal method was used. This method is known to underestimate the value of integrals. It would then seem that the mass flow rate has been verified and the software calculates mass flow correctly within a reasonable tolerance. What is interesting, however, is that the Fluent Theory Guide [1] states that the source terms of gas introduced during the transition between VOF and DPM models will affect mass balance. What is likely meant by that statement is that if the overall domain is considered, mass is added to the system during each transition. To further elaborate on this, let us consider one liquid ligament that has met sphericity and size criteria for transition to DPM. The mass of the liquid in the cell is assigned to a newly formed discrete parcel. The volume formerly occupied by liquid is filled with gas. The mass of the added gas is in addition to the mass already present in the system. This is not what the results indicate. One of two scenarios is thus possible: either the author misinterpreted

the description of the Fluent Theory Guide or the sample size is not large enough. One way to check the reliability of the sample size is to show its convergence history in time. Table 7.2 shows how error values change with increasing sample size.

Table 7.2: Mass flow rate convergence

| Sample size (ms) | Total Inlet Mass Flow (kg/s) | Total Outlet Mass Flow (kg/s) | %error |
|---|---|---|---|
| 1.32 | 5.97e-03 | 6.12 | 2.5 |
| 1.67 | 5.97e-03 | 6.0 | 0.5 |
| 2.03 | 5.97e-03 | 5.94e-03 | 0.5 |
| 2.73 | 5.97e-03 | 5.96e-03 | 0.16 |

Increasing the sample size results in a decrease in the % difference between inlet and outlet mass flow rates. This is indicative of a converging sample. The collected sample was not large enough to indicate whether or not the error percentages stay constant past a certain sample size. Further investigation is required to confirm that the error percentages stabilize around a mean value. Further investigation is also required to check if the transition mechanism does result in additional mass added to the system.

# 8 Validation

The purpose of this chapter is to compare simulation results with measured data. The first section discusses how convergence was established. Later sections concern qualitative and quantitative validation of the simulation results.

## 8.1. Convergence study

Before the quality of the obtained data set could be analyzed, it was necessary to ensure that the flow field has converged. In other words, it was necessary to confirm that any transient effects resulting from the initialization of the simulation have died out. To this end, the axial velocity profile at the burner exit plane and an upstream location (X=-5e-03 m) were plotted at different simulation times. Fig. 8.1 shows the x velocity profile across the burner exit plane (Simulation nr 1) at four different times. Each profile was recorded 4000 timesteps from the next. The time of the first data set (labeled ”0”) was chosen arbitrarily.

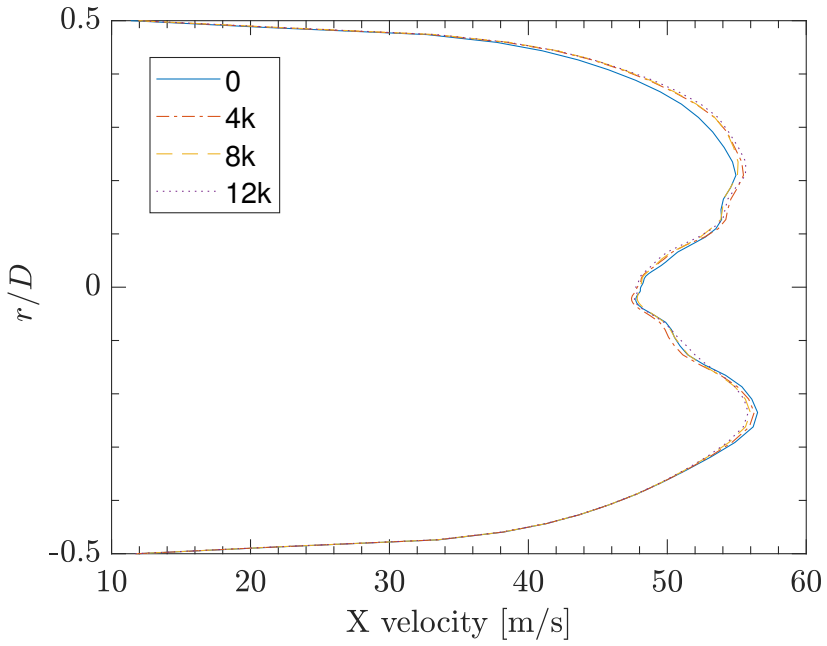


Figure 8.1: Axial velocity profile at exit plane

A discrepancy is visible between the ”0” data set and the remaining ones. The last three sets are closely matching across the entire diameter of the coflowing stream. The error between velocities is less than 5% of the bulk coflow velocity at any height. The same can be

said for the location upstream of the exit plane, seen in Fig. 8.2. The total elapsed time between the first and last dataset is roughly .7 ms. Given that an estimate of the characteristic time of the largest eddies is roughly .1 ms (ratio of coflow radius and bulk velocity magnitude), one could argue that the sampling time is long enough to capture the effects of large scale fluctuations in the flow-field. Once a converged flow-field is obtained, it can be expected that the droplet size distribution at the sampled axial location is also converged.

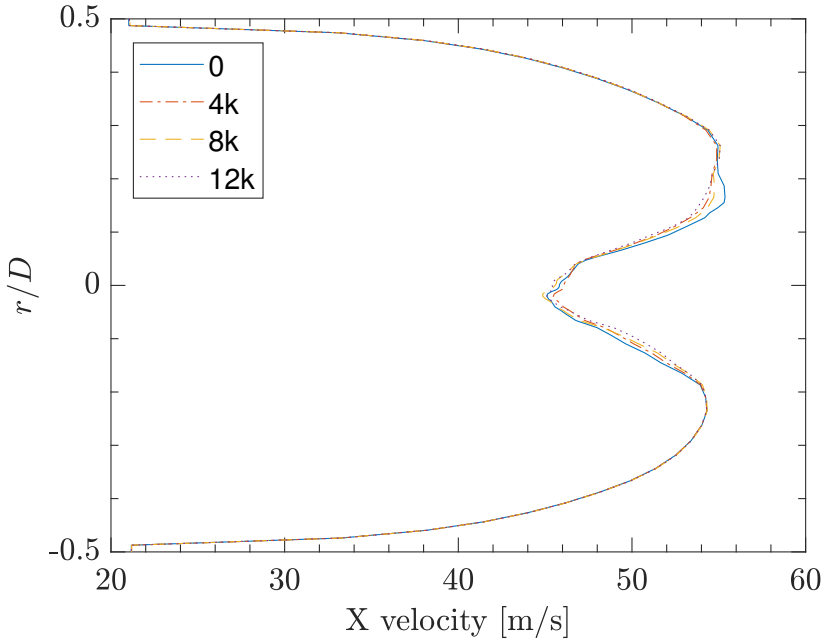


Figure 8.2: Axial velocity profile upstream at X=-5e-03 m

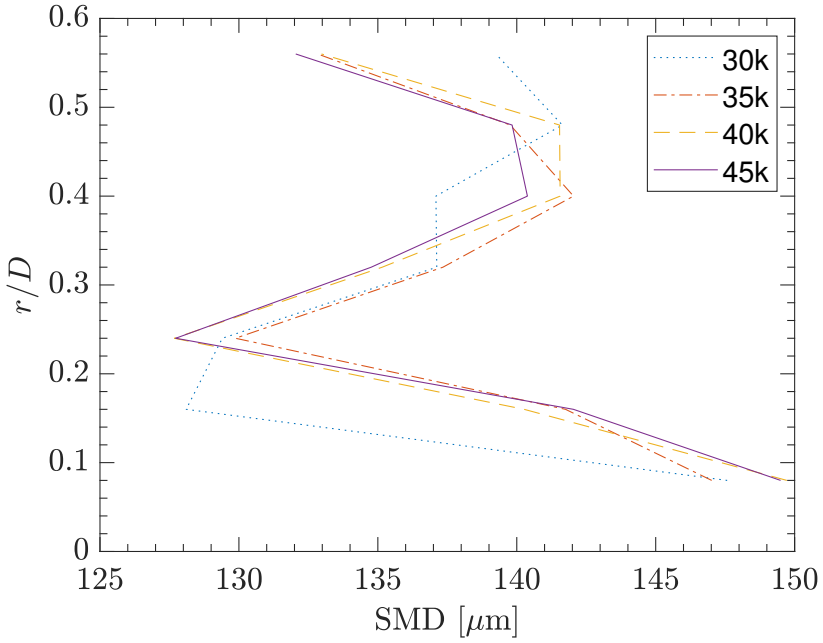


Figure 8.3: SMD convergence history

Fig. 8.3 shows the changing SMD profile with sample size. The data points are connected with lines for clarity. The labels indicate the total number of samples collected across the sampling plane. This data belongs to the same set as the velocity values presented above. It was deemed more relevant to show convergence with an increasing total number of collected droplets than with time. Although there is not a linear decrease in relative error between the data points with increasing sample size at all heights, the magnitude of variation is small between the last two sets.

The **convergence criterion** for SMD values at each measurement interval was determined by the author based on a balance between simulation time and accuracy. All SMD distributions were deemed converged when a 10% change in total sample size resulted in a less than 10% change of SMD at any measurement interval. The appropriateness of this criteria could form a basis for future work.

Residuals are a measure of the imbalance allowed for conservation equations between iterations. They indicate both the accuracy of the obtained solution as well as the convergence of the solution algorithm. As stated by the Ansys Theory Guide, there are no universal parameters for ensuring convergence. It is recommended to check the convergence of quantities of interest as well as the residuals [51]. It is common to examine the pattern of the residuals for each of the solved equations as well as their magnitude. Specifically, the desirable outcome is that the residuals decrease several orders of magnitude at the beginning of a simulation and eventually level out and remain within a certain range. How many orders of magnitude the residuals decrease and what the highest acceptable magnitudes are usually depend on the case being solved. Fig. 8.4 shows a typical distribution of residuals for the performed simulations. Specifically, the globally scaled residuals for simulation nr. 2 over the last 2e04 time steps.

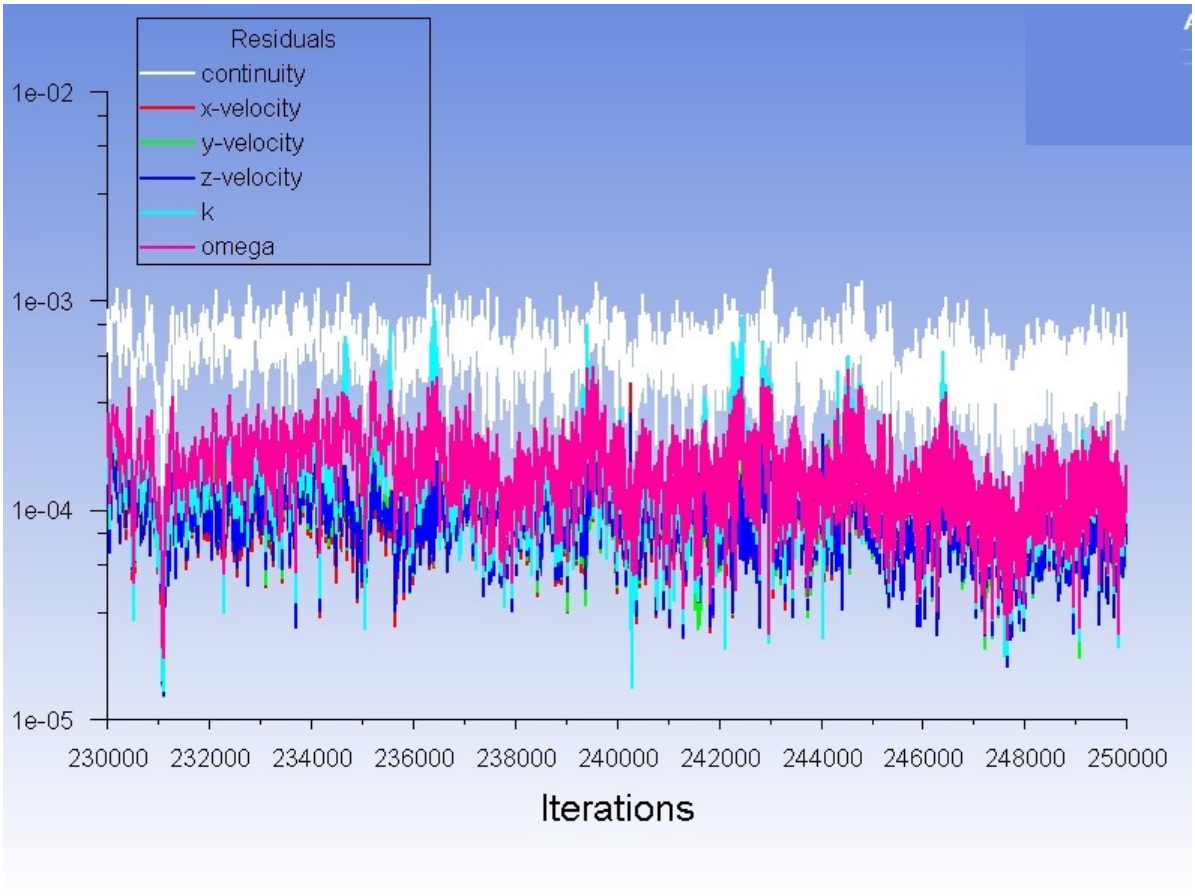


Figure 8.4: Globally scaled residuals

The sum of the residuals of each equation being solved is scaled by the flow-rate through the entire domain of the respective quantity. The convergence threshold was 1e-03 (default value of Ansys Fluent 19.2), which is acceptable for most cases [51]. One can see that all residuals stay below the set threshold and show no tendency to diverge. Given the results of the convergence study and the behaviour of the residuals, these results were deemed sufficient for the purpose of this study. Future work could include a study of the effect of residual convergence thresholds on the accuracy of quantities of interest.

## 8.2. Validation

Experimental data provided by the University of Sydney was used to validate simulation results. The data was released as part of a database to be used for comparison of computational results at the 7th Workshop on Measurement and Computation of Turbulent Spray Combustion (TCS7) held in Tenerife, Spain on June 16th, 2019 [17]. A poster on the results showcased in this work was presented at the workshop. The abstract submitted to the workshop can be found in Appendix A. Details on the experimental procedure can be found in the work of Masri et al. [34]. The data used for the validation of this work was obtained via Laser Doppler Velocimetry (LDV) and Phase Doppler Anemometry (PDA) measurement techniques. The measurement system allowed the simultaneous measurement of droplet velocities and sizes [35]. As mentioned in previous chapters, the provided data set contained droplet axial velocities, diameters and SMD values at several radial locations per individual axial location. The reader should note that although data was provided both above and below the center line of the burner, in order to accelerate the sampling of parcels in the simulation, all values were averaged per radial location. This is reasonable since the experimental data was close to symmetrical about the centerline.

### 8.2.1. Flow-field

Before proceeding to a quantitative validation, it was decided to conduct qualitative comparisons of the flow-field with images from similar cases. The goal was to check if on the macro scale, the patterns seen in the flow-field were similar to experiment and physically meaningful. Fig. 8.5 gives the reader a general overview of the flow field:

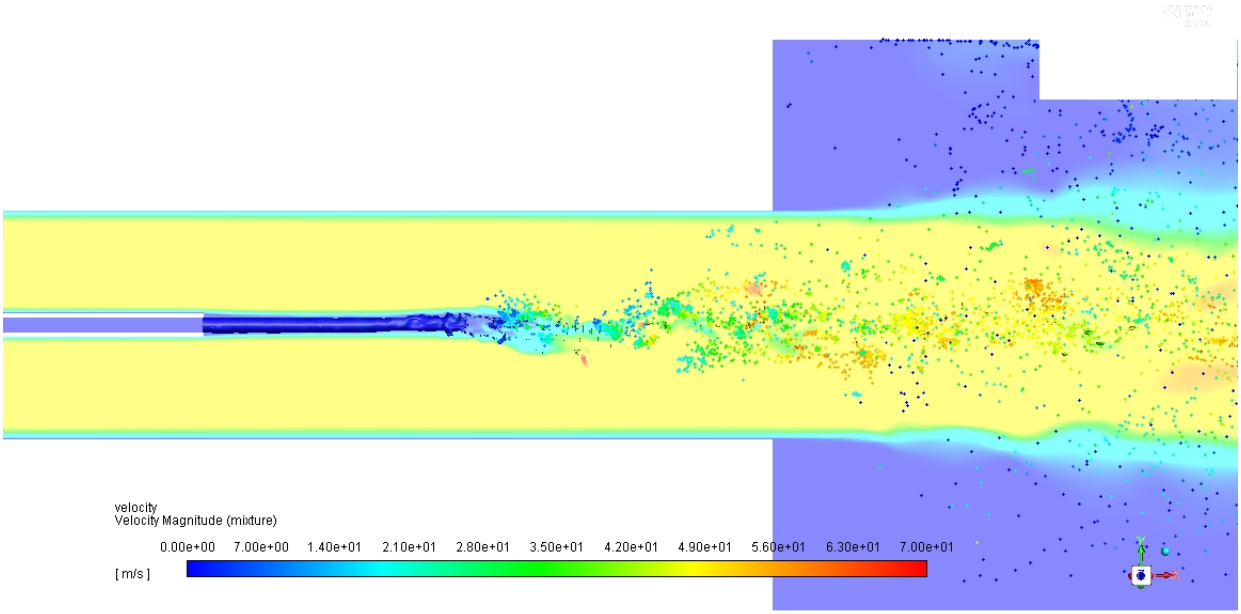


Figure 8.5: Overview of simulated velocity field and gas-liquid interface

The velocity magnitude, the 0.5 volume fraction isosurface and discrete particles are dis-

played in one figure showing the end of the needle and the exit plane of the burner. The rectangular structure at the top right is a watermark and not part of the results.

Since experimental figures inside the burner are not available, similar experimental studies will be used as a qualitative reference. The first comparison is that of Fig. 8.6a (simulation) and Fig. 8.6b (experiment). Fig. 8.6a shows a view of the 0.5 volume fraction iso-surface. Fig. 8.6b was first discussed in Chapter 5 as a reference for the expected outcome of the simulation. The reader is referred to section 5.3 for details.

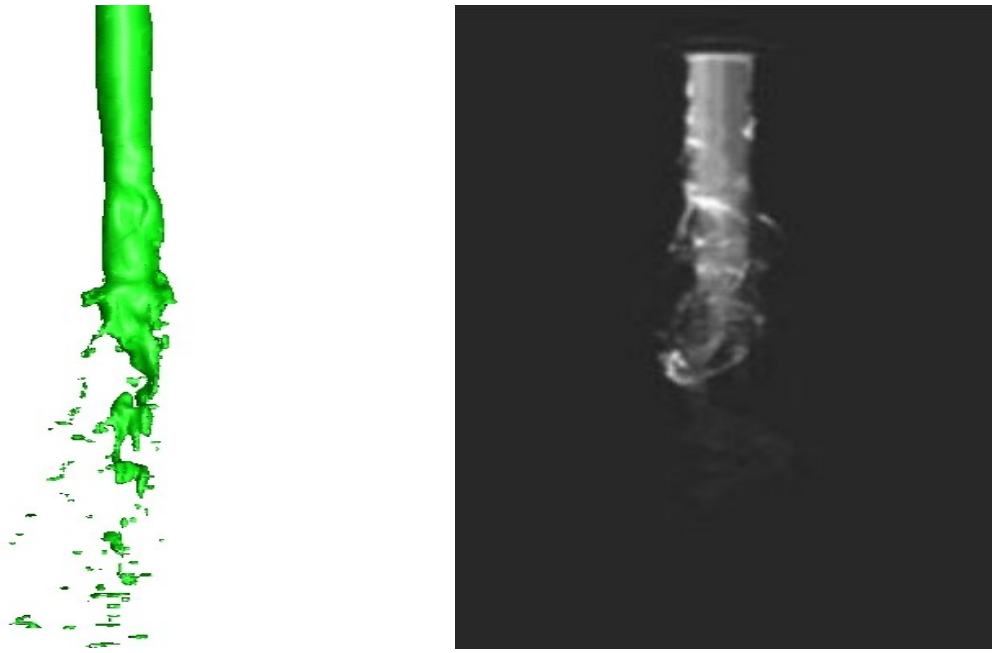

(a) Simulation (b) Experiment [44]

Figure 8.6: Liquid core comparison with experiment

The side-by-side comparison shows that the simulation successfully predicts the formation of an unbroken, elongated liquid core. Small instabilities are visible at the surface of the simulated liquid core, similarly to experiment. Qualitatively, the primary breakup region appears physical and similar to the experimental snapshot. Large ligaments break off initially with some radial displacement. Their size decreases in the axial direction. The dilute region in front of the core is not clearly visible in the experimental figure due to the liquid being illuminated from the interior resulting in decreased light intensity in the axial direction. In addition, the effects of low mesh resolution are visible in the form of elongated ligaments at the bottom of 8.6a. These ligaments appear to conform to the shape of the relatively large cells found close to the wall of the coflow stream (see Fig. 5.4 for details). The overall results of the qualitative comparison indicate, based on the aforementioned flow features, that the simulation correctly predicts the general shape of the liquid core and the primary atomization region.

Apart from the dense regime, the dilute region can also be qualitatively validated via comparison with PIV (Particle Image Velocimetry) figures. Fig. 8.7 shows an instant velocity vector field obtained by a PIV study of the dilute region of a coaxial air-blast atomizer spray. The data was obtained from a different experimental setup of similar geometry.

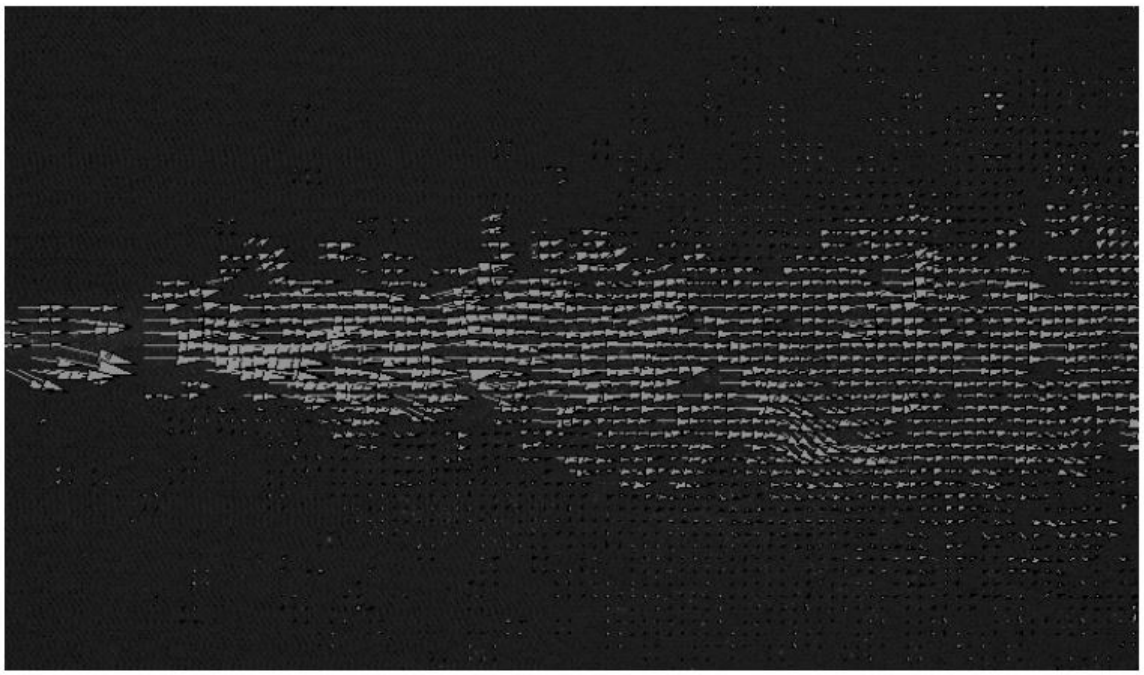

Figure 8.7: Air-blast atomizer PIV [44]

Fig. 8.8 shows the velocity field produced via simulation in the dilute region of the spray inside the burner. The reason the velocity field of the mixture is shown for comparison instead of parcel velocities is clarity. Due to difficulties in obtaining a clear image with non-overlapping vectors or a sufficient amount of particles per plane, it was decided to display the velocity field of the continuum phase instead.

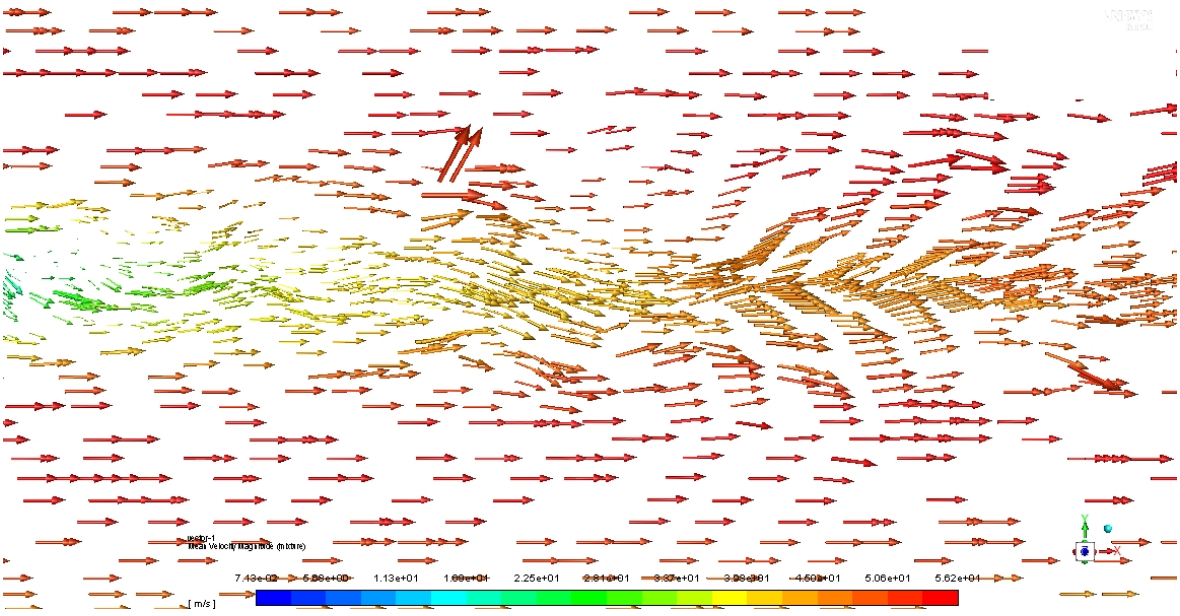


Figure 8.8: Dilute region velocity field

The comparison of Figs. 8.7 & 8.8 qualitatively demonstrates that the simulation correctly predicts radial velocity components close to the injection site. The simulation also correctly predicts that the gas-liquid interface will spread radially, similarly to the growth of an unstable surface wave. This is visible by examining the width of the areas with radial velocity

components. From a qualitative point of view, this reinforces the argument that the general flow structures of the simulation are physical.

### 8.2.2. Droplet properties

This section will compare the sampled droplet properties from the simulation with experiment. The reader is reminded that during the simulation, all droplets were sampled at a plane normal to the burner exit plane and at an axial distance such that X/D=.3. SMD values were calculated for the group of droplets obtained per radial interval. Velocity values were averaged per all the droplets in a radial interval. Fig. 8.9 presents the SMD results of Simulation nr. 1 labeled "sim" vs experimental measurements labeled "exp". At first glance it is clear that the accuracy of the SMD values is off by over 100%. If one looks closer at the shape of the curve however, similarities are noticeable. Locations of local minima and maxima in the SMD vs r/D curve match up. Both distributions have minima at r/D of roughly .25-.3. Both distributions show a local decrease in SMD near the r/D=.6 location. The maxima of both distributions are found at the SMD value closest to the centerline. This is promising because a correct pattern in the size distribution likely indicates that the flow-field has been modeled correctly and the breakup model works as expected. In general, it is physically reasonable that smaller droplets are sampled at higher velocity regions in the flow.

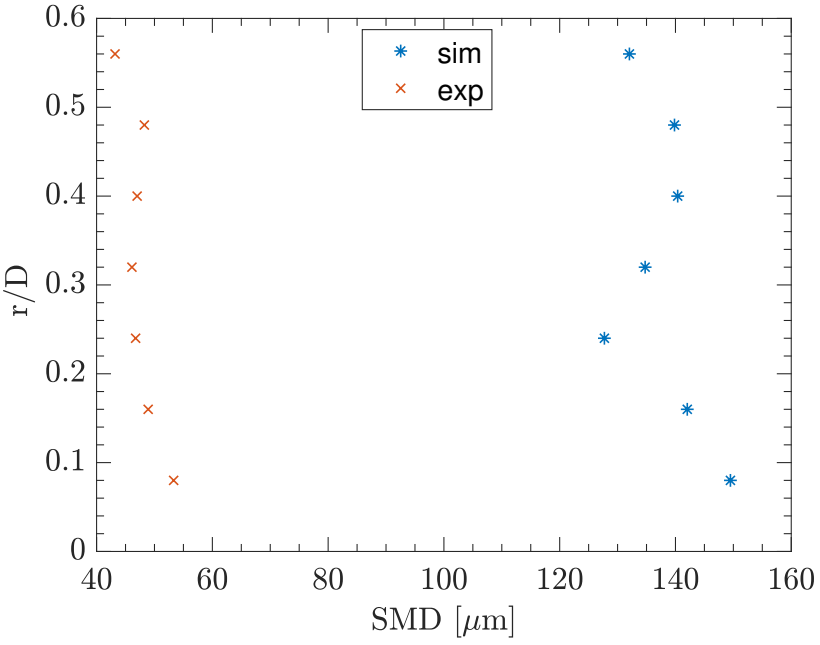


Figure 8.9: Parcel SMD validation - Sim 1

Experimental and simulated droplet velocities can be seen in Fig. 8.10. The experimental data shows a peak of roughly 33m/s at the r/D=.4 location. Velocities decrease towards the centerline and the r/D=.6 location. The experimental velocity is about 5m/s at the highest radial point and in the range of 25 m/s close to the centerline. Regarding the simulated data, there are two anomalies in the shape of the distribution. The highest datapoint (radially) is an increase from the previous one. The other anomaly is the almost perfectly straight line that the first three (counting from the centerline) points form. The highest quantitative discrepancies are found at the extremes of the simulated data: near the centerline and at the r/D=.6 mark.

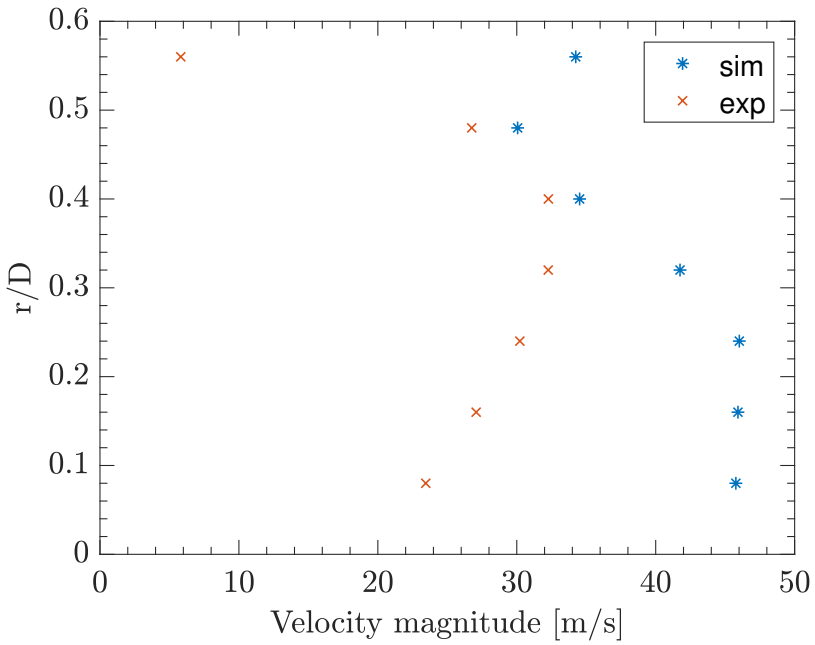


Figure 8.10: Parcel axial velocity validation - Sim 1

Of all the sensitivity studies performed, Simulation nr. 3 (breakup model variation from WAVE to TAB) has shown the most significant positive change in the results. Fig. 8.11 presents the SMD values of Simulation nr. 3 (TAB results) vs experiment. As seen previously in Chapter 6, the shape of the distribution is the same as for Simulation 1, but there is a significant increase in accuracy, bringing the avg. SMD error down to roughly 100%.

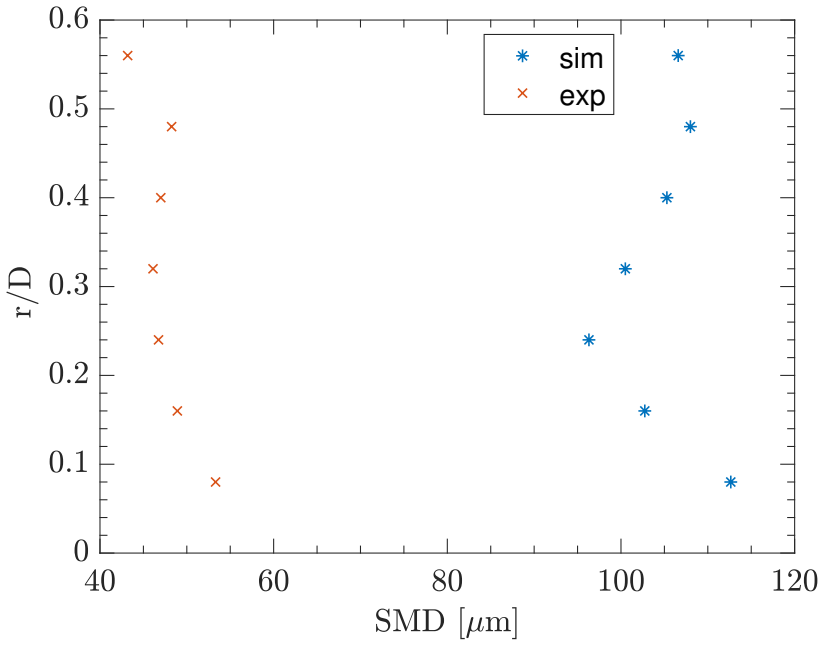


Figure 8.11: Parcel SMD validation - Sim 3

The axial velocity values found in Fig. 8.12 are an improvement over those of Simulation nr. 1. Both discrepancies mentioned earlier are no longer present. Despite the improvement however, the velocity values near the centerline are still not in agreement with the pattern

observed in the SMD values. The simulated data does not exhibit a peak at the r/D=.4 mark and there is not a decrease in velocity values from the r/D=.3 mark towards the centerline.

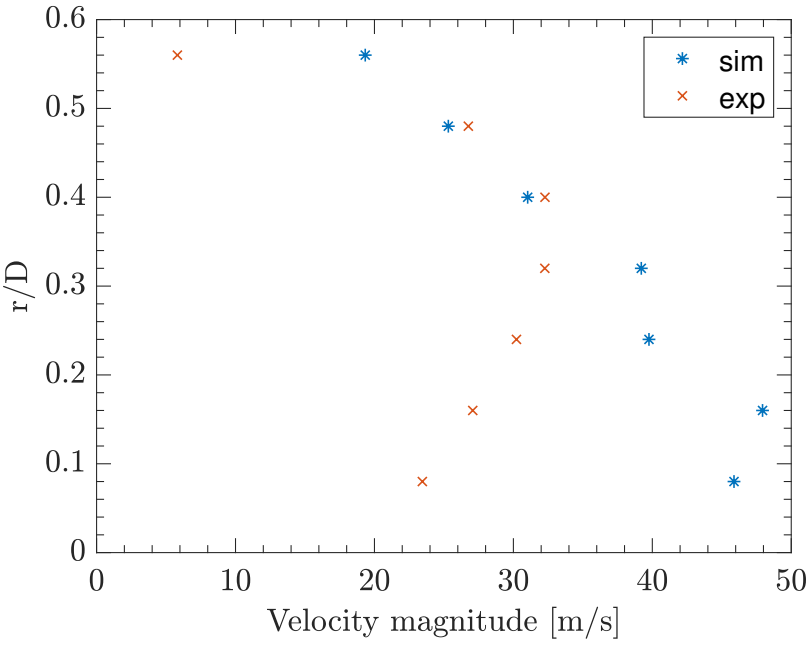


Figure 8.12: Parcel axial velocity validation - Sim 3

## 8.3. Discussion & Analysis

This section will review the results showcased in the chapter and provide an in-depth analysis of the findings in the context of validation. The section follows the structure of chapter 7 and discusses the flow-field, droplet sizes and droplet velocities individually.

### 8.3.1. Flow-field

Examining the general properties of the flow-field produced by the simulation, at first glance the results appear physical. Specifically, in Fig. 8.5, the velocity clearly decreases towards the wall and towards the interface between the gas and the liquid (relative to the bulk velocity of the gas). All the produced droplets and ligaments travel downstream of the injection site as expected. A mixing layer can be seen developing between the pilot and coflow streams.

Taking a closer look at the liquid core, Fig. 8.6 shows good qualitative agreement with experiments at similar conditions. Instabilities can be seen forming on the surface of the liquid core, which eventually break it into ligaments. Some unstable structures are also noticeable in the circumferential direction. It is also important to note that there are two possible reasons why the experimental snapshot in Fig. 8.6b does not show a number of small ligaments downstream of the core: a) the mesh is coarse in the simulation and the ligaments formed are too large and/or b) the light source used to illuminate the liquid column during experiment (from the inside) has lost intensity and cannot illuminate the smaller ligaments downstream. It is likely that both statements apply. The velocity field downstream of the needle exit plane can be qualitatively assessed via comparison of Figs. 8.7 and 8.8. The wave-like structures at the edges of the velocity magnitude field and the spreading of the particles are some indicators of the physicality of the obtained solution.

### 8.3.2. Droplet sizes

As mentioned earlier, the shapes of the simulated SMD curves are similar to their experimental counterparts. This indicates that the physics that govern the motion of droplets have been correctly modeled. There are significant quantitative discrepancies between simulated

and experimentally measured SMD values. A number of points can be made on the reasons behind these. There are two elements to the correct prediction of droplet sizes when using the VOF-to-DPM solver: accuracy of primary atomization prediction and accuracy of secondary break up models. As discussed in Chapter 5, an estimate of the smallest resolvable droplet diameter is about 86 $\mu m$. From experiment, it is known that at X/D=.3 , the average droplet diameter is 26 $\mu m$. A mesh sensitivity analysis is necessary to establish if the current mesh resolution was sufficient to correctly predict primary atomization. It is not unfeasible that the largest droplets are of the order of 86 $\mu m$ and they decay to the range of 26 $\mu m$ by the time they reach the sampling plane. Given the results of the two breakup models however, it is likely that a finer mesh is needed in the primary atomization region. It is also important to note that the estimates carried out for the smallest resolvable diameter in Chapter 5 only concerned the cylindrical volume in line with the needle. The circumferential and radial (y direction) resolution decrease significantly towards the wall of the coflow (see Fig. 5.5 & 5.4). If droplets were to form in this region, they would likely be significantly larger than those close to the needle axis, due to the coarser mesh elements.

### 8.3.3. Droplet velocities

There are two primary mentioned parcel velocity discrepancies that require attention. The first is the previously mentioned increase in velocity at the highest r/D location vs. experiment. This is likely due to a poorly resolved mixing layer between the coflow and pilot streams. A part of the cause is mesh resolution and another part is probably the infinitely thin wall between the two mentioned streams (a simplification of the geometry). The second mentioned anomaly regarding the velocity distribution is the nearly straight, high velocity (relative to experiment) region near the centerline. This is unusual not only because it does not follow the pattern defined by the measured values, but because the corresponding SMD values in the simulation increase towards the centerline. Larger particles will take longer to react and adjust to the flow velocity. For this reason, an inverse pattern would be expected of the velocity. This anomaly is not well understood and will be referenced in comparisons with other datasets.

It is worth reiterating that the expected trend of decreasing SMD values with increasing velocities rests on the assumptions that:

1. Axial velocity magnitude dominates breakup
2. Flow properties upstream of the sampling plane and at the sampling plane are similar
3. The effects of turbulent structures on breakup are insignificant
4. Droplets are rigid spheres

In other words, it is possible that the assumption mentioned in Chapter 6 regarding the inverse relationship between droplet size and axial velocity magnitude is a crude one due to the points presented above. Examining the experimental data, this assumption seemingly holds (except at r/D above .5). The reasons behind it are likely more complex than initially stated. This is indicated by discrepancies in the shape of the velocity curve with two different secondary breakup models.

Keeping in mind the assumptions stated above, let us reexamine the possible reasons for a droplet sample with a correct SMD profile and an incorrect axial velocity profile. One reason could be that the relative velocity magnitude between droplets and the continuum has the correct profile, but the velocity components are incorrect. For example, if near the center line there are turbulent structures which impose a negative axial velocity on the droplets, this could result in the experimental velocity profile. If the simulation does not correctly resolve these structures, it may result in the observed discrepancies. Regarding the assumption of rigid spheres, it is well known that it breaks down with increasing relative velocity. Consequently, it is possible that the drag model used is not appropriate for the problem in question. Specifically, if the drag coefficient is too high for a droplet, its velocity will increase faster than it should. This may be happening near the center line.

In conclusion, the qualitative and quantitative inaccuracies found in the axial velocity results are not completely understood and further research is required.

### 8.3.4. Error summary

The average errors (averaged across all measurement locations) when compared with experiment are tabulated in Table 8.1:

Table 8.1: Mass flow rates

| Simulation nr | Average droplet SMD error(%) | Average droplet velocity error(%) |
|---|---|---|
| Simulation 1 | 190.0 | 107.8 |
| Simulation 2 | 217.9 | 91.7 |
| Simulation 3 | 119.9 | 66.7 |
| Simulation 4 | 222.5 | 102.0 |

While averaged error is not the sole indicator that one set of results is more physically meaningful than the other, it is relevant as a general indicator of accuracy. It is clear from the above data that the results from Simulation 3 are significantly closer to experiment than the others. The conclusion is that the TAB model is more accurate than the WAVE model for the Weber number range in question. In addition, the presented error values give the reader an order of magnitude analysis on the effect of changing different simulation settings.

# 9

# Conclusions & Recommendations

The overall findings of the study are summarized in this chapter. The research questions that were presented at the beginning of the document are answered and recommendations are provided for future studies.

## 9.1. Research Questions

Recall the primary objective of the current study, outlined in Chapter 1:

**The aim of the proposed study is the accurate prediction of spray properties at reasonable computational cost, using the VOF-to-DPM solver.**

Considering the overall results of the study presented in this document, the proposed objective has been achieved for the most part. A simulation of an air-blast atomizer was carried out and a set of spray properties have been obtained. Specifically, SMD and droplet velocity data were extracted from the simulation results. Furthermore, most of the obtained data follow the trends established via experiment. Any discrepancies related to data trends can be justified using numerical or theoretical arguments within reasonable doubt. Accurate results have not been achieved, but steps for future work that are expected to improve accuracy have been outlined. The results produced have had a reasonable computational cost per the definition in Chapter 1. For reference, the research questions seen in Chapter 1 can be found below:

1. Can the Ansys VOF-to-DPM solver predict experimental trends correctly?
   1.1. Are droplet size and velocity trends predicted correctly?
   1.2. What solver parameters and breakup models predict trends correctly?
2. Can the Ansys VOF-to-DPM solver predict spray properties accurately?
   2.1. Are droplet size and velocity values predicted accurately?
   2.2. What solver parameters and breakup models predict spray properties most accurately?

### 9.1.1. On the ability to predict experimental trends

The trend in radial SMD distribution was predicted correctly at the location of interest. Regions of decreasing and increasing SMD values match with experiment. Simulated axial velocity distribution trends do not present a match with experiment. The possible reasons behind this are several: improperly resolved velocity field, improperly predicted breakup locations and droplet diameters, inaccurate drag coefficients etc. It is likely that a refined mesh

will yield significantly better results across the board. It is worth noting that there is a correlation between SMD values and parcel velocities through the drag force. For this reason, if SMD distribution trends are correctly predicted, then it is likely that the trend of velocity magnitude is correct, but the velocity component trends are incorrect.

To summarize, the answer to research question 1.1 is: Droplet size trends are predicted correctly, whereas velocity trends are not. The author believes that results can be significantly improved with subsequent studies.

On research question 1.2, further research is required to provide a full answer. This is partly due to the complex coupling between the physical phenomena at play. For example, the results show that the TAB breakup model did not change the trend of SMD values, but did change the axial velocity distribution. The likely reason is that smaller droplets were produced which reacted to the flow-field differently than larger droplets. Because there is no certainty that the velocity field was correctly resolved, the results do not unequivocally indicate that the TAB model is more appropriate than the WAVE model (even for cases with a similar Weber number).

A smaller OVF parameter has been shown to affect the shape of the SMD curve negatively. Results using an OVF value of 1 vs 2 presented an SMD curve that does not follow the trends of the experimental data set as we move away from the center line. While hypotheses are presented for the cause, the phenomenon is not well understood and requires further work to quantify. To summarize, the current results reinforce the notion that the OVF parameter is a setting that fulfills a purely numerical stability requirement by causing artificial atomization. In order to produce the most physical results, this parameter should be as high as possible.

A switch to higher order discretization of turbulent quantities and to the PRESTO! discretization for the pressure term resulted in a negative change in the shape of the SMD curve. It is hypothesized that this may have to do with the pressure discretization scheme. This is reinforced by a positive change in the shape of the velocity curve near the center line. This is likely the result of a more accurate calculation of turbulent quantities. Since several settings were changed together, the full effect of each change could not be isolated. It is the author's view that due to a reduction in truncation error, higher order discretization schemes for turbulent quantities should improve results. In the case of the pressure term, there is a change in the interpolation method used, the effects of which require further study to confirm. In conclusion, the change in pressure discretization may have been the cause for the worsening of the SMD curve shape, but further studies are required to confirm this.

As a closing remark, it is important to note that there are many parameters that can be varied when using the studied solver. Not all could be tested during this study and their analyses are included as a recommendation for future work. Based on the results obtained so far, the TAB breakup model with a Body-Force Weighted pressure discretization scheme and an OVF parameter of 2 are likely to yield the best results for the studied experiment.

### 9.1.2. On the ability to predict spray properties

Concerning research question 2.1: neither droplet size nor velocity values were predicted accurately per the definition established in Chapter 1. The two properties are related by physical phenomena. Therefore if droplet diameters are inaccurate, then physics dictates that velocities, as a rule, can not be accurate. It is hypothesized based on the solver documentation and the physics of the problem, that the prediction of droplet sizes will improve significantly with a finer mesh. The improvement in droplet diameters is expected to reduce droplet velocity error. It should be noted however, that there are many physical models that determine the velocity of a droplet. These are: drag model, dispersion model, one-way/two-way coupling and phase transition mechanism. It is therefore difficult to predict the source of the inaccuracy of the velocity of a droplet, without examining the sensitivity to the mentioned models. To summarize: further study is required to examine the reasons for droplet velocity discrepancies. It is the author's hypothesis that a mesh refinement study and sensitivity studies of the mentioned physical models will provide insight into the primary cause of the velocity error.

Regarding research question 2.2, the results using the TAB breakup model with a Body-Force Weighted pressure discretization and an OVF parameter of 2 have produced the least

average error (averaged over all radial locations). While these results may serve as a good reference for future studies, it should be noted that they may not produce results of equal quality for other experiments. This is due to the problem dependence of both the breakup model and the discretization scheme. The OVF parameter should produce more physical results regardless of the simulated case.

## 9.2. Recommendations for future work

While the results presented herein are promising, there is still much work to be done in the pursuit of accuracy and reliability. The following studies are therefore recommended as follow-up work:

- **Comparison of breakup models** - Breakup models other than the ones considered in this work should be evaluated. As seen previously, their effect on the resulting droplet diameters can be very significant.
- **Higher order schemes** - Further work could be done using other discretization/interpolation schemes for flow and turbulence quantities. As seen from the sensitivity studies performed in this work, the effects on the results can be significant.
- **Turbulence model comparison** - Subsequent studies could compare different SGS models (in the case of LES) or RANS turbulence models. The Scale Adaptive Simulation model recommended by Ansys could be of interest [52].
- **Mass flow rate imbalance quantification** - Further study is required to confirm the mechanism by which mass is added to the domain during phase transition. A comparison of relative mass imbalance using different grid sizes could clarify the significance of this effect. It is the author's hypothesis that the relative mass imbalance should not change with grid refinement.
- **Two-way coupling** - All simulations during this study neglected the effect of the discrete phase on the gaseous phase. This assumption holds only if the volume of the liquid phase is negligible per control volume. This may not be true all of the time, especially close to the primary atomization zone. It is therefore necessary to analyze how results are affected when the gaseous phase can be disturbed by the discrete phase.
- **Transition tolerances** - The tolerances on the two asphericity criteria govern which ligaments are converted into the discrete phase. These were kept constant during this study. It would be meaningful to analyze how droplet diameters are affected when the asphericity criteria are tightened. This should delay the transiton of ligaments to the discrete phase, as they would have to be more spherical. Consequently, it is possible that smaller droplets would form and that transition would occur further from the injection site. A reduction in purely numerical atomization caused by the use of low OVF parameters may also occur. Since the VOF phase would be present in the domain longer, it is expected that the computational cost would go up.
- **Comparison of drag models** - Several empirical models are available for the drag coefficient used in the particle equations of motion. A comparison of the results using different models could identify the degree to which the particle velocities are affected.

## 9.3. Closing remarks

The VOF-to-DPM solver has the potential to predict spray properties accurately. Further work is required to confirm the highest accuracy that the solver is able to provide. Because a full mesh sensitivity study could not be carried out, the full capabilities of the solver are yet to be revealed. What can be stated, based on the results of this work, is that the VOF-to-DPM solver can provide physically meaningful results on spray properties without requiring experimental data as input. It therefore has the potential of becoming a predictive tool for

injector/combustor design. Due to its hybrid approach to atomization modeling and dynamic mesh refinement capability, the solver shows promise as far as reducing computational demand. This can be a significant advantage in a field such as atomization, where a large range of spatial scales must often be resolved. This study is a step towards showcasing the potential of hybrid two-phase flow solvers for atomization prediction. With advances in high performance computing, propulsion engineers may soon have the tools to reliably simulate a newly designed injector in a matter of days to weeks. For a throttleable injector, the capability of quickly simulating a range of operating conditions could reduce development costs dramatically and facilitate trade studies.

# Bibliography


[1] Fluent theory guide(19.2). Technical report, Ansys Inc., 2018.

[2] Capabilities and services, nov 2018. URL https://www.spacex.com/about/capabilities.

[3] Making life multiplanetary, nov 2018. URL http://www.spacex.com/mars.

[4] Ariane 6 rocket sees first commercial deals in race with spacex, feb 2019. URL https://www.reuters.com/article/us-arianegroup-contracts/ariane-6-rocket-sees-first-commercial-deals-in-race-with-spacex-idUSKCN1QA2BW.

[5] French auditor says ariane 6 rocket too conventional to compete with spacex, feb 2019. URL https://arstechnica.com/science/2019/02/french-auditor-says-ariane-6-rocket-too-conventional-to-compete-with-spacex/.

[6] Exomars landing platform arrives in europe with a name, march 2019. URL https://www.esa.int/Our_Activities/Human_and_Robotic_Exploration/Exploration/ExoMars/ExoMars_landing_platform_arrives_in_Europe_with_a_name.

[7] Rahul Anand, PR Ajayalal, Vikash Kumar, A Salih, and K Nandakumar. Spray and atomization characteristics of gas-centered swirl coaxial injectors. *International Journal of Spray and Combustion Dynamics*, 9(2):127–140, 2017. doi: 10.1177/1756827716660225. URL https://doi.org/10.1177/1756827716660225.

[8] Tariq Ahmed Abul Kalam Azad. Computational Modeling of Turbulent Ethanol Spray Flames in a Hot Diluted Coflow using OpenFOAM. Master's thesis, Delft University of Technology, Delft, Netherlands, 2015.

[9] Erin Betts and Robert Frederick. A Historical Systems Study of Liquid Rocket Engine Throttling Capabilities. American Institute of Aeronautics and Astronautics, July 2010. ISBN 978-1-60086-958-7. doi: 10.2514/6.2010-6541. URL http://arc.aiaa.org/doi/abs/10.2514/6.2010-6541.

[10] Ambrus Both. RANS-FGM simulation of n-heptane spray flame in OpenFOAM. Master's thesis, Delft University of Technology, Delft, Netherlands, 2017.

[11] J.U Brackbill, D.B Kothe, and C Zemach. A continuum method for modeling surface tension. *Journal of Computational Physics*, 100(2):335 – 354, 1992. ISSN 0021-9991. doi: https://doi.org/10.1016/0021-9991(92)90240-Y. URL http://www.sciencedirect.com/science/article/pii/002199919290240Y.

[12] M. Broumand and M. Birouk. Liquid jet in a subsonic gaseous crossflow: Recent progress and remaining challenges. *Progress in Energy and Combustion Science*, 57: 1 – 29, 2016. ISSN 0360-1285. doi: https://doi.org/10.1016/j.pecs.2016.08.003. URL http://www.sciencedirect.com/science/article/pii/S0360128516300235.

[13] Matthew J. Casiano, James R. Hulka, and Vigor Yang. Liquid-Propellant Rocket Engine Throttling: A Comprehensive Review. *Journal of Propulsion and Power*, 26(5):897–923, September 2010. ISSN 0748-4658, 1533-3876. doi: 10.2514/1.49791. URL http://arc.aiaa.org/doi/10.2514/1.49791.

[14] C. T. Crowe. *Multiphase flows with droplets and particles*. CRC Press, Boca Raton, FL, 2nd ed. / edition, 2012. ISBN 978-1-4398-4051-1 1-4398-4051-2. doi: 10.1201/b11103. URL http://www.crcnetbase.com/isbn/9781439840511.

[15] J. Dannenhoffer, Iii and J. Baron. Grid adaptation for the 2-D Euler equations. In *23rd Aerospace Sciences Meeting*, Reno,NV,U.S.A., January 1985. American Institute of Aeronautics and Astronautics. doi: 10.2514/6.1985-484. URL http://arc.aiaa.org/doi/10.2514/6.1985-484.

[16] Gordon Dressler and J. Bauer. TRW pintle engine heritage and performance characteristics. American Institute of Aeronautics and Astronautics, July 2000. doi: 10.2514/6.2000-3871. URL http://arc.aiaa.org/doi/10.2514/6.2000-3871.

[17] *7th Workshop on Measurement and Computation of Turbulent Spray Combustion (TCS7)*, Tenerife, Spain, 6 2019. ERCOFTAC special interest group 28.

[18] G.M Faeth, L.-P Hsiang, and P.-K Wu. Structure and breakup properties of sprays. *Annual Reviews in Multiphase Flow 1995*, 21:99–127, December 1995. ISSN 0301-9322. doi: 10.1016/0301-9322(95)00059-7. URL http://www.sciencedirect.com/science/article/pii/0301932295000597.

[19] Xin-xin Fang and Chi-bing Shen. Study on atomization and combustion characteristics of LOX/methane pintle injectors. *Acta Astronautica*, 136:369–379, July 2017. ISSN 00945765. doi: 10.1016/j.actaastro.2017.03.025. URL http://linkinghub.elsevier.com/retrieve/pii/S0094576516309298.

[20] P. Gaillard, C. Le Touze, L. Matuszewski, and A. Murrone. Numerical Simulation of Cryogenic Injection in Rocket Engine Combustion Chambers. *AerospaceLab*, (11):16, 2016. URL https://hal.archives-ouvertes.fr/hal-01369627.

[21] Gautam V. and Gupta A.K. Cryogenic flow and atomization from a coaxial injector. *Journal of Propulsion and Power*, 25(1):33–39, 2009. ISSN 0748-4658. doi: 10.2514/1.28921. 33.

[22] Georgios Charalampous, Yannis Hardalupas, and Alex Taylor. Structure of the Continuous Liquid Jet Core during Coaxial Air-Blast Atomisation. *International Journal of Spray and Combustion Dynamics*, 1(4):389–415, 2009. ISSN 1756-8277. doi: 10.1260/175682709789685840. 389.

[23] Carlos Gonzalez. Spacex launched a tesla into deep orbit—now what?, feb 2018. URL https://www.machinedesign.com/motion-control/spacex-launched-tesla-deep-orbit-now-what.

[24] Yogish Gopala, Peng Zhang, Oleksandr Bibik, Eugene Lubarsky, and Ben Zinn. Liquid Fuel Jet in Crossflow -Trajectory Correlations based on the Column Breakup Point. In *48th AIAA Aerospace Sciences Meeting Including the New Horizons Forum and Aerospace Exposition*, Aerospace Sciences Meetings. American Institute of Aeronautics and Astronautics, January 2010. doi: 10.2514/6.2010-214. URL https://doi.org/10.2514/6.2010-214.

[25] A. D. Gosman and E. loannides. Aspects of Computer Simulation of Liquid-Fueled Combustors. *Journal of Energy*, 7(6):482–490, November 1983. ISSN 0146-0412. doi: 10.2514/3.62687. URL https://doi.org/10.2514/3.62687.

[26] William R Hammock and Arlie E Fisher. Apollo experience report - descent propulsion system. Technical report, National Aeronautics and Space Administration, 03 1973.

[27] D.K. Huzel and D.H. Huang. *Design of liquid propellant rocket engines*. NASA SP. Scientific and Technical Information Office, National Aeronautics and Space Administration; [for sale by the National Technical Information Service, Springfield, Va.], 1971. URL https://books.google.nl/books?id=7BQZE5FcTl4C.

[28] The Combustion Institute. 7th workshop on measurement and computation of turbulent spray combustion (tcs7), jun 2019. URL https://www.combustioninstitute.org/ci-event/7th-workshop-on-measurement-and-computation-of-turbulent-spray-combustion-tcs7/.

[29] Patrick Jenny, D Roekaerts, and Nijso Beishuizen. Modeling of turbulent dilute spray combustion. *Progress in Energy and Combustion Science*, 38:846–887, 12 2012. doi: 10.1016/j.pecs.2012.07.001.

[30] Min Wook Lee, Jung Jae Park, Massoud Massoudi Farid, and Sam S. Yoon. Comparison and correction of the drop breakup models for stochastic dilute spray flow. *Applied Mathematical Modelling*, 36(9):4512 – 4520, 2012. ISSN 0307-904X. doi: https://doi.org/10.1016/j.apm.2012.02.015. URL http://www.sciencedirect.com/science/article/pii/S0307904X12000972.

[31] Arthur H. Lefebvre and Vincent G. McDonell. *Atomization and sprays*. CRC Press, Taylor & Francis Group, CRC Press is an imprint of the Taylor & Francis Group an informa business, Boca Raton, second edition edition, 2017. ISBN 978-1-4987-3625-1.

[32] Arthur H. Lefebvre, Dillip R. Ballal, and DONALD W. BAHR. *Gas Turbine Combustion—Alternative Fuels and Emissions*. CRC Press, Taylor & Francis Group, Boca Raton, third edition edition, August 2010. ISBN 9781420086058. doi: 10.1115/1.4001927. URL http://dx.doi.org/10.1115/1.4001927.

[33] Marcel. Lesieur. *Turbulence in fluids*. Fluid mechanics and its applications ; v. 84. Springer, Dordrecht ;, 4th rev. and enl. ed. edition, 2007. ISBN 9781402064357 1402064357 9781402064340 1402064349 9786611339296 6611339299. URL http://www.myilibrary.com?id=133929.

[34] Alby Lowe, Agisilaos Kourmatzis, and Assaad R. Masri. Turbulent spray flames of intermediate density: Stability and near-field structure. *Combustion and Flame*, 176: 511–520, 02 2017. doi: 10.1016/j.combustflame.2016.10.024.

[35] Albyn Lowe. *Flow and Turbulent-Field Structure of Turbulent Spray Flames: From Dilute to Dense*. PhD thesis, The University of Sydney, 1 2018.

[36] Edward John Mercieca. Spray Characteristics in Gas/Liquid Pintle Injection. Master's thesis, Delft University of Technology, Delft, Netherlands, 2017.

[37] S. A. Morsi and A. J. Alexander. An investigation of particle trajectories in two-phase flow systems. *Journal of Fluid Mechanics*, 55(2):193–208, 1972. doi: 10.1017/S0022112072001806.

[38] A. Murrone, N. Fdida, C. Le Touze, and L. Vingert. Atomization of cryogenic rocket engines coaxial injectors. Modeling aspects and experimental investigations. In *Space Propulsion 2014*, COLOGNE, Germany, May 2014. URL https://hal-onera.archives-ouvertes.fr/hal-01068686.

[39] Afshin Ahmadi Nadooshan and Ebrahim Shirani. Interface pressure model for surface tension force for vof-based methods in interfacial flows. *Engineering Applications of Computational Fluid Mechanics*, 2(4):496–513, 2008. doi: 10.1080/19942060.2008.11015247. URL https://doi.org/10.1080/19942060.2008.11015247.

[40] Rene Nardi, Vladia Perez, and Amilcar Pimenta. Experiments with Pintle Injector Design and Development. In *51st AIAA/SAE/ASEE Joint Propulsion Conference*, Orlando, FL, July 2015. American Institute of Aeronautics and Astronautics. ISBN 978-1-62410-321-6. doi: 10.2514/6.2015-3810. URL http://arc.aiaa.org/doi/10.2514/6.2015-3810.

[41] NASA. Verification assessment, 2008. URL https://www.grc.nasa.gov/WWW/wind/valid/tutorial/verassess.html.

[42] S. Ninish, Aravind Vaidyanathan, and K. Nandakumar. Spray characteristics of liquid-liquid Pintle injector. *Experimental Thermal and Fluid Science*, 97:324–340, October 2018. ISSN 08941777. doi: 10.1016/j.expthermflusci.2018.03.033. URL https://linkinghub.elsevier.com/retrieve/pii/S0894177718304874.

[43] P.J. O'Rourke and A.A. Amsden. The tab method for numerical calculation of spray droplet breakup. 1 1987.

[44] Daniel P. Hoeg, Zhen Wang, Peter Friedman, and R.N. Laoulache. Investigation of a coaxial air-blast atomizer using particle image velocimetry and computational fluid dynamics. *Atomization and Sprays - ATOMIZATION SPRAYS*, 18:739–759, 01 2008. doi: 10.1615/AtomizSpr.v18.i8.40.

[45] Botond Pal. Pintle injector spray modeling. Technical report, TU Delft, Delft, Netherlands, 10 2018.

[46] Christos Panagopoulos. Theoretical and Numerical Analysis of Laminar Ethanol Spray Flames for the creation of a Spray Flamelet Library. Master's thesis, Delft University of Technology, Delft, Netherlands, 2017.

[47] Vlad Petrescu, Ferdinand Schrijer, and B.T.C. Zandbergen. Atomized spray properties in pintle injection. Technical report, TU Delft, 10 2017.

[48] Kanmaniraja Radhakrishnan, Min Son, Keonwoong Lee, and Jaye Koo. Effect of injection conditions on mixing performance of pintle injector for liquid rocket engines. *Acta Astronautica*, December 2017. ISSN 00945765. doi: 10.1016/j.actaastro.2017.12.012. URL http://linkinghub.elsevier.com/retrieve/pii/S0094576517317782.

[49] Rolf Reitz. Modeling atomization processes in high-pressure vaporizing sprays. *Atomisation Spray Technology*, 3:309–337, 01 1987.

[50] S S. PENNER. On maximum evaporation rates of liquid droplets in rocket motors 1. *Journal of the American Rocket Society*, 23, 03 1953. doi: 10.2514/8.4548.

[51] Muhammad Sami. Ansys fluent 19.0 speeds up cfd spray simulations, Jun 2018. URL https://www.ansys-blog.com/fluent-19-speeds-cfd-spray-simulations/.

[52] Muhammad Sami. Vof-lagrangian hybrid spray modeling [webinar], May 2018.

[53] Eckart Schmidt, Gerald T. Brewster, and George E. Cain. Mars lander retro propulsion. In *Proceedings of the 50th International Astronautical Congress*, 10 1999.

[54] Jayanth Sekar, Arvind Rao, Sreedhar Pillutla, Allen Danis, and Shih-Yang Hsieh. Liquid Jet in Cross Flow Modeling. (45691):V04BT04A013, 2014. doi: 10.1115/GT2014-26124. URL http://dx.doi.org/10.1115/GT2014-26124.

[55] Ethan Siegel. Spacex's falcon heavy launch brings humanity one giant leap closer to mars, feb 2018. URL https://www.forbes.com/sites/startswithabang/2018/02/08/the-falcon-heavy-launch-by-spacex-changes-the-game-for-getting-to-mars/.

[56] Min Son, Kijeong Yu, Jaye Koo, Oh Chae Kwon, and Jeong Soo Kim. Effects of momentum ratio and Weber number on spray half angles of liquid controlled pintle injector. *Journal of Thermal Science*, 24(1):37–43, February 2015. ISSN 1003-2169, 1993-033X. doi: 10.1007/s11630-015-0753-7. URL http://link.springer.com/10.1007/s11630-015-0753-7.

[57] Min Son, Kijeong Yu, Kanmaniraja Radhakrishnan, Bongchul Shin, and Jaye Koo. Verification on spray simulation of a pintle injector for liquid rocket engine. *Journal of Thermal Science*, 25(1):90–96, February 2016. ISSN 1003-2169, 1993-033X. doi: 10.1007/s11630-016-0838-y. URL http://link.springer.com/10.1007/s11630-016-0838-y.

[58] Min Son, Kanmaniraja Radhakrishnan, Jaye Koo, Oh Chae Kwon, and Heuy Dong Kim. Design Procedure of a Movable Pintle Injector for Liquid Rocket Engines. *Journal of Propulsion and Power*, 33(4):858–869, July 2017. ISSN 0748-4658, 1533-3876. doi: 10.2514/1.B36301. URL https://arc.aiaa.org/doi/10.2514/1.B36301.

[59] George P. Sutton and Oscar Biblarz. *Rocket propulsion elements*. John Wiley & Sons, New York, 7th ed edition, 2001. ISBN 978-0-471-32642-7.

[60] Hiroumi Tani, Susumu Teramoto, and Koji Okamoto. Effects of injector geometry on cryogenic shear coaxial jets at supercritical pressures. *Journal of Propulsion and Power*, 31:1–6, 01 2015. doi: 10.2514/1.B35530.

[61] Brunno Vasques and Oskar Haidn. Effect of Pintle Injector Element Geometry on Combustion in a Liquid Oxygen/Liquid Methane Rocket Engine. In *7TH European Conference For Aeronautics and Aerospace Sciences (EUCASS)*. EUCASS, 2017. doi: 10.13009/eucass2017-88.

[62] H. K. Versteeg and W. Malalasekera. *An introduction to computational fluid dynamics: the finite volume method*. Pearson Education Ltd, Harlow, England ; New York, 2nd ed edition, 2007. ISBN 978-0-13-127498-3. OCLC: ocm76821177.

[63] Mike Wall. Wow! spacex lands orbital rocket successfully in historic first. URL https://www.space.com/31420-spacex-rocket-landing-success.html.

[64] Shang J Wang. Analysis of the continuum surface force method. Technical report, Delft University of Technology, 2015.

[65] Zhen-Guo Wang. *Internal combustion processes of liquid rocket engines*. Wiley, Singapore, 2016. ISBN 978-1-118-89003-5 1-118-89003-5 978-1-118-89004-2 1-118-89004-3 978-1-118-89005-9 1-118-89005-1 1-118-89002-7 978-1-118-89002-8. URL http://search.ebscohost.com/login.aspx?direct=true&scope=site&db=nlebk&db=nlabk&AN=1239713.

[66] K. Warncke, S. Gepperth, B. Sauer, A. Sadiki, J. Janicka, R. Koch, and H.-J. Bauer. Experimental and numerical investigation of the primary breakup of an airblasted liquid sheet. *International Journal of Multiphase Flow*, 91:208–224, 2017. ISSN 0301-9322. doi: 10.1016/j.ijmultiphaseflow.2016.12.010. 208.

[67] Chun-guo Yue, Xin-Long Chang, Shu-jun Yang, and You-hong Zhang. Numerical Simulation of a Pintle Variable Thrust Rocket Engine. In Yuanxu Yu, Zhengtao Yu, and Jingying Zhao, editors, *Computer Science for Environmental Engineering and EcoInformatics*, volume 159, pages 477–481. Springer Berlin Heidelberg, Berlin, Heidelberg, 2011. ISBN 978-3-642-22690-8 978-3-642-22691-5. doi: 10.1007/978-3-642-22691-5_84. URL http://link.springer.com/10.1007/978-3-642-22691-5_84.

[68] B.T.C. Zandbergen. Thermal rocket propulsion(2.07). Technical report, Delft University of Technology, 2018.

[69] Davide Zuzio, Jean-Luc Estivalèzes, and Bastien DiPierro. An improved multiscale Eulerian–Lagrangian method for simulation of atomization process. *Computers & Fluids*, 176:285–301, November 2018. ISSN 0045-7930. doi: 10.1016/j.compfluid.2016.12.018. URL http://www.sciencedirect.com/science/article/pii/S0045793016304017.

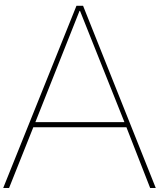

# 7th International Workshop on Turbulent Combustion of Sprays (TCS7) - Abstract

The abstract of the poster presented during the ”7th International Workshop on Turbulent Combustion of Sprays” in Tenerife, Spain can be found below.

# Hybrid Volume of Fluid/Discrete Particle Simulation of the Sydney Needle Burner Spray

B.I.Pal, D.J.E.M.Roekaerts[1,2,*], B.T.C.Zandbergen[3]
[1]Department of Process and Energy, Delft University of Technology, Delft, Netherlands
[2]Power and Flow, Department of Mechanical Engineering, Eindhoven University of Technology, Eindhoven, Netherlands
[3]Department of Aerospace Engineering, Delft University of Technology, Delft, Netherlands
*Corresponding author: D.J.E.M.Roekaerts@tudelft.nl

**Abstract**

The topic of this work is the validation of a hybrid multi-phase solver for atomization simulations. Early 2018 saw the release of the "VOF-to-DPM" solver in Ansys Fluent 19. This solver attempts to tackle the demanding computational cost of simulating primary atomization via the combination of two commonly used methods: Volume of Fluid (VOF) & Discrete Phase Model (DPM). The solver uses geometric criteria to switch between an Eulerian formulation (both phases) and an Eulerian-Lagrangian one. There are two asphericity criteria that are continuously calculated for each identified liquid ligament. When the criteria are met, the liquid mass is converted to a discrete particle surrounded by the gaseous phase. The cells that contained the ligament are filled with the gaseous phase. A dynamic mesh is used to enable refinement near the gas liquid interface in an effort to better predict ligament shapes at an affordable computational cost. To study the capability of the solver to predict spray properties, an air-blast atomization case was simulated. Validation was carried out using the NAS-8-25 dataset from the University of Sydney needle burner database [1]. The burner consists of a circular needle injecting acetone into a gaseous coflow. The simulation assumes iso-thermal, non-reacting, non-evaporating flow. A hybrid RANS-LES turbulence model is used. The k-$\omega$ SST model is used near the walls and LES with the WALE sub-grid scale model is used in the core flow [2]. A representative view of the transition between models can be seen in Fig. 1. The needle wall is red, the VOF phase is green and the colored dots are discrete particles (not to scale).

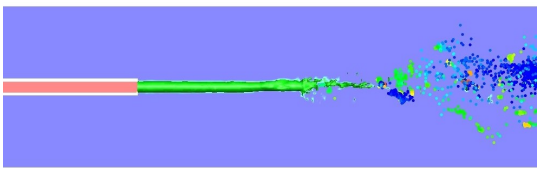

**Figure 1.** Continuum to discrete phase transition [3]

Preliminary results indicate that the solver is capable of producing a droplet distribution that is physically meaningful. Qualitative agreement of spray SMD values has been achieved with experiment. Quantitative agreement is yet to be achieved. Initial findings indicate SMD values off by a factor 2-2.5 versus experiment. This is attributed to low mesh resolution. Droplet velocity trends do not fully agree with experiment. It is believed that improperly resolved turbulent structures and/or the multi-phase transition parameters may be the cause. The primary identified drawback is a susceptibility to numerical instabilities likely due to the multi-phase transition mechanism. It was found that due to the geometric criteria for transition, results are highly sensitive to cell aspect ratios.

It is concluded that the solver has the potential to output spray properties at reasonable computational cost. A single, 16 core machine was used for all simulations. The unrefined grid contained 450k cells. The capability of producing accurate results requires further studies to confirm. Future work aims to investigate sensitivity to mesh resolution and transition criteria tolerances. It is expected that tighter tolerances on asphericity criteria will increase SMD accuracy by mitigating premature transition to the discrete phase. In addition, studies of which physical models (dispersion, secondary breakup) and what parameters produce the best results in combination with the VOF-to-DPM solver are also of interest.

## References

[1] Clean Combustion Research Group, Spray Jets and Flames Database, University of Sydney, http://web.aeromech.usyd.edu.au/thermofluids/database.php
[2] Ansys Fluent Theory Guide 19.2, Technical report, Ansys Inc., 2019
[3] Pal, B.I., Numerical Investigation of Spray Formation in Air-Blast Atomizers, MSc. Thesis, Delft University of Technology, 2019

# B

# Simulation Data Guide

This document serves as a user guide to the data provided at the conclusion of this study. The provided data should allow the reproduction of all SMD, droplet velocity, gas phase velocity and mass flow rate plots found in this work.

The data set consists of a zip file organized in 5 main folders. Four contain simulation data for each simulation in Table 6.1. The fifth contains two mesh files. The mesh files use the .msh extension. The first mesh (Sim14) is the mesh used for all the simulations discussed in this work. The second mesh, named Sim5, is a finer mesh of the same geometry that was not used due to time constraints.

Each simulation folder contains two subfolders: "Ansys Fluent Files" and "Extracted Data". The former will contain one set of .cas and .dat files which can be read into Fluent directly. These files contain all the settings used to run the case and the data from the last time-step used during this study. The Extracted Data subfolder will contain droplet data in the form of .csv files for each simulation, entitled "Sim1-4droplets". All csv files follow the format seen in Fig. B.1:

| x | y | z | u | v | w | diameter | Temp | parcel-mass | mass | n-in-parcel | time | flow-time | r/D |
|---|---|---|---|---|---|---|---|---|---|---|---|---|---|
| 3.00E-03 | 6.48E-04 | -9.52E-04 | 4.69E+01 | -5.33E-01 | -2.26E-01 | 5.21E-06 | 3.00E+02 | 1.03E-13 | 5.84E-14 | 1.77E+00 | 5.39E-04 | 3.27E-02 | 1.15E-01 |
| 3.00E-03 | 7.84E-04 | -7.07E-04 | 4.05E+01 | -1.19E+00 | -1.38E+00 | 2.03E-05 | 3.00E+02 | 1.37E-11 | 3.44E-12 | 3.99E+00 | 6.57E-04 | 3.27E-02 | 1.06E-01 |
| 3.00E-03 | -9.78E-04 | 1.69E-03 | 4.93E+01 | -2.81E-01 | 8.08E-01 | 1.35E-05 | 3.00E+02 | 7.23E-12 | 1.02E-12 | 7.08E+00 | 5.86E-04 | 3.27E-02 | 1.95E-01 |
| 3.00E-03 | -2.28E-03 | 9.77E-04 | 4.24E+01 | -8.99E-01 | 8.95E-02 | 2.09E-05 | 3.00E+02 | 6.47E-12 | 3.77E-12 | 1.72E+00 | 8.64E-04 | 3.27E-02 | 2.48E-01 |
| 3.00E-03 | 1.79E-03 | -2.58E-03 | 2.54E+01 | 1.36E+00 | -1.95E+00 | 8.23E-05 | 3.00E+02 | 4.40E-11 | 2.29E-10 | 1.92E-01 | 3.27E-02 | 3.27E-02 | 3.14E-01 |
| 3.00E-03 | -3.37E-03 | 1.40E-03 | 2.87E+01 | -1.61E+00 | 5.82E-01 | 6.09E-05 | 3.00E+02 | 1.29E-11 | 9.29E-11 | 1.39E-01 | 3.27E-02 | 3.27E-02 | 3.65E-01 |
| 3.00E-03 | -3.70E-03 | -1.18E-03 | 2.28E+01 | 3.25E+00 | 1.25E-01 | 7.12E-05 | 3.00E+02 | 2.06E-11 | 1.49E-10 | 1.39E-01 | 3.27E-02 | 3.27E-02 | 3.88E-01 |
| 3.00E-03 | -6.97E-04 | 9.04E-04 | 4.03E+01 | -1.51E+00 | -3.42E-01 | 1.58E-05 | 3.00E+02 | 4.85E-12 | 1.63E-12 | 2.97E+00 | 8.36E-04 | 3.27E-02 | 1.14E-01 |
| 3.00E-03 | 6.08E-04 | 3.05E-04 | 5.08E+01 | -2.81E+00 | -1.72E+00 | 5.57E-06 | 3.00E+02 | 1.54E-12 | 7.10E-14 | 2.17E+01 | 7.37E-04 | 3.27E-02 | 6.80E-02 |
| 3.00E-03 | -1.13E-03 | -3.52E-03 | 2.91E+01 | -2.31E+00 | -3.85E+00 | 1.35E-04 | 3.00E+02 | 1.86E-10 | 1.01E-09 | 1.84E-01 | 3.27E-02 | 3.27E-02 | 3.70E-01 |
| 3.00E-03 | -2.21E-03 | 9.20E-04 | 4.51E+01 | -2.46E+00 | 7.21E-01 | 1.70E-05 | 3.00E+02 | 2.37E-11 | 2.03E-12 | 1.17E+01 | 6.15E-04 | 3.27E-02 | 2.39E-01 |
| 3.00E-03 | -6.86E-05 | 5.10E-03 | 2.41E+01 | 2.23E-01 | 3.26E+00 | 7.12E-05 | 3.00E+02 | 2.08E-11 | 1.48E-10 | 1.40E-01 | 3.27E-02 | 3.27E-02 | 5.10E-01 |
| 3.00E-03 | 6.13E-04 | 3.03E-04 | 5.10E+01 | -2.93E+00 | -1.68E+00 | 5.57E-06 | 3.00E+02 | 1.63E-12 | 7.12E-14 | 2.29E+01 | 7.38E-04 | 3.27E-02 | 6.84E-02 |
| 3.00E-03 | -7.39E-04 | 6.19E-04 | 4.07E+01 | -2.41E+00 | -1.09E+00 | 1.65E-05 | 3.00E+02 | 5.25E-12 | 1.85E-12 | 2.83E+00 | 8.42E-04 | 3.27E-02 | 9.64E-02 |
| 3.00E-03 | 8.07E-04 | -1.98E-04 | 4.42E+01 | 1.51E+00 | -5.01E+00 | 2.74E-06 | 3.00E+02 | 6.83E-14 | 8.42E-15 | 8.11E+00 | 5.85E-04 | 3.27E-02 | 8.31E-02 |
| 3.00E-03 | -4.10E-03 | 9.22E-04 | 2.01E+01 | 3.08E+00 | -2.12E-01 | 1.25E-04 | 3.00E+02 | 4.82E-10 | 8.05E-10 | 5.99E-01 | 3.27E-02 | 3.27E-02 | 4.20E-01 |
| 3.00E-03 | 3.14E-03 | -2.11E-03 | 2.52E+01 | -3.24E+00 | 1.42E+00 | 6.12E-05 | 3.00E+02 | 5.39E-11 | 9.45E-11 | 5.71E-01 | 3.27E-02 | 3.27E-02 | 3.78E-01 |

.

Figure B.1: Data format for all droplet files

Columns x,y and z represent droplet positions and u,v,w represent velocity components. The r/D column marks the radial location at which the parcel was recorded. The last column of relevance is the flow-time column, which indicates what time the parcel was sampled. All parameters are given in SI units. For details on the other columns, the reader is referred to the Ansys Fluent Theory guide [1].

Simulations 1 and 4 contain additional data in the Extracted Data folders. In the case of Simulation 1, the convergence data for the velocity field seen in section 8.1 can be found. There are two data series, one for the exit plane and one for the location upstream of the

exit plane. These are labeled ”exit plane” and ”upstream” respectively. The data sets in each series are numbered in the order they were recorded, the lowest number is arbitrary and only the order is of importance. Each set contains data for 2000 time steps using an average timestep of 5e-08 seconds. An included readme file indicates which specific data sets were used in section 8.1.

The Extracted Data folder of Simulation 4 contains the mass flow rate data seen in Chapter 7. These flow rates were recorded at the exit plane of the domain. There are two csv files: one for the continuum phase and one for the discrete phase. In both cases, the column on the left is the mass flow rate (kg/s) and the column on the right is the simulation time (sec). Again, the first value of the simulation time is arbitrary. The relevance of the time column is that it indicates the time span of the sample.